DIFFUSE RADIO EMISSION IN MERGING GALAXY CLUSTERS

DISSERTATION

ZUR ERLANGUNG DES DOKTORGRADES AN DER FAKULTÄT FÜR MATHEMATIK, INFORMATIK UND NATURWISSENSCHAFTEN FACHBEREICH PHYSIK DER UNIVERSITÄT HAMBURG

VORGELEGT VON

ALEXANDER RICHARD JONES

HAMBURG, 2023

Gutachter/innen der Dissertation:	Prof. Dr. Francesco de Gasperin Prof. Dr. Marcus Brüggen
Zusammensetzung der Prüfungskommission:	Prof. Dr. Jochen Liske Prof. Dr. Francesco de Gasperin Prof. Dr. Marcus Brüggen Prof. Dr. Thomas Kupfer Prof. Dr. Stephan Rosswog
Vorsitzende/r der Prüfungskommission:	Prof. Dr. Jochen Liske
Datum der Disputation:	15.01.2024
Vorsitzender des Fach-Promotionsausschusses PHYSIK:	Prof. Dr. Markus Drescher
Leiter des Fachbereichs PHYSIK:	Prof. Dr. Wolfgang J. Parak
Dekan der Fakultät MIN:	Prof. Dr.-Ing. Norbert Ritter

Zusammenfassung

Galaxienhaufen befinden sich an den Knotenpunkten der großskaligen Filamente des kosmischen Netzes und sind Ansammlungen von Hunderten bis Tausenden von Galaxien, die von Halos aus dunkler Materie umgeben sind. Den baryonischen Massengehalt von Galaxienhaufen dominiert jedoch das heiße, magnetisierte Intracluster-Medium (ICM), das das Haufenvolumen ausfüllt. Wenn Galaxienhaufen kollidieren und miteinander verschmelzen, werden enorme Energiemengen in das ICM eingespeist, was eine Vielzahl physikalischer Prozesse antreibt. Ein Teil der verlorenen Gravitationsenergie fließt in die Beschleunigung der kosmischen Strahlung auf relativistische Geschwindigkeiten durch magnetohydrodynamische Turbulenzen auf Galaxienhaufen-Skalen und die Ausbreitung von Stoßwellen. Die so beschleunigte kosmische Strahlung erzeugt in Gegenwart von μG-Magnetfeldern Synchrotronstrahlung, die als diffuse Radioemission beobachtet wird. Die durch Verschmelzungen verursachte großskalige diffuse Radioemission wird grob in zwei Kategorien unterteilt: Radiohalos, die durch Turbulenzen erzeugt werden, und Radiorelikte, die auf Schockwellen der Verschmelzung zurückgehen.

In dieser Dissertation konzentriere ich mich hauptsächlich auf die Eigenschaften von Radiorelikten. Radiorelikte befinden sich in der Peripherie einiger verschmelzender Cluster und sind bogenförmige Radiostrukturen mit einer Länge in der Größenordnung von 1 Mpc. Der Beschleunigungsmechanismus, welcher Radiorelikte erzeugt, die diffusive Stoßbeschleunigung (DSA), ist weithin akzeptiert. Allerdings ist die Entstehung von Radiorelikten noch nicht vollständig geklärt und es bleiben offene Fragen bestehen. Kann die DSA von Elektronen aus dem thermischen Plasma die Eigenschaften von Radiorelikten vollständig erklären, oder ist eine erneute Beschleunigung einer Population leicht relativistischer Elektronen der kosmischen Strahlung erforderlich? Wenn eine Wiederbeschleunigung erforderlich ist, woher kommt dann eine solche Population? Ist DSA der einzige Beschleunigungsmechanismus, der an der Reliktgenerierung beteiligt ist?

Mithilfe von Multiwellenlängenbeobachtungen untersuchte ich die diametral entgegengesetzten Radiorelikte im verschmelzenden Cluster PSZ2 G096.88+24.18. Unter anderem fand ich heraus, dass eines der Relikte Hinweise auf eine Wiederbeschleunigung fossiler Elektronen, die durch vorherige AGN-Aktivität erzeugt wurden, sowie Turbulenzen im stromabwärts gelegenen Bereich des Relikts aufwies. Anhand der 35 Relikte, die in den Bildern des Data Releases 2 des LOFAR Two-meter Sky Survey (LoTSS)-Daten enthalten sind, untersuchte ich die statistischen Eigenschaften und Skalierungsbeziehungen von Relikten bei niedrigen Radiofrequenzen. Ich fand heraus, dass die Schockoberfläche zunimmt, wenn sie sich nach außen bewegt, und fand einen ersten Hinweis auf eine

Zunahme der Radioreliktleistung bei höheren Haufenmassen. Meine Ergebnisse deuten auch darauf hin, dass das Vorkommen von Radiorelikten höher ist als bisher berichtet und dass die Breite der Radiorelikte systematisch größer ist als die Erwartungen für eine Beschleunigung an einer Stoßfront ohne andere Beschleunigungsquelle.

Summary

Galaxy clusters, located at the nodes of the large-scale filaments of the cosmic web, are collections of hundreds to thousands of galaxies, surrounded by dark matter halos. Dominating the baryonic mass content of clusters, however, is the hot, magnetised intracluster medium (ICM) which fills the cluster volume. When clusters collide and merge together, enormous amounts of energy are injected into the ICM, driving a multitude of physical processes. A fraction of the energy dissipated goes into the acceleration of cosmic rays to relativistic speeds via cluster-scale magnetohydrodynamical turbulence and shock wave propagation. In the presence of μG magnetic fields, the cosmic rays accelerated in this way produce synchrotron radiation, observed as diffuse radio emission. Cluster-scale, merger-induced, diffuse radio emission is broadly split into two categories: giant radio halos, generated by turbulence, and radio relics, which trace merger shockwaves.

In this thesis I focus primarily on the properties of radio relics. Located in the peripheries of some merging clusters, radio relics are arc-like radio structures of the order of 1 Mpc in length. The acceleration mechanism which produces radio relics, diffusive shock acceleration (DSA), is well-established. However, the generation of radio relics is still not fully understood, and there remain open questions. Namely, can DSA of electrons from the thermal pool fully explain the properties of radio relics, or is re-acceleration of a population of mildly relativistic cosmic ray electrons required? If re-acceleration is required, where does such a population come from? Is DSA the only acceleration mechanism involved in relic generation?

Using multi-wavelength observations, I investigated the diametrically-opposed radio relics in the merging cluster PSZ2 G096.88+24.18. Amongst other results, I found that one of the relics showed evidence of re-acceleration of fossil electrons produced by previous AGN activity, as well as turbulence in the downstream region of the relic. Additionally, using the 35 relics contained in the LOFAR Two-metre Sky Survey (LoTSS) data release 2 images of galaxy clusters with *Planck*-derived masses, I investigated the statistical properties and scaling relations of relics at low radio frequencies. I found that the shock surface increases as it travels outwards, and tentative evidence for an increase in radio relic power at higher cluster masses. My results also suggested that the occurrence of radio relics is higher than previously reported, and that the width of radio relics is systematically higher than expectations for acceleration at a shock front with no other source of acceleration.

Eidesstattliche Versicherung

Hiermit versichere ich an Eides statt, die vorliegende Dissertationsschrift selbst verfasst und keine anderen als die angegebenen Hilfsmittel und Quellen benutzt zu haben.

Die eingereichte schriftliche Fassung entspricht der auf dem elektronischen Speichermedium.

Die Dissertation wurde in der vorgelegten oder einer ähnlichen Form nicht schon einmal in einem früheren Promotionsverfahren angenommen oder als ungenügend beurteilt.

Alexander Richard Jones
Hamburg, den 27.10.2024

Contents

Chapter 1

Introduction

1.1 Galaxy clusters

Matter in the Universe is clumped together in a web-like structure, comprised of filaments of dark matter (DM), galaxies and gas, separated by vast voids containing almost no matter. At the nodes of these filaments lie galaxy clusters; large overdensities of hundreds to thousands of galaxies, spanning a virial radius of $\sim 1-3$ Mpc, surrounded by large DM halos, which dominate the cluster mass content ($\sim 80\%$). With typical masses $\sim 10^{14}$ - $10^{15} M_{\odot}$, galaxy clusters are the most massive virialised systems in the Universe. Galaxy clusters have formed and grown from initial density perturbations in the Universe to their current mass almost exclusively through gravitational interactions (Press & Schechter, 1974). The mass function of clusters is therefore dependent only on the initial density perturbations and can be used to constrain cosmological parameters, such as the cosmic matter density fluctuations, σ_8, and the total mass density, Ω_m (e.g. Reiprich & Böhringer, 2002).

One consequence of the large masses of galaxy clusters is that their enormous potential wells act as gravitational lenses for light from background galaxies. The images we observe can be magnified, distorted and, in some cases, duplicated. The magnification of a source is quantified by the convergence, $\vec{\kappa}$, which depends only on the projected surface mass distribution, $\Sigma(\vec{\theta})$, and the geometry of the lensing system. I.e. for a source at angular diameter distance D_s to the observer, and D_{ls} to a gravitational lens, the convergence is given by

$$\vec{\kappa} = \Sigma(\vec{\theta}) \frac{4\pi G D_l D_{ls}}{c^2 D_s}, \tag{1.1}$$

where D_l is the angular diameter distance to the lens. Since it is impossible to know the intrinsic ellipticity of a lensed galaxy, a useful observable to measure is the *average* ellipticity, $\langle \epsilon \rangle$, of a sample of galaxies which have all been gravitationally lensed by the same foreground source. The galaxies should be randomly oriented in space, meaning that the intrinsic ellipticities are averaged out, leaving only the effect of the lens. In the weak-lensing regime, i.e. $\kappa \ll 1$, outside of the high surface mass density regions near the cluster centre, the average ellipticity is related to the image magnification, and the

Figure 1.1: *Chandra* X-ray image of the Perseus cluster of galaxies. Credit: NASA/CXC/SAO/E. Bulbul, et al.

anisotropic distortion of the image, i.e. the shear, γ, by

$$\langle \epsilon \rangle \approx \frac{\gamma}{1-\kappa}. \tag{1.2}$$

In this way, weak lensing measurements can provide a probe of the total mass of a cluster and its distribution (e.g. Wright & Brainerd, 2000). For a review of gravitational lensing, as applied to galaxy clusters, see Umetsu (2020), and Bartelmann & Schneider (2001) for weak lensing in particular.

At the cores of most, if not all, galaxies lie supermassive black holes (SMBHs). A fraction of these SMBHs, called active galactic nuclei (AGNs), are extremely luminous (up to 10^{47}erg s^{-1}) in both continuum and line emission across $\sim$ 20 decades of the electromagnetic spectrum. AGNs are the brightest sources within their host galaxies and often outshine the rest of the emitting galactic sources by a few orders of magnitude. As

matter accretes onto these SMBHs, it forms an accretion disc, converting gravitational potential energy into thermal energy, heating the accreted matter to $\sim 10^6$ K and emitting predominantly optical and UV emission. This emission is scattered by a hot corona of electrons surrounding the SMBH, to X-ray wavelengths, via Compton scattering (Haardt & Maraschi, 1991). A small fraction of AGNs are also bright in the radio regime, and therefore named radio-loud AGNs. Collimated outflows from the central source launch relativistic cosmic-ray electrons (CRes) into the surrounding medium in jets. Since the jets are lighter than their surrounding medium, the material is directed sideways and backwards away from the source, to form lobes. The generated radio-bright jets and lobes are typically pc - Mpc in size and have $\sim$ nT strength magnetic fields, and those residing in clusters often have different morphologies to their counterparts in non-rich environments. This is most strikingly seen in bent-tail sources, preferentially found in clusters, where the movement of the galaxy through its surrounding medium bends the jets away from the direction of motion (for a review, see Hardcastle & Croston, 2020).

1.1.1 The intracluster medium

Dominating the baryonic mass content of clusters is the intracluster medium (ICM), which permeates the regions between cluster-member galaxies. The ICM is a hot ($\sim 10^8$ K), low-density ($n_e \sim 10^{-3}\mathrm{cm}^{-3}$), magnetised ($\sim \mu$G) plasma, which accounts for $\sim 15-20\%$ of the total mass of a galaxy cluster. Electromagnetic interactions between the free electrons and ions in the hot plasma decelerate the electrons, resulting in the emission of X-ray photons (i.e. thermal bremsstrahlung emission). The ICM is therefore extremely luminous in X-rays ($\sim 10^{43-45}\mathrm{erg\ s}^{-1}$). Fig. 1.1 shows an image of the Perseus cluster, made from *Chandra* X-ray data.

The X-ray luminosity of a cluster is a relatively straightforward observable to measure and, under a few assumptions, can be used to determine intrinsic cluster properties. It is therefore an appealing property to measure in the context of understanding cluster populations and their application to cosmology. To this end, many X-ray surveys have been undertaken, such as the Northern *ROSAT* all-sky (NORAS) galaxy cluster survey (Böhringer et al., 2000) and the *ROSAT*-ESO flux-limited X-ray (REFLEX) galaxy cluster survey (Böhringer et al., 2001), which detected 495 and 452 galaxy cluster sources, respectively. Assuming that a cluster is in virial equilibrium, its X-ray temperature, T, scales with the cluster mass, M, as

$$T \propto M^{2/3}. \tag{1.3}$$

The X-ray luminosity, L_X, of a cluster, with gas density ρ_{gas} and a gas mass fraction f_{gas}, is given by

$$L_X(T) = f_{gas}^2 [M(T)\Lambda(T)] \langle \rho_{gas}^2 \rangle / \langle \rho_{gas} \rangle^2, \tag{1.4}$$

where the angle brackets denote a volume average and $\Lambda(T)$ is the cooling function (Arnaud & Evrard, 1999). For Bremsstrahlung emission, $\Lambda(T) \propto T^{1/2}$. Therefore, combining with Eq. 1.3, assuming constant f_{gas} and cluster gas structure, $\langle \rho_{gas}^2 \rangle / \langle \rho_{gas} \rangle^2$, we see that

$$L_X \propto T^2, \tag{1.5}$$

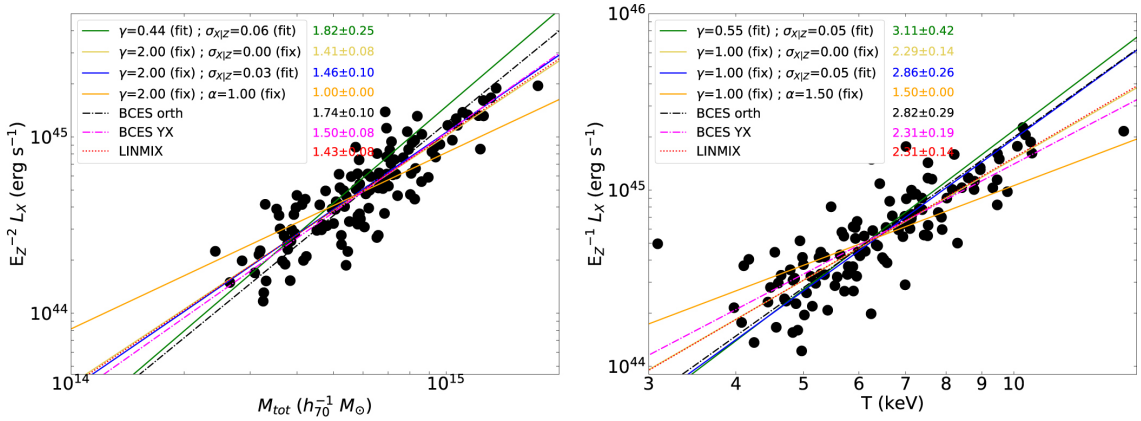

Figure 1.2: Cluster scaling relations from Lovisari et al. (2020) for a representative sample of clusters observed by both *Planck* and *XMM-Newton*. **Left:** X-ray luminosity vs. cluster mass. **Right:** X-ray luminosity vs. temperature.

and

$$L_X \propto M^{4/3}. \tag{1.6}$$

In practice, the actual scaling relations measured in cluster samples are steeper (e.g. Pratt et al., 2009). Fig. 1.2 shows the correlation of cluster X-ray luminosity, as measured by *XMM-Newton*, with both cluster mass and temperature measured by Lovisari et al. (2020). It can often be useful to use Y_X - i.e. the product of the total gas mass, M_{gas}, measured from gas density profiles (e.g. Croston et al., 2008) within R_{500}[1], and its temperature - as a mass proxy, since it scales tightly with the total mass (e.g. Arnaud et al., 2007).

X-ray observations of the ICM can also provide a wealth of information on the dynamical history of a cluster. The X-ray emission of relaxed clusters, i.e. those in or close to thermal equilibrium, typically has a strong peak at the cluster centre, roughly coincident with the brightest cluster galaxy (BCG). The metal-rich gas producing this emission is significantly cooler than its immediate surroundings, and they are therefore named cool core (CC) clusters. The relatively short radiative lifetime of CCs implies the existence of cooling flows at the centres of relaxed clusters (Fabian et al., 1984). The temperature drop in CCs is, however, not large enough to support this scenario, leading to the suggestion that there must be a source of heating which balances such a cooling flow. One likely source of heating is from AGN radio emission associated with the BCG (Binney & Tabor, 1995). Low surface brightness radio emission outside the extent of radio emission associated with ongoing AGN activity is observed around many cluster-member galaxies. The bubbles of CRs that produce them are buoyant and rise slowly (about half the sound speed) through the cooler surrounding gas, heating it (Churazov et al., 2001; Bîrzan et al., 2004). Heating the ICM can destroy cooling flows at cluster centres by increasing the entropy and radiative lifetime of the gas. Once the AGN stops powering the bubbles, the cooling flow may then restart and eventually restart AGN activity, producing a feedback loop which balances the cooling and AGN heating (Brüggen & Kaiser, 2002). Clusters without a sharp temperature decrement at their cores are referred to as non-cool core (NCC) clusters and are typically

[1] R_{500} is defined as the radius at which the mean density of the cluster is 500 times the critical density of the Universe at the cluster redshift

associated with dynamical disturbance.

Measurements of the surface brightness, gas density and temperature profiles have revealed the presence of X-ray substructures in the ICM generated by gas motions in the cluster. A prominent example of this are cold fronts, observed as sharp surface brightness, gas density and temperature discontinuities between the relatively cold, dense gas inside the cold front and the hotter, less dense ICM beyond (Markevitch & Vikhlinin, 2007, for a review). Thought to primarily be the result of sloshing gas motions or the remnants of minor merger events, cold fronts have been observed in many clusters to date, both relaxed and disturbed, e.g. Abell 2142 (Markevitch et al., 2000) and Abell 3667 (Vikhlinin et al., 2001). In a merger, the gas peak can be displaced from the DM peak by ram pressure. Once it falls back towards the centre of the cluster potential well, the dense gas interacts with the less dense gas moving in the opposite direction and forms a cold front. The gas will overshoot the cluster core, producing a concentric cold front on the opposite side of the cluster when the same process happens on the other side (Ascasibar & Markevitch, 2006). Depending on the merger mass ratio, impact parameter etc. of the merger, the dynamical state of the cluster may or may not be significantly affected. X-ray observations can also be used to study the wealth of effects on cluster dynamics caused by major merger events between clusters. This will be detailed in Sec. 1.2.

A further consequence of the high temperatures and ionisation of the ICM is that photons passing through will be deflected by inverse-Compton (IC) scattering off the electrons contained within. Consequently, the spectrum of the cosmic microwave background (CMB) is altered by the interaction of the photons with the ICM, i.e. the Sunyaev-Zel'dovich (SZ) effect (Sunyaev & Zel'dovich, 1970, 1972, 1980). The brightness of the CMB spectrum is changed by a cluster of temperature T_e, with number electron density n_e, along the line-of-sight l, by

$$\Delta I_\nu = j_\nu y \equiv j_\nu \int n_e \frac{k_B T_e}{m_e c^2} \sigma_T dl, \tag{1.7}$$

where j_ν encodes the frequency dependence, and y is the Compton parameter, which is redshift-independent (Birkinshaw, 1999; Carlstrom et al., 2002). The SZ effect can therefore be used to detect distant clusters, as has been done by e.g. the *Planck* satellite in its all-sky *Planck* SZ (PSZ) catalogue (Planck Collaboration et al., 2014, 2016). The second, deepest catalogue, PSZ2, contains 1653 SZ sources, of which 1203 are confirmed galaxy clusters. Integrating y over the cluster volume, V, and multiplying by D_A^2, where D_A is the angular diameter distance, gives the intrinsic thermal SZ signal,

$$Y_{SZ} = \int n_e \frac{k_B T_e}{m_e c^2} \sigma_T dV. \tag{1.8}$$

The integrated effect of a cluster is therefore a function of only the amount of gas and its temperature. Consequently, Y_{SZ} is expected to correlate tightly with cluster mass (e.g. Barbosa et al., 1996; da Silva et al., 2004). Many studies have indeed found a correlation between Y_{SZ} and both the X-ray-derived cluster mass (e.g. Benson et al., 2004; Bonamente et al., 2008) and weak lensing-derived mass (e.g. Marrone et al., 2009; Planck Collaboration et al., 2011). Fig. 1.3 shows the correlation between Y_{SZ} and cluster mass, derived from the $M_{500} - Y_X$ correlation, for a representative sample of 33 clusters in the REFLEX sample by Arnaud et al. (2010).

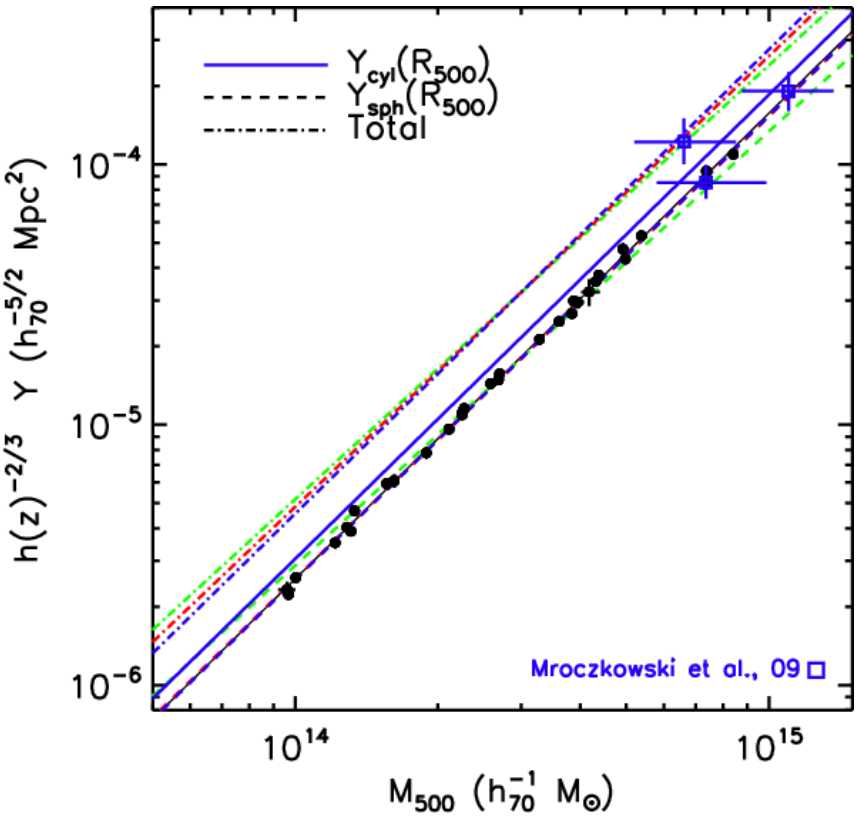

Figure 1.3: Correlation of the integrated Compton parameter and cluster mass from Arnaud et al. (2010).

1.1.2 Magnetic fields in the ICM

Magnetic fields, present at all scales throughout the Universe, permeate galaxy clusters. Though the origin of cluster-scale magnetic fields is uncertain, it is most likely that small seed magnetic fields were present in the early Universe and were subsequently amplified to their currently observed $\sim \mu$G values by a combination of adiabatic compression and small-scale dynamo amplification (e.g. Beck et al., 1996; Donnert et al., 2018).

Though their presence is obvious from the existence of large-scale radio synchrotron emission, the measurement of the strength of magnetic fields in clusters is limited to indirect methods. One such method is to use the synchrotron emission itself, since the emissivity at a given frequency depends on the magnetic field strength and electron energy spectrum. If one assumes equipartition of energy distributed between magnetic fields and energetic particles, the luminosity of the synchrotron radiation, L, produced by CRes within the cluster can be used to estimate the equipartition magnetic field strength through

$$B = \left(\frac{L(1+k)}{\Phi V} \right)^{2/7}, \tag{1.9}$$

where Φ is the filling factor of the magnetic field and relativistic particles and k is a number which depends on the CR acceleration mechanism (Pacholczyk, 1970). Typically, $k = 1$ is assumed for turbulent and shock acceleration, as is commonly observed in clusters

(see Sec. 1.2). Brunetti et al. (1997) also suggested integrating over a range of electron energies, $\gamma_{min} - \gamma_{max}$, resulting in

$$B' \sim 1.1 \gamma_{min}^{\frac{1-2\alpha}{3+\alpha}} B^{\frac{7}{2(3+\alpha)}}, \tag{1.10}$$

where B is the magnetic field derived from Eq. 1.9 and α is the radio spectral index[2] (see also Beck & Krause, 2005). This has been done for a number of clusters, and typically puts magnetic field strengths on cluster scales at $0.1 - 10\mu$G. However, this approach requires a number of assumptions to be made, for example that the entire cluster volume is filled with magnetic fields and relativistic particles, i.e. $\Phi = 1$.

An alternative method is to measure the Faraday rotation of linearly-polarised sources which lie behind a galaxy cluster, along our line of sight, i.e. rotation measure (RM) synthesis. Since the right- and left-handed circularly polarised components of synchrotron emission propagate through the magnetised ICM at different phase velocities, the plane of polarisation is rotated. The angle through which the polarised emission is rotated, $\Delta\Psi$, at a given wavelength, λ, depends on the magnetic field component of the intervening ICM along the line of sight, $B_{\parallel}$, through

$$\Delta\Psi \propto \lambda^2 \int n_e B_{\parallel} dl, \tag{1.11}$$

where n_e, the electron density along the line of sight, can be inferred from X-ray observations (Burn, 1966; Brentjens & de Bruyn, 2005). One advantage of this method is that it does not require observation of a diffuse radio source within the cluster and can therefore be used to measure the magnetic field distribution. Bonafede et al. (2010) found, by measuring $\Delta\Psi$ of seven sources embedded within the Coma cluster, that the magnetic field strength fits a Kolmogorov power spectrum with central intensity $\sim 5\mu$G and decreases radially.

1.2 Galaxy cluster mergers

In the ΛCDM model of structure formation, the galaxy clusters we observe today have formed and grown through a combination of accretion of matter from filaments and extremely energetic ($10^{63} - 10^{64}$ erg) merger events with other clusters. Due to the long timescales of these events ($\sim$ 1Gyr), we are only able to observe a snapshot of the merger. Fortunately, owing to the large number of mergers discovered by galaxy cluster surveys, we are able to piece together a picture of the evolution of a merger, though the details are not entirely clear. At large distances, galaxy clusters interact almost exclusively through gravitational attraction. The thermal plasma in each subcluster is approximately spherical, in thermal equilibrium and is centred on the bottom of the DM halo potential well. The subclusters are accelerated toward each other at speeds of $\sim$ 1000kms^{-1} (Thompson & Nagamine, 2012). As the clusters collide, the cluster gas is slowed by ram pressure. Since the cluster-member galaxies behave like collisionless particles, they, along with the

[2]The radio flux, S_ν, scales with frequency, ν, as $S_\nu \propto \nu^\alpha$. See Sec. 1.3.1 for more detail.

collisionless DM halo, move ahead of the ICM (Clowe et al., 2006). The interaction of the ICM of the two subclusters can generate turbulence (Sec. 1.2.1), launch giant shocks (Sec. 1.2.2), which heat the ICM (e.g. Markevitch et al., 1999), and large-scale motions disturb it from its equilibrium state. This is most obvious in X-rays, where the ICM is observed to be elongated along the merger axis, the CC has been destroyed and the BCG is displaced from the X-ray brightness peak.

Fig. 1.4 shows an example of a merging cluster, MACS J1752.0+4440, at various wavelengths. The top images show radio data, taken by GMRT, overlaid on an Sloan Digital Sky Survey (SDSS) image (left) and an *XMM-Newton* image (right) from Bonafede et al. (2012). The radio data shows a radio halo, roughly coincident with the X-ray emission from the ICM (see Sec. 1.2.1) and a clear pair of diametrically-opposed radio relics in the cluster outskirts (see Sec. 1.2.2). None of these radio sources have an optical counterpart. The bottom image shows the mass distribution, constructed from weak lensing using *Hubble Space Telescope* and Subaru optical images by Finner et al. (2021). The cluster is comprised of two distinct mass peaks, corresponding to the two merging subclusters.

There have been many proposed measures of the dynamical state of a cluster from its X-ray properties, but we focus here on the three most-commonly used metrics. The concentration parameter, c, defined by Santos et al. (2008) as the ratio of the X-ray flux, S_X, measured within two concentric circles, typically with radii 100 and 500 kpc, centred on the cluster centre, is given by

$$c = \frac{S_X(r < 100\text{kpc})}{S_X(r < 500\text{kpc})}. \tag{1.12}$$

Relaxed, CC clusters are very luminous at their cores, and mergers often destroy the CCs. The X-ray brightness is therefore more homogeneous in disturbed, NCC clusters and c smaller.

Since in a merger the ICM is slowed, relative to the cluster centre, the displacement of the X-ray surface brightness peak from the cluster centre can be used as another probe of the dynamical state (Mohr et al., 1993; Poole et al., 2006). The centroid shift, w, is the standard deviation of the projected separation between the cluster centre, calculated in a series of apertures with radius R_{ap}, given by

$$w = \left[\frac{1}{N_{ap} - 1}\Sigma_i(\Delta_i - \overline{\Delta})^2\right]^{1/2} \frac{1}{R_{ap}}, \tag{1.13}$$

where N_{ap} is the number of apertures used from $0.05R_{ap} - R_{ap}$, Δ_i the centroid of the i^{th} aperture, and $\overline{\Delta}$ the average centroid. A larger value of w is an indication that the X-ray brightness peak is further from the cluster centre and the cluster is therefore more dynamically disturbed.

The power ratio is a multipole decomposition of the mass distribution and provides a measure of the surface brightness fluctuations of the ICM (Buote & Tsai, 1995). They are defined as

$$P_0 = S_X(r < R_{ap})\ln(R_{ap}), \tag{1.14}$$

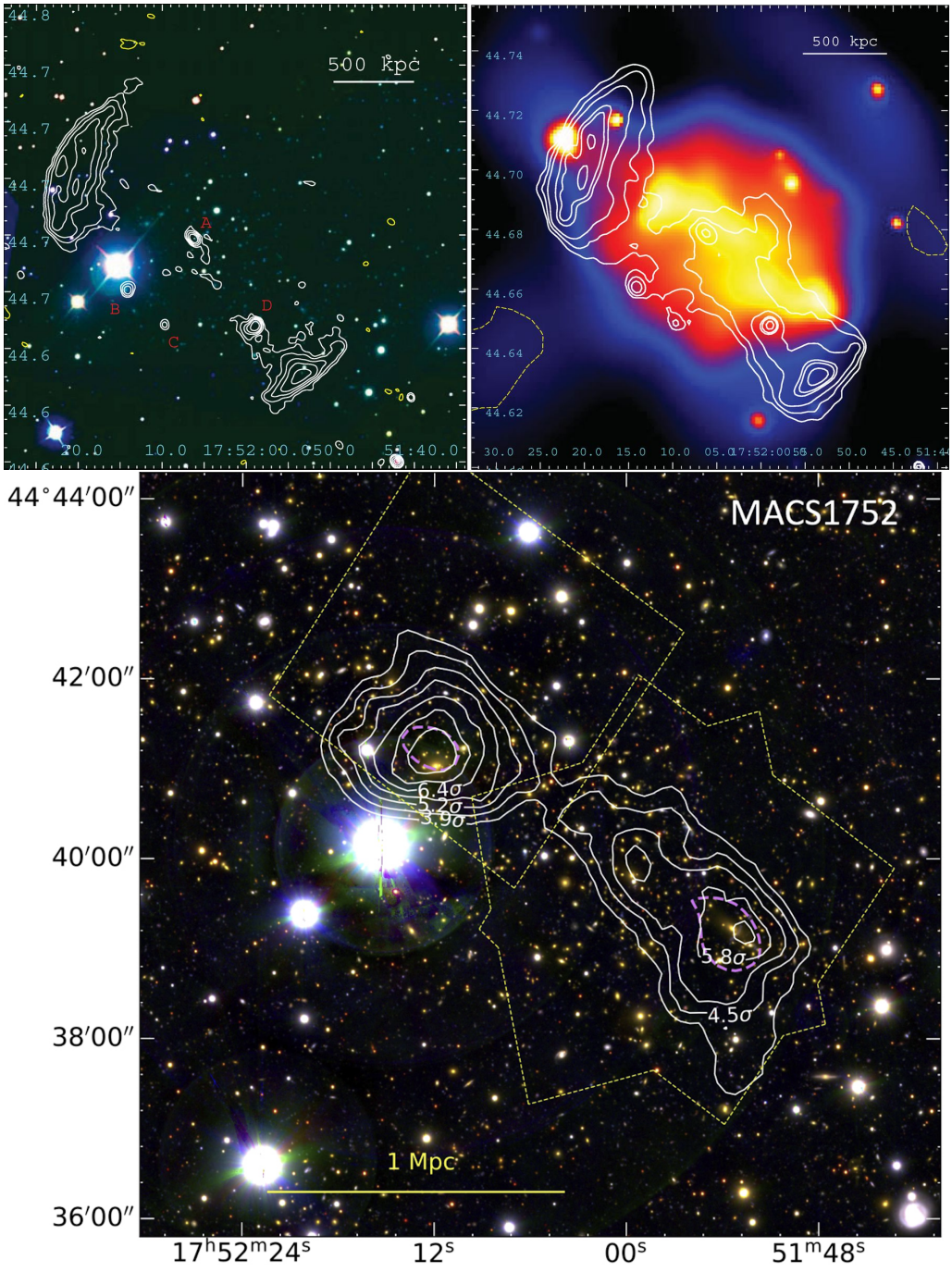

Figure 1.4: Merging cluster MACS J1752.0+4440. **Top left:** SDSS optical image from Bonafede et al. (2012). White contours show higher resolution 323 MHz radio brightness taken by GMRT. **Top right:** 0.2 - 12 KeV X-ray emission from *XMM-Newton*, also from Bonafede et al. (2012). White contours show the same radio data, but at low resolution. **Bottom:** Mass distribution reconstruction from *Hubble Space Telescope* and Subaru optical images by Finner et al. (2021). Optical image from Subaru data.

and

$$P_m = \frac{1}{2m^2 R_{ap}^{2m}}(a_m^2 + b_m^2), \tag{1.15}$$

where $a_m = \int_{r \leq R_{ap}} S_X(x)(r)^m \cos(m\phi) d^2x$ and $b_m = \int_{r \leq R_{ap}} S_X(x)(r)^m \sin(m\phi) d^2x$, integrated over all pixels, x. Typically, P_3/P_0 is chosen, as it is related to substructures (e.g. Bauer et al., 2005; Böhringer et al., 2010). Since disturbed clusters generally have larger surface brightness fluctuations, they are associated with larger power ratios.

The above measures of the dynamic state of a cluster are the most widely used, but there are many other metrics. For example, the offset between the X-ray peak and the BCG (Jones & Forman, 1984, 1999), the photon asymmetry in cluster X-ray images (Nurgaliev et al., 2013) and the ratio between soft and hard X-ray images (e.g. Allen & Fabian, 1997) have been proposed as alternatives. Each method has its own advantages and shortcomings, and can be biased in different ways, so a combination of parameters is most effective in separating clusters into relaxed and disturbed (Pinkney et al., 1996; Böhringer et al., 2010). Lovisari et al. (2017) found, using a sample of *Planck*-detected clusters, that the most robust parameters are the concentration parameter and the centroid shift. In my work I focus on the combination of these two parameters. Some attempts have also been made to combine different parameters into a single measure of dynamical status. For example, Rasia et al. (2013) defined the parameter M, and, more recently, Ghirardini et al. (2022) defined the relaxation score, $\mathcal{R}$, as ways to combine an arbitrary number of different indicators into a single parameter. Fig. 1.5 shows a selection of morphological estimators for a sample of X-ray clusters from Rasia et al. (2013). Clusters are more disturbed going from red, green, magenta to blue points.

1.2.1 Radio halos

A significant fraction ($\sim 10\%$) of the energy budget of a cluster merger event is dissipated in (re-)accelerating charged particles to relativistic energies. In the presence of cluster-scale magnetic fields, these relativistic charged particles produce diffuse radio synchrotron emission. One such example of radio emission observed in galaxy clusters is that of giant radio halos (RHs). Observed in $\sim 20-30\%$ of X-ray luminous clusters ($L_{0.1-2.4\mathrm{keV}} \geq 5 \times 10^{44}\mathrm{erg\ s^{-1}}$; Venturi et al., 2007, 2008; Kale et al., 2013, 2015), the low surface-brightness, unpolarised RHs roughly trace the thermal distribution of electrons in the ICM. I.e. RHs reside in the centre of clusters, typically overlapping with the thermal bremsstrahlung observed in X-rays, and fill a significant portion of the cluster volume ($\sim 1\mathrm{Mpc}^2$). The spectral index of RHs is steep ($-1.4 < \alpha < -1.1$), but roughly homogeneous. The homogeneity implies that there is no single point of CRe acceleration, but rather that they are (re-)accelerated throughout the RH.

The characteristic lifetime of highly-relativistic, synchrotron-emitting electrons in the ICM is too short for Mpc-scale diffuse radio emission to have been produced by a population of CRes accelerated in one location, which subsequently diffused across the cluster volume (for more details, see Sec. 1.3.1). In-situ acceleration is therefore required to explain the presence of RHs. One model proposed to explain the generation of RHs

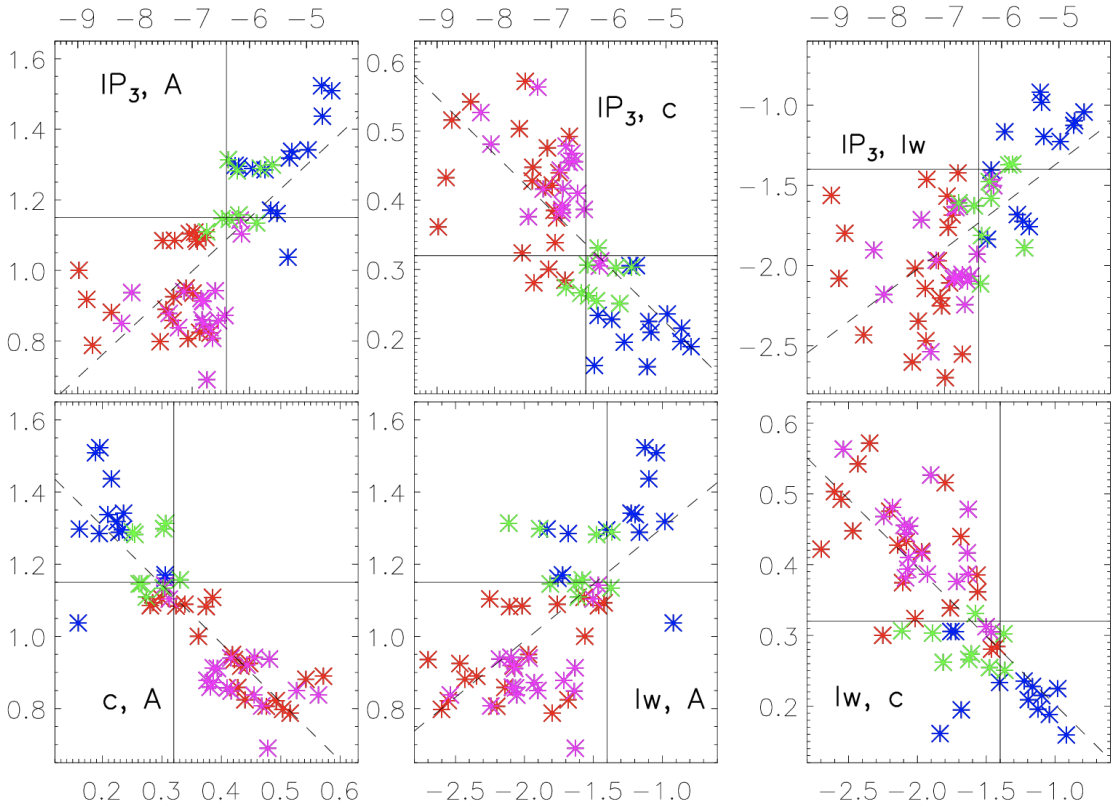

Figure 1.5: A combination of a selection of cluster morphological estimators from Rasia et al. (2013). The parameters are the decimal logarithm of the third order power ratio (lP_3), asymmetry parameter (A), X-ray surface brightness concentration (c), and decimal logarithm of the centroid shift (lw). Clusters are more disturbed going from red, green, magenta to blue points.

in clusters is the so-called secondary-model, in which the electrons required to produce RHs are produced by hadronic collisions between cosmic ray protons (CRp) and thermal protons. This model of RH-generation is generally disfavoured, since the collisions should also result in γ-ray emission and, to-date, no cluster has been observed with sufficient γ-ray emission to support this model (e.g. Ackermann et al., 2010). Alternatively, the steep spectra and high-frequency cutoff of RHs supports a scenario in which ICM electrons are accelerated in-situ by turbulent motions (second-order Fermi acceleration, or Fermi II) within the ICM, driven by mergers, as well as core sloshing (Brunetti et al., 2008). In this model, turbulence cascades from larger to smaller scales, until it reaches dissipative scales, at which it can accelerate electrons. The electrons scatter off magnetic inhomogeneities, gaining energy $E \propto \frac{v^2}{c^2}$ in head-on collisions, and losing energy otherwise. For the random motions of these electrons, there is a slightly greater probability of gaining energy through the scattering process, resulting overall in acceleration, though the process is inefficient (Fermi, 1949). For a review, specifically with regards to cluster merger turbulence, see Brunetti & Jones (2014). The magnetic field lines within the turbulent ICM are expected to be tangled and if there is a characteristic scale at which they are ordered, it is too small to observe polarised emission with the angular resolution of current state-of-the-art telescopes (e.g. Govoni et al., 2013).

The variety of different internal and external processes taking place in galaxy clusters makes them a diverse set of objects. It is therefore imperative to study representative samples to understand the effects that govern their properties. Through the combination of radio measurements of RHs and X-ray probes of cluster dynamical state, the relation between cluster mergers and RHs has become clear (e.g. Cassano et al., 2010). There is a bi-modal distribution in the dynamical properties of galaxy clusters, with RHs typically residing in dynamically-disturbed clusters. The scaling relations of radio halos have also been well-studied in the past decade. Numerous studies have shown that the power of radio halos correlates with cluster X-ray power, SZ-signal and cluster mass (e.g. Liang et al., 2000; Cassano et al., 2006; Cuciti et al., 2023), indicating that the infalling mass in a galaxy cluster merger is a direct driver of the radio power of a RH.

Above a steepening frequency, ν_s, which depends on the merger energetics, the integrated spectrum of RHs steepens. Only the most energetic mergers are able to generate sufficient turbulence to produce a RH spectrum with $\nu_s \gtrsim 1$ GHz (Cassano & Brunetti, 2005). This implies the existence of a population of low-power RHs with very steep spectra ($\alpha < -1.5$), so-called ultra-steep spectrum radio halos (USSRHs), resulting from low-mass mergers, which are unable to generate enough turbulence to produce GHz-emitting CRe. Therefore, the turbulent re-accleration model predicts that the fraction of RH-hosting clusters should increase with larger cluster mass, since the available energy budget in a merger is much greater. This is indeed observed in statistical samples of galaxy clusters. Cuciti et al. (2015) found that, at masses $> 8 \times 10^{14} M_{\odot}$, the occurrence of RHs is $\sim 60 - 80\%$, i.e. much greater than in lower mass clusters. Since minor mergers are more common than major mergers, the turbulent re-acceleration model also predicts that more RHs should be observed at lower observing frequencies, since high-frequency observations are only sensitive to the most energetic, major mergers. The advent of low-frequency observatories, such as LOFAR, has allowed the discovery of USSRHs (e.g. Brunetti et al., 2008; Cuciti et al., 2021), and it has been shown that RH occurrence increases with decreasing frequency (Cassano et al., 2023).

The somewhat regular morphology of RHs makes them relatively straightforward to model. Murgia et al. (2009) found that the flux profiles of RHs could be modelled as a projected exponential profile, with characteristic central intensity, I_0, and e-folding radius, r_e, i.e.

$$I(r) = I_0 e^{-r/r_e}. \tag{1.16}$$

By injecting mock RHs into in the uv datasets of clusters with no RH detection and measuring the brightness at which they are first detected, given the image noise, Bonafede et al. (2017) were able to place upper limits on the brightness a RH in these clusters would require to remain unobserved. Injection of mock halos to derive RH brightness upper limits have been used to show that clusters with/without observable RH constitute different populations in the correlation of RH power and cluster mass (Brunetti et al., 2007; Bruno et al., 2023; Cuciti et al., 2023).

1.2.2 Radio relics

Another, less common, group of radio objects associated with galaxy cluster mergers are radio relics (RRs). Found in $\sim$ 5% of galaxy clusters (Kale et al., 2015), RRs are roughly arc-shaped, ~Mpc-long diffuse radio structures which reside in the outskirts of some merging clusters. Their steep spectra ($\alpha \lesssim -1$) makes them challenging to observe at high radio frequencies and they have no optical counterpart. RRs are expected to trace shocks launched into the ICM by merger events.

1.2.2.1 Cluster shocks

Shocks have been observed directly in X-ray observations as sharp temperature, density, pressure and surface brightness discontinuities in the ICM. The strength, or Mach number, of a shock is the ratio of the shock speed and the sound speed, i.e. $\mathcal{M} = \frac{V_{sh}}{c_s}$. The Mach number of a shock can be estimated directly, using the Rankine-Hugoniot jump condition (Landau & Lifshitz, 1959), with X-ray measurements of the pre- and post-shock temperatures

$$\frac{T_{post}}{T_{pre}} = \frac{5\mathcal{M}^4 + 14\mathcal{M}^2 - 3}{16\mathcal{M}^2}, \tag{1.17}$$

or ICM densities

$$\frac{\rho_{post}}{\rho_{pre}} = \frac{4\mathcal{M}^2}{\mathcal{M}^2 + 3}. \tag{1.18}$$

ICM shocks measured this way typically have Mach numbers of $\mathcal{M} \lesssim 3$. Shocks have been detected in a number of clusters, for example Abell 2255 (Akamatsu et al., 2017), Abell 754 (Krivonos et al., 2003; Macario et al., 2011) and, most strikingly, 1E 0657-56 (Shimwell et al., 2015). Also called the "Bullet" cluster because of its morphology, 1E 0657-56 exhibits a bow shock on the western edge travelling outwards, caused by the passage of a subcluster through the core of the main cluster, with a cold front $\sim$ 100kpc behind. Fig. 1.6 shows an image of this cluster, as well as corresponding X-ray surface brightness and density profiles. The profiles show two clear discontinuities, corresponding to the cold front and shock front on the western side of the cluster.

Finoguenov et al. (2010) discovered, using deep *XMM-Newton* observations, that the RR in the nearby cluster Abell 3667 coincides with a shockwave in the cluster periphery, consistent with a merger shock with Mach number $\mathcal{M} \sim 2$. Subsequent studies have found further evidence of a direct connection between RRs and merger shocks, supporting the scenario that RRs are produced by shock acceleration. For example, Abell 521 (Brunetti et al., 2008; Giacintucci et al., 2008; Bourdin et al., 2013), Abell 2744 (Eckert et al., 2016; Hattori et al., 2017; Pearce et al., 2017) and Coma (Giovannini et al., 1991; Thierbach et al., 2002; Akamatsu & Kawahara, 2013; Ogrean & Brüggen, 2013) all host RRs with underlying shock detection. To-date, there are around 20 RRs with an associated shock detection, though there are > 50 known RRs (van Weeren et al., 2019). One likely cause of the discrepancy is that RRs are preferentially found in cluster outskirts, where the low X-ray photon count limits detections to nearby clusters, or from deep observations. Vazza et al. (2012) showed, with cosmological simulations, that the kinetic energy dissipated at

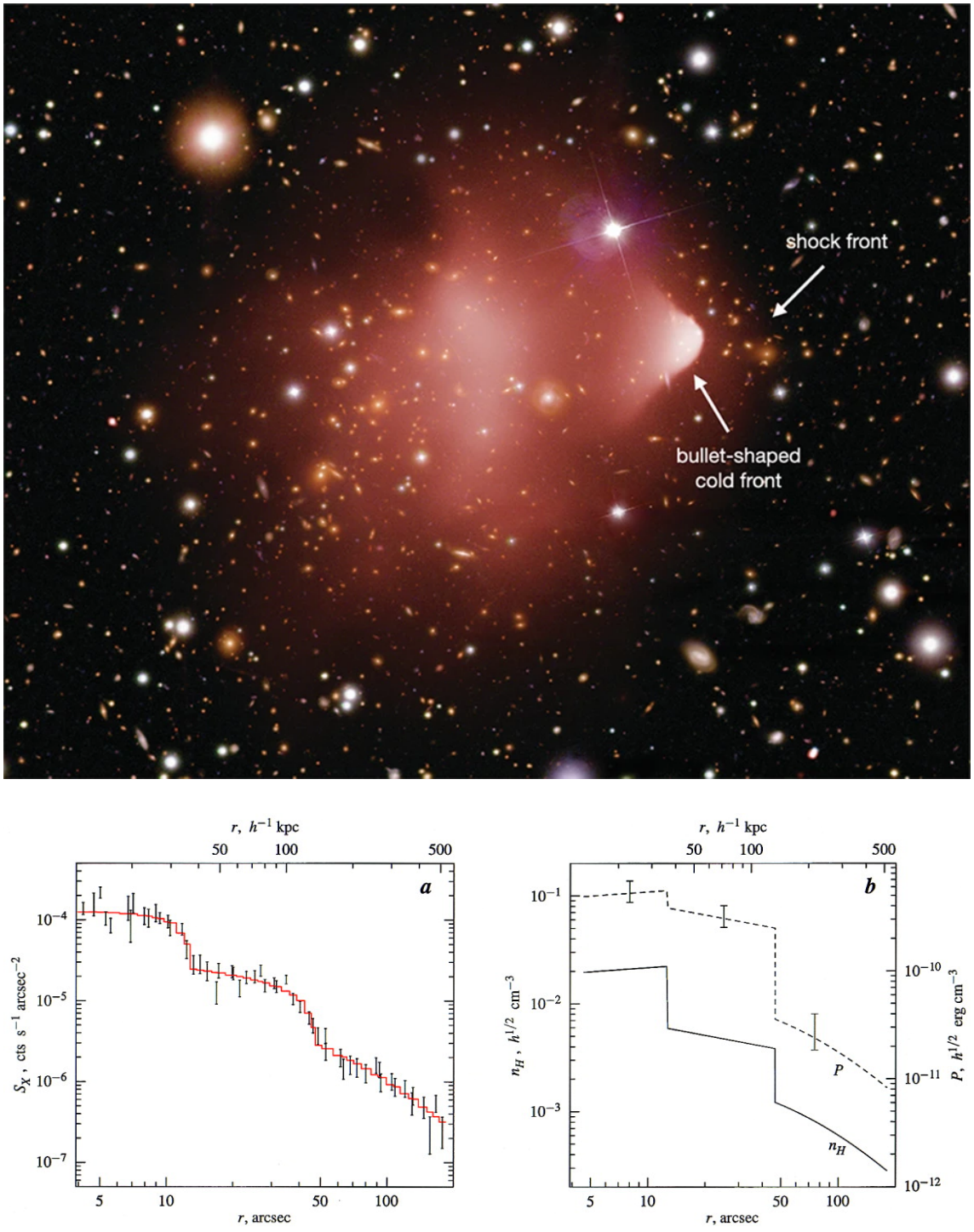

Figure 1.6: Merging cluster 1E 0657-56, or the "Bullet" cluster. **Top:** Composite X-ray and optical image taken from ZuHone & Su (2022). The X-ray image comes from Markevitch et al. (2002) and the optical from Clowe et al. (2004). **Bottom:** Radial surface brightness (left) and density (right) graphs centred on the bullet and directed westward from Markevitch et al. (2002). The density graph also includes an approximate gas pressure model, as a dashed line.

shocks increases sharply with radius, within the central ~Mpc. The lack of RRs close to the cluster centre is likely a consequence of this.

In a binary merger, a pair of shocks should be launched outwards, along the merger axis, after dark matter core passage. Many examples of double radio relics (dRRs), i.e. RRs with another, diametrically-opposed, RR in the same cluster, have been discovered in merging clusters. For example, PSZ1 G108.18-11.53 (de Gasperin et al., 2015), Abell 1240 (Bonafede et al., 2009b) and PLCK G287.0+32.9 (Bagchi et al., 2011). However, only a fraction of RR-hosting clusters are observed to host dRRs. Simulations by van Weeren et al. (2011) suggest that the lack of dRRs is driven by the merger mass ratio and viewing angle of the merger. Only major mergers, with a mass ratio 1:1 - 1:3, that are on, or close to, the plane of the sky will produce observable dRRs. The combination of the merging subcluster mass distribution obtained from weak-lensing analysis and redshift measurements of cluster-member galaxies allows one to constrain the three-dimensional geometry of a merger. Golovich et al. (2019a,b) utilised this for a sample of 29 RR-hosting clusters and found that the merger axis of those with dRRs was indeed on, or close to, the plane of the sky. Since the merger axis is close to perpendicular to the line of sight, dRRs are ideal to study the properties of relics and mergers, with minimal projection effects.

1.2.2.2 Diffusive shock acceleration

The preferred model used to explain the acceleration of electrons which produce RRs is first-order Fermi acceleration (Fermi I), also known as diffusive shock acceleration (DSA; Bell, 1978; Enßlin et al., 1998). In DSA, particles with scattering lengths greater than the shock width are trapped and scatter back and forth across the shock front off magnetic inhomogeneities, gaining energy each time. Eventually, particles are able to escape downstream through convection. The process forms a population of cosmic-ray electrons with a power-law spectrum of the form $f(p) = Kp^{-(\delta_{inj}+2)}$ in momentum space. The injection slope of the accelerated electrons, δ_{inj}, depends only on the shock Mach number, through

$$\delta_{inj} = 2\frac{\mathcal{M}^2 + 1}{\mathcal{M}^2 - 1}. \tag{1.19}$$

δ_{inj} is related to the observable spectral index at the site of acceleration, α_{inj}, by $\alpha_{inj} = (\delta_{inj} - 1)/2$. However, it is often challenging to measure α_{inj}, and the volume-integrated spectral index, $\alpha = \alpha_{inj} + 1/2$, is often used instead (Kardashev, 1962). This allows for a method of measuring the shock Mach number independent of the X-ray-derived value. Comparisons of radio- and X-ray-derived Mach numbers, $\mathcal{M}_{radio}$ and $\mathcal{M}_{xray}$ respectively, show that $\mathcal{M}_{radio}$ is often greater than $\mathcal{M}_{xray}$, which could point to a problem with DSA. The discrepancy could alternatively be explained by observational effects. Ha et al. (2018a) found that the CR-energy-weighted Mach number is greater than that weighted by the kinetic energy, and both observations and cosmological simulations have shown that the structure of RRs is complex, representing a distribution of Mach numbers (Hoeft et al., 2011; Skillman et al., 2013; de Gasperin et al., 2022). Radio-derived Mach numbers are therefore biased high, since they are biased towards the parts of the shock with the highest Mach numbers. Unfavourable viewing angles for X-rays (Akamatsu

et al., 2017), re-acceleration of fossil CRes (Pinzke et al., 2013; Kang & Ryu, 2016) and superdiffusive shock acceleration (Zimbardo & Perri, 2018) have also been proposed as possible explanations for the discrepancy, amongst others. For a comprehensive discussion of the systematic uncertainties in $\mathcal{M}_{radio}$, see van Weeren et al. (2016a) and Hoang et al. (2017), and Akamatsu et al. (2017) for those in $\mathcal{M}_{xray}$.

In general, DSA is successful in reproducing many of the properties of RRs. The morphology, radio flux and spectral profiles in simulations of individual RRs produced by DSA are, in general, in agreement with observations (e.g. Kang et al., 2012). Cosmological simulations of RR populations are also able to reproduce most of the statistical properties of RRs, such as the distribution of longest linear sizes (LLSs) and radio powers (e.g. Nuza et al., 2017; Brüggen & Vazza, 2020). Unlike RHs, RRs have inhomogeneous spectral index distributions. RRs are observed with relatively flat spectra at their outermost edge, i.e. the edge furthest from the cluster centre, which steepens towards the cluster centre. This is what would be expected from radio emission produced from a site of continuous particle acceleration which is travelling outwards (shock front), leaving behind a trail of particles downstream which are no longer undergoing acceleration and radiate away energy in the form of synchrotron and IC radiation. The polarisation properties of RRs are also in line with expectations for shock acceleration. Since the magnetic field lines should be aligned along the shock front by compression, one would expect that RRs are highly polarised and that the magnetic field vectors lie parallel to the shock surface (Enßlin et al., 1998). RRs are typically observed with relatively high polarisation fractions ($\gtrsim 20-60\%$) (e.g. Govoni & Feretti, 2004; Bonafede et al., 2009b; Hoang et al., 2017). Fig. 1.7 shows the the spectral index profile and polarisation intensity of the northern RR in CIZA J2242.8+5301, also known as the "Sausage" relic. The spectral index steepens from the shock front at the northern edge of the RR towards the cluster centre (southwards). The RR is polarised and the polarisation electric field vectors are aligned approximately perpendicular to the shock front, indicating that the magnetic field lines are aligned along the shock front.

However, there is growing evidence that DSA is unable to fully reproduce the observed properties of RRs. As well as CRes, which produce the synchrotron radiation we observe as RRs, galaxy cluster shocks should also accelerate CRps. As for the hadronic model of RHs (Sec. 1.2.1), these CRps should collide with thermal ICM protons and produce γ-rays (e.g. Blasi & Colafrancesco, 1999). To date, there have been no confirmed γ-ray detections from cluster shocks (e.g. Ackermann et al., 2010). Under relatively optimistic assumptions, Vazza & Brüggen (2014) showed that DSA is expected to produce a γ-ray flux above the upper limits set by the *Fermi* satellite. However, there is evidence that CRps are preferentially accelerated by quasi-parallel ($Q_{\parallel}$) shocks, i.e. those with an upstream magnetic field $\leq 45^{\circ}$ to the shock normal (Ha et al., 2018b). Conversely, CRes are preferentially accelerated by quasi-perpendicular ($Q_{\perp}$) shocks. This may imply that CRp acceleration by cluster shocks is less efficient than previously thought and reduce the tension with γ-ray observations.

Another unresolved issue with DSA is with the required CRe acceleration efficiency. Botteon et al. (2020a) studied a number of RRs which had both good radio and X-ray observations and calculated the electron acceleration efficiency required, as a function of

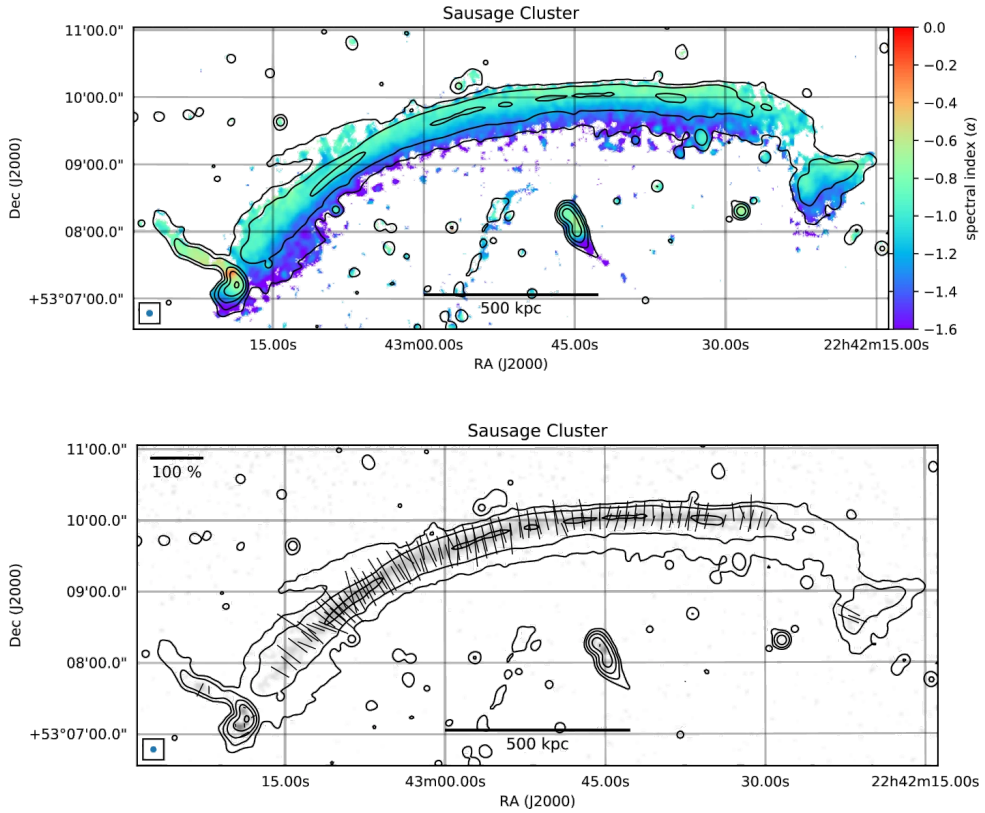

Figure 1.7: Radio relic in merging cluster CIZA J2242.8+5301, or the "Sausage" relic. Image taken from van Weeren et al. (2019), using data from Di Gennaro et al. (2018, 2021). **Top:** Spectral index map of the relic between 0.15 – 3GHz. **Bottom:** Polarised intensity image, overlaid with polarisation electric field vectors.

magnetic field strength at the shock, to produce observed RR properties and shock Mach numbers. They found that, for most of the RRs in their sample, DSA from the thermal pool required either a magnetic field strength much greater than those typically observed in RRs, or extremely large CRe acceleration efficiencies incompatible with DSA. The CR acceleration in shocks is constrained by observations of supernovae (SN). The strong ($\mathcal{M} \sim 10^3$) shocks from SN are able to accelerate CRs with an efficiency of $\eta \sim 0.1$. The weaker shocks in galaxy clusters are not expected to be able to accelerate CRs with such efficiency, but a number of RRs in Botteon et al. (2020a) required similar, or greater, η to those observed in SN shocks.

A simple solution to this problem is that DSA remains the physical mechanism producing RRs, but that the population of electrons accelerated are mildly-relativistic fossil CRe, instead of thermal electrons. In this re-acceleration model, CRes created during cluster assembly, or from AGN activity, which have cooled through radiative and Coulomb losses to $10 \lesssim \gamma \lesssim 10^4$ provide the seed population to be subsequently re-accelerated at a shock, producing a RR. For weak shocks, such as cluster merger shocks, RRs produced by re-accleration should dominate over those produced by acceleration from the thermal pool (Pinzke et al., 2013). Populations of fossil CRes within the ICM should be relatively common (e.g. Sarazin, 1999; Petrosian, 2001; Pinzke et al., 2013). They are however challenging to observe, owing to their extremely steep radio spectra, but with the

advent of ultra-low frequency radio observations with LOFAR, there have been a handful of discoveries of fossil plasma within the ICM (de Gasperin et al., 2017; Mandal et al., 2020). Another potential source of CRes available to be re-accelerated by merger shocks are those from the tails of radio galaxies. There have been a number of observations showing a RR coincident with a radio galaxy (e.g. Bonafede et al., 2014; Shimwell et al., 2015). However, the most compelling case comes from van Weeren et al. (2017), who found morphological, spectral and polarimetric evidence of re-acceleration of the tail of a radio galaxy from a shock. They found that the tail of a cluster-member radio galaxy in the merging cluster Abell 3411-3412 connected with the radio emission of a RR. The radio spectral map indicates that the radio emission steepens along the radio galaxy tail, as expected for ageing plasma losing energy through radiative and IC losses (see Sec. 1.3.1). The spectrum subsequently flattens at the inner edge of the RR and continues towards the RR outer edge, in line with a shock which is propagating away from the cluster centre and has passed through the tail. This provides strong evidence for re-acceleration of CRes at shocks which can produce RRs. However, the number of observed RRs with spatially coincident radio galaxies is low, so it remains unknown if such a scenario can provide a general solution.

1.2.2.3 Correlations

Similar to RHs, attempts have been made to study the statistical properties of RRs. Due to the low occurrence of RRs, studies have been mostly limited to creating samples from the literature, with the cluster and RR properties being measured by different methods and observatories. van Weeren et al. (2009) studied a sample of 26 RRs (all those observed at the time) and found that the LLS correlates with the distance from the cluster centre. This implies that the shock surface expands as it travels. They also found a correlation between the LLS and the integrated spectral index of the RRs in their sample. However, unlike the LLS - cluster centre distance correlation, this finding was not corroborated by Bonafede et al. (2012), who limited their analysis to only dRRs, or de Gasperin et al. (2014). The sample of van Weeren et al. (2009) was contaminated with radio phoenices, which are clouds of fossil plasma from previous bursts of AGN activity that have been revived by subsequent compression (see van Weeren et al., 2019). These sources have steep spectra and are typically located near the cluster centre, so are the likely source of the LLS - α correlation. de Gasperin et al. (2014) also found, similar to RHs, that the radio power of RRs correlates with the cluster mass. I.e. more massive clusters are able to produce more powerful RRs. This is in line with findings by Feretti et al. (2012) that the radio power scales with the cluster X-ray luminosity. This implies that the energy dissipated into shock acceleration of CRes depends on the total energy budget of a merger. Fig. 1.8 shows the RR scaling relations found by de Gasperin et al. (2014). Simulations of cluster mergers aimed at reproducing the statistical properties of RRs have however suggested that observations are missing populations of low-power RRs, particularly in low-mass clusters, which may affect the validity of such scaling relations (Nuza et al., 2017; Brüggen & Vazza, 2020).

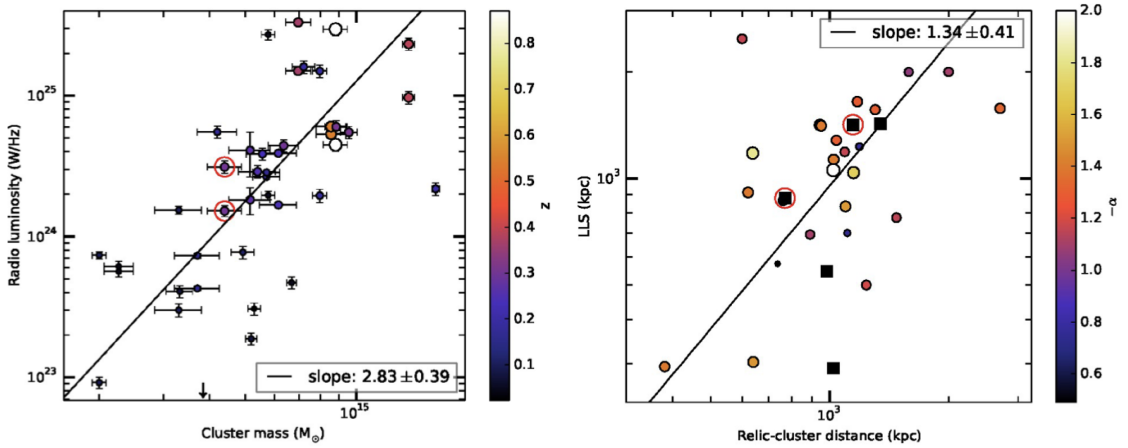

Figure 1.8: Radio relic scaling relations found by de Gasperin et al. (2014). **Left:** Radio power vs. cluster mass. **Right:** longest linear size vs. distance from cluster centre.

1.2.3 The connection between halos and relics

The connection of both RHs and RRs to galaxy cluster mergers is well-established. One may therefore reasonably expect that all merging clusters host both RRs and RHs. However, whilst some clusters are known to host both, many host either one or the other, though there are many more detections of RHs than RRs. Fig. 1.9 shows radio images of PSZ2 G181.06+48.47 and PSZ2 G107.10+65.32 (Abell 1758). PSZ2 G181.06+48.47 hosts a dRR pair in the NE/SW, but no RH. PSZ2 G107.10+65.32 consists of two separate clusters, in the north and south, each undergoing its own merger along the W/E axis. Both subclusters host a RH, whilst the southern subcluster also hosts a RR on its eastern side.

One cause for the discrepancy could be from the respective dependence of merger-induced turbulence and DSA on the energetics of a merger. The turbulence responsible for the generation of RHs is injected directly by the merger. The cutoff frequency of the RH spectrum is therefore dependent on the merger energetics (Cassano & Brunetti, 2005). If the generation of RRs is less dependent on the energetics, clusters which host RRs, but not RHs, may correspond to the least energetic mergers which were unable to generate sufficient turbulence to produce a visible RH. In this case, it might be expected that only the most dynamically-disturbed clusters host RHs. Alternatively, since RRs and RHs are produced by different mechanisms which act on different timescales and lose energy through radiative losses, there may be an evolutionary effect on the discrepancy. The kinetic energy dissipated by a shock increases as it propagates outwards (Vazza et al., 2012), implying that a significant amount of time post-merger is required for the generation of relics. ICM turbulence must also cascade down to scales at which it can (re-)accelerate CRe, and simulations by Donnert et al. (2013) have shown that the power of RHs evolves throughout a merger.

In order to understand the difference between RR-hosting clusters with and without RHs, Bonafede et al. (2017) studied a sample of 15 merging clusters, 8 of which host a RH and 7 which do not. All of the clusters were chosen to be those which host dRRs, since their merging axis is well-constrained and projection effects are minimised. In their

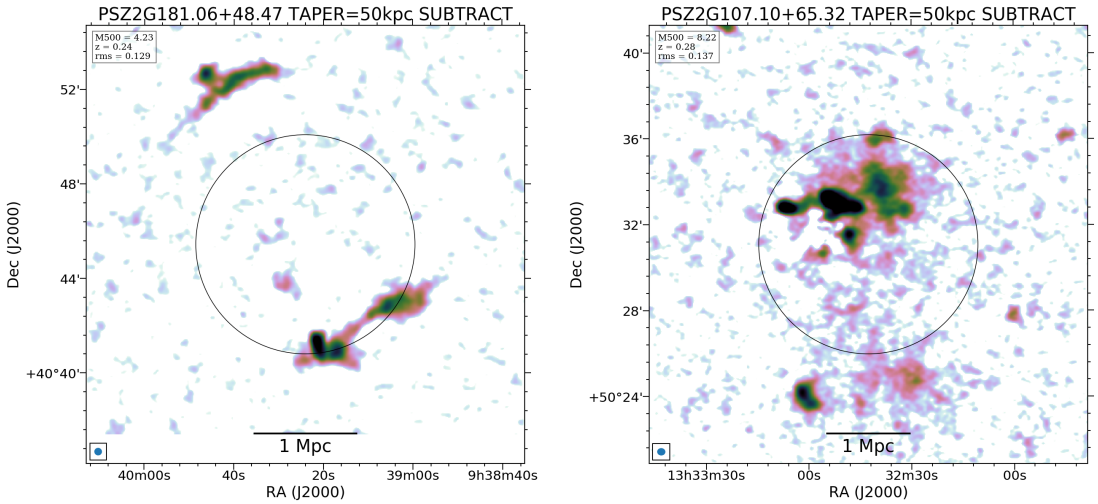

Figure 1.9: Radio images of merging galaxy clusters made using LOFAR data release 2 data, from Botteon et al. (2022). **Left:** PSZ2 G181.06+48.47. **Right:** PSZ2 G107.10+65.32 (Abell 1758), which consists of two separate subclusters, each undergoing its own merger.

analysis, they assessed whether the existence of the two populations could be explained by the cluster morphological disturbance, the merging mass ratio or the time since the merger, but did not find any conclusive evidence for any of them. The underlying reason for the different cluster populations remains unknown.

Some clusters contain RHs bound by shock fronts, for example Abell 520 (Markevitch et al., 2005), Coma (Brown & Rudnick, 2011), 1E 0657-56 ("Bullet" cluster; Shimwell et al., 2014) and the southern edge of 1RXS J0603.3+4214 (van Weeren et al., 2016a). There has been no spectral index steepening observed downstream of the shock fronts, as would be expected if CRes accelerated by DSA at the shock front encountered, and were re-accelerated by, turbulence injected by the merger further downstream. Additionally, Shimwell et al. (2014) found no polarised emission associated with the shock-RH region in 1E 0657-56. The radio emission at these edges could therefore come exclusively from Fermi II processes, implying that shocks can, in some cases, generate significant turbulence immediately downstream of the shock front (Fujita et al., 2015). Evidence of downstream turbulence has also been found in other RRs not associated with a RH. The characteristic widths of the RRs in Abell 3667 (de Gasperin et al., 2022) and the northern RRs in 1RXS J0603.3+4214 ("Toothbrush" relic; Kang et al., 2017; de Gasperin et al., 2020) and CIZA J2242.8+5301 ("Sausage" relic; Kang, 2016) have been found to be too large to be explained by CRes that are accelerated by DSA at the shock front and subsequently radiate away their energy through synchrotron and IC losses (see Sec. 1.3.1). Re-acceleration by turbulence downstream may be able to explain the discrepancy. Additionally, examination of the polarised emission in the "Sausage" relic by Di Gennaro et al. (2021) showed that the polarisation fraction decreases in the downstream region, in line with a turbulent magnetic field of strength $B \sim 6\mu$G.

1.3 Radio observations

1.3.1 Synchrotron emission and radio spectra

The mechanisms responsible for acceleration of particles in the ICM to relativistic speeds typically produce CRes with a power-law energy distribution, i.e. $n(E) \propto E^{\delta} dE$, where δ is a constant which depends on the acceleration mechanism and other properties at the site of acceleration, such as the shock Mach number in the case of DSA (Sec. 1.2.1 & Sec. 1.2.2). As CRes move within the magnetic field of the ICM, they experience an acceleration due to the Lorentz force, producing synchrotron radiation. For optically-thin radio sources, i.e. those emitting synchrotron radiation at frequencies high enough that synchrotron self-absorption can be neglected, the resulting flux spectrum is also a power-law

$$S_{\nu} \propto \nu^{\alpha}, \tag{1.20}$$

where α is the spectral index, which depends only on the CRe spectral distribution index, δ, through $\alpha = \frac{\delta-1}{2}$. The spectral index can be measured directly with radio observations by taking measurements at two frequencies, ν_1 and ν_2, through

$$\alpha = \frac{log(S_1/S_2)}{log(\nu_1/\nu_2)}. \tag{1.21}$$

Many sources in the ICM have steep integrated spectra, i.e. $\alpha \lesssim -1$, which can make them challenging to observe at higher frequencies. Studies are therefore typically limited to low frequencies ($\lesssim$ 2GHz).

CRes in the ICM also interact with background radiation, in particular CMB photons, via Thomson scattering. The scattering of photons off CRes converts CRe kinetic energy into IC radiation by upscattering the photons to higher energies. Both synchrotron and IC losses from CRes follow

$$\frac{\mathrm{dE}}{\mathrm{dt}} = \frac{4}{3}\sigma_T c \beta^2 \gamma^2 U, \tag{1.22}$$

where σ_T is the Thomson cross-section, $\beta \equiv v/c$, γ the Lorentz factor and U represents either the magnetic energy density, in the case of synchrotron radiation, or the radiation energy density, for IC. Importantly, the rate of energy loss in both cases is strongly dependent on the CRe energy. This means that, in the absence of another source of acceleration, the flux spectra of ageing plasma will steepen over time, as the higher energy CRes radiate away their energy faster. Consequently, low-frequency observations of galaxy clusters are required to observe and understand the oldest relativistic plasma in the ICM, such as fossil electron populations and the furthest downstream regions of RRs (see Sec. 1.2.2).

Due to these energy losses, the characteristic lifetime, t_{age}, at observing frequency, ν, of GeV CRes, which produce synchrotron emission, is given by

$$t_{age} \approx 3 \times 10^{10} \frac{B^{1/2}}{B^2 + B_{CMB}^2} \frac{1}{\sqrt{\nu(1+z)}}, \tag{1.23}$$

where $B_{CMB} = 3.24(1+z)^2$ μG is the equivalent magnetic field strength of the CMB at redshift, z. In the ICM, $B \sim \mu$G, giving $t_{age} \lesssim 10^8$yr. The distance over which synchrotron-emitting CRes in the ICM can diffuse during the characteristic lifetime of the electrons is therefore $\sim$ 1pc (Bagchi et al., 2002). Diffuse Mpc-scale radio emission observed in clusters, such as RRs and RHs, must therefore be driven by continuous in-situ acceleration, since CRes accelerated at one location would not be able to diffuse far enough before becoming too faint to observe (Jaffe, 1977).

1.3.2 Radio interferometry

The angular resolution, θ, of a single-dish radio telescope is diffraction-limited, i.e. $\theta \sim \frac{\lambda}{D}$, where λ is the observing wavelength, and D is the dish diameter. At long radio wavelengths, an unfeasibly large dish would be required to reach sub-arcsecond resolution. The solution to this problem is to use multiple radio telescopes simultaneously and combine the radio signal they receive, i.e. radio interferometry. This has the additional effect of increasing the sensitivity of the telescope.

An array of N telescopes can be treated as $N(N-1)/2$ pairs of antennas, each with a separation, or baseline, $\vec{b}$. The angular resolution of such an array is then $\theta \sim \frac{\lambda}{b_{max}}$, where b_{max} is the longest baseline of all elements in the array. A complex correlator then multiplies and time-averages the voltage received by the individual antennas for each pair of antennas. The resultant response, or visibility, $\mathcal{V}$, to a brightness distribution, $I(\hat{s})$, in direction of the unit vector $\hat{s}$, with components (l, m, n) is given by

$$\mathcal{V} = \int\int I(\hat{s}) e^{\frac{-2i\pi}{\lambda}\vec{b}\cdot\hat{s}} d\Omega, \tag{1.24}$$

which becomes a two-dimensional Fourier transform,

$$\mathcal{V}(u,v) = \int\int \frac{1}{\sqrt{1-l^2-m^2}} I(l,m) e^{-2i\pi(ul+vm)} dl dm, \tag{1.25}$$

for the baseline $\vec{b} = (\lambda u, \lambda v, \lambda w)$, when the distance in the direction of $\hat{s}$, $w = 0$. The source brightness distribution, $I(l,m)$, can then be obtained by inverting this. Fig. 1.10 shows how the u, v, w and l, m coordinate systems relate to each other for a simple interferometer consisting of two antennas, separated by baseline D_λ, observing a source with brightness distribution, $I(l,m)$. Keeping w small enough that Eq. 1.24 can be approximated as a 2D Fourier transform would require a small field-of-view, which would limit the capability of radio interferometers to produce wide-field images. One solution for this is to split the sky up into facets, effectively removing the effect of w, imaging each with 2D Fourier transforms, and combining the results to produce a full image.

Another advantage of radio interferometers is that one can balance the sensitivity to both compact and diffuse emission. To study diffuse emission in galaxy clusters, this is essential, since the low surface brightness spread over large cluster volumes requires the high sensitivity to large physical scales given by shorter baselines to observe. However, higher resolution is also required to understand the smaller-scale cluster physics at play.

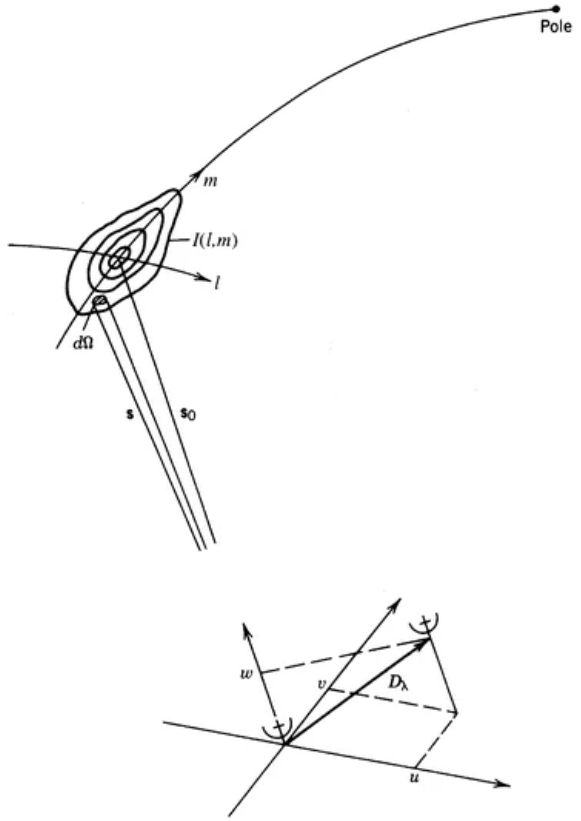

Figure 1.10: Geometry of the relationship between an interferometer formed of a single pair of antennas with baseline D_λ and a source with brightness distribution $I(l, m)$ from Thompson et al. (2017).

Additionally, there are often many compact sources, such as radio galaxies, close to, or along the line of sight of the diffuse emission one is interested in. Excising such compact emission requires long baselines, which are much more sensitive to smaller angular scales. In fact, diffuse emission is often not observable at all if one images with data from only the longer baselines. With the smaller synthesised beam, i.e. the response of an interferometer to a point source in the phase centre, created by longer baselines it can become impossible to distinguish the low surface brightness emission from the noise.

There are many different effects that can impact the actual complex visibility measured by an interferometer, such as antennas which have varying responses to a radio signal over time or frequency. To ensure that the data measured are representative of the real sky, one or more calibrator sources, with known brightness distributions, I, must also be observed and compared against the actual measurements. The goal is to use these sources to solve for the true visibility, V_{ij}^{true}, from the observed visibility, V_{ij}^{obs} for each baseline ij, using the radio interferometry equation

$$V_{ij}^{obs} = M_{ij} B_{ij} G_{ij} D_{ij} E_{ij} P_{ij} T_{ij} V_{ij}^{true}, \tag{1.26}$$

where $M_{ij}, B_{ij}, G_{ij}, D_{ij}, E_{ij}, P_{ij}$ and T_{ij} are the baseline errors, bandpass response, gain amplitude and phase, instrumental polarisation, elevation errors, paralactic angle change and opacity and path length variation, respectively.

One significant influence on V_{ij}^{obs} at low radio frequencies is the propagation delay introduced by the changing refractive index, n, of the ionosphere (Intema et al., 2009; Mangum & Wallace, 2015; de Gasperin et al., 2018). For frequencies, ν, much greater than the plasma frequency of the ionosphere ($\sim 1 - 10$MHz), the refractive index can be calculated using Taylor expansion as

$$n \approx 1 - \frac{q^2}{8\pi^2 m_e \epsilon_0} \frac{n_e}{\nu^2} \pm \frac{q^3}{16\pi^3 m_e^2 \epsilon_0} \frac{n_e B \cos\theta}{\nu^3}, \tag{1.27}$$

where q is the electron charge, θ is the angle between the Earth's magnetic field, B, and the direction of propagation of the electromagnetic wave, n_e is the number density of free electrons and ϵ_0 is the vacuum electric permittivity. Higher order terms are not included, since they can generally be neglected for frequencies above $\sim$ 40MHz. At ~GHz frequencies, only the first term, related to dispersive delay, plays a significant role. However, at lower frequencies, higher order terms, such as the second term, related to Faraday rotation, must be taken into account.

Even after calibration against a known source, there may remain residual errors. For example, bright sources in the field of view can leave ripples, or artefacts which introduce non-real emission into a radio image. The solution is self-calibration, in which the data is used iteratively to calibrate itself. First, a "dirty" image of the sky is created from the visibilites calculated by calibration against calibrator radio sources by solving for I in Eq. 1.24. From this image, a model of the sky in uv-space is created. Small changes in the amplitude and phase of the measured visibilities can then be removed by the iteratively calibrating them against the model created and creating a new sky model from the image produced. Eventually, one is left with a "clean" image, which represents the real sky brightness distribution.

As well as the total intensity of radio emission, interferometers are able to measure the degree of polarisation. The polarisation state can be described by the Stokes parameters, I, Q, U and V (Stokes, 1851), given by

$$\begin{aligned} I &= E_x^2 + E_y^2, \\ Q &= E_x^2 + E_y^2, \\ U &= 2E_x E_y \cos\delta, \\ V &= 2E_x E_y \sin\delta, \end{aligned} \tag{1.28}$$

where $E_{x,y}$ is the magnitude of the electric field vector in the x and y plane, respectively, and $\delta \equiv \delta_y - \delta_x$ is the offset between the electric field vectors. I is the total intensity, whilst the polarised emission is separated into linear (Q and U) and circular polarisation (V). There is not expected to be any circularly polarised emission ($V = 0$) from diffuse radio emission in galaxy clusters, so the fractional polarisation of a source can be computed as

$$p = \frac{\sqrt{Q^2 + U^2}}{I}, \tag{1.29}$$

and the polarisation angle,

$$\chi = \frac{1}{2} \arctan \frac{U}{Q}. \tag{1.30}$$

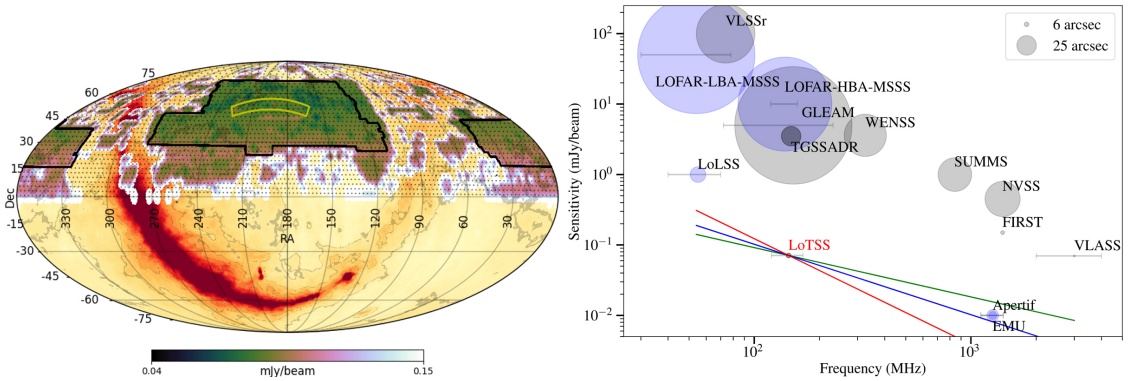

Figure 1.11: **Left:** Sky coverage of LoTSS as of Data Release 2 from Shimwell et al. (2022). The area covered by Data Release 1 and Data Release 2 are shown in the yellow and black boxes, respectively. **Right:** Graph comparing the frequency ranges and sensitivity of different radio surveys from Shimwell et al. (2019). The radius of the shaded circles is proportional to the survey resolution.

In this way, radio observations can quantify the degree of polarisation of a source and in which direction the magnetic field lines are oriented.

1.3.3 LOFAR

The Low-Frequency Array (LOFAR) is a radio interferometer with a core of 24 stations located in the Netherlands, with a further 14 remote stations also in the Netherlands. As of May 2023, there are 14 international stations spread across Europe, which add extremely long baselines, allowing for observations with sub-arcsecond resolution. Each station is comprised of 96 low-band antennas (LBA), which operate at frequencies between 10 - 90 MHz and 48 - 96 high-band antennas (HBA), which measure frequencies between 110 - 240 MHz. The large range of baselines spanned is designed to best cover the *uv* plane and provide sensitivity to compact and diffuse emission (van Haarlem et al., 2013). The LOFAR instrument was designed with a broad range of scientific goals in mind, from the search for signals from the epoch of re-ionisation and study of AGNs and other galaxies, to transient sources in our own galaxy and solar weather.

Unlike most radio interferometers, which can be pointed in the direction of a particular source, the LOFAR antennas are fixed in place. LOFAR is instead "steered" by introducing an artificial time delay, corresponding to a particular sky direction, into the dataset. In this way, it is possible for LOFAR to observe in many directions at once by adding in different time delays. This, combined with its large field of view, with a full width half maximum of $\sim 4°$, makes LOFAR ideal to efficiently undertake deep, low-frequency radio sky surveys.

To this end, the ongoing LOFAR Two-metre Sky Survey (LoTSS; Shimwell et al., 2017) aims to map the entire northern sky at low frequency (120 - 168 MHz) with a resolution of 6" and, with a median rms sensitivity of $83 \mu \text{Jybeam}^{-1}$ at the central frequency 144 MHz, i.e. a sensitivity a factor of ~ 10 better than the most sensitive wide-area radio-continuum surveys. In the LoTSS DR1 and DR2, full polarimetric data of 2% and 27% of the

northern sky were released, respectively, containing >4 million radio sources, the majority of which had not previously been detected (Shimwell et al., 2019, 2022). The DR1 area is entirely encompassed by the DR2 area and is analysed with an improved data reduction pipeline, most importantly with regards to the fidelity of diffuse emission and the greater dynamic range of DR2. The corresponding ultra-low frequency LOFAR LBA Sky Survey (LoLSS; de Gasperin et al., 2021, 2023) will produce 15" resolution images of the entire northern sky above 24° declination, at frequencies of 41 - 66 MHz. The first data release of LoLSS covers 650 deg^2 and contains 42463 detected radio sources, with a characteristic rms sensitivity of 1.55mJybeam^{-1}. Fig. 1.11 shows the coverage of the ongoing LoTSS survey. The DR1 and DR2 coverages are shown in yellow and black, respectively. It also shows the sensitivity, frequency coverage and resolution of a number of notable radio surveys. The LoTSS and LoLSS surveys have considerably better sensitivity and resolution than those at comparable frequencies and provide an unprecedented view into the least energetic, steepest-spectrum radio sources.

1.4 Aims and outline of this thesis

In this thesis I focus on the study of radio relics in the ICM, generated by shock waves induced by galaxy cluster mergers. In this regard, I used low-frequency radio observations to address the following questions:

- Can lobes of previous AGN activity provide seed electrons to produce radio relics, and are the properties of the relics altered?
- What are the statistical properties of radio relics as a population? Do the scaling relations previously reported extend to low frequency?
- Is DSA the only CRe acceleration mechanism present in radio relics, or does turbulence also play a role?
- What is the connection between radio relics and radio halos?

This thesis is organised as follows. In Chapter 2 I present Jones et al. (2021), *Radio relics in PSZ2 G096.88+24.18: A connection with pre-existing plasma*. In this paper, a double radio relic system is investigated using surface brightness, spectral index and polarisation maps created from 1.5GHz VLA and 140MHz LOFAR radio observations, as well as X-ray surface brightness *Chandra* data. A connection is discovered in radio between a cluster-member galaxy and the southern relic, which coincides with the brightest region of the relic. The relic also has a complex spectral index distribution and a very low polarisation fraction. This is interpreted as evidence for re-acceleration of a lobe of previous AGN activity, which has resulted in a turbulent region downstream of the shock front. Additionally, the presence of a radio halo, reported at low-significance by de Gasperin et al. (2014), is investigated. However, the higher-sensitivity LOFAR images indicate that the source is in fact a steep-spectrum tail of a cluster-member radio galaxy.

In Chapter 3 I present Jones et al. (2023), *The Planck clusters in the LOFAR sky VI. LoTSS-DR2: Properties of radio relics*. In this paper, the properties of radio relics contained in the LoTSS-DR2 144MHz radio survey which are hosted by *Planck*-detected clusters are investigated. The heterogeneity of the relics necessitated the development of methods to measure their properties in a uniform and fair manner. With these measurements, it was possible to determine the statistical properties of radio relics, including their occurrence, scaling relations, locations and connection to radio halos. The longest linear size of radio relics is found to correlate with its distance from the cluster centre, and the results tentatively support a correlation between radio power and cluster mass. It was also discovered that the downstream width of radio relics is systematically too large to be explained by a single site of acceleration at the shock front.

In Chapter 4 I summarise my work in the context of my overarching aims and how future work could expand upon the findings presented here.

Appendix A contains the radio relic properties, and their associated errors, measured and used in Jones et al. (2023).

Chapter 2

Radio relics in PSZ2 G096.88+24.18: A connection with pre-existing plasma

A. Jones, F. de Gasperin, V. Cuciti, D. N. Hoang, A. Botteon, M. Brüggen, G. Brunetti, K. Finner, W. Forman, C. Jones, R. Kraft, T. Shimwell, R. J. van Weeren

Published in Monthly Notices of the Royal Astronomical Society, 21 May 2021

Abstract

Giant radio relics are arc-like structures of diffuse, non-thermal synchrotron radiation that trace shock waves induced by galaxy cluster mergers. The particle (re-)acceleration mechanism producing such radio relics is unclear. One major open question is whether relics can be formed directly from a population of thermal seed electrons, or if pre-existing relativistic seed electrons are required. In some cases AGN can provide such a population of sub-GeV electrons. However, it is unclear how common this connection is. In this paper we present LOFAR 140 MHz and VLA L-band radio observations, as well as *Chandra* data of PSZ2 G096.88+24.18, a merging galaxy cluster system hosting a pair of radio relics. A large patch of diffuse emission connects a bright radio galaxy with one of the relics, likely affecting the properties of the relic. We find that the most plausible explanation for the connection is that the merger shock wave has passed over an AGN lobe. The shock passing over this seed population of electrons has led to an increased brightness in the relic only in the region filled with seed electrons.

2.1 Introduction

Mergers of galaxy clusters are energetic astronomical events in which a fraction of the energy budget is dissipated into the acceleration of charged particles within the hot,

magnetised intra-cluster medium (ICM, Brunetti & Jones, 2014). This process results in the formation of Mpc-scale radio synchrotron emission that is broadly split into two categories: giant radio halos and relics (also known as radio shocks; see van Weeren et al., 2019, for a review). Giant radio halos are generally characterised by low surface brightness, unpolarised emission spanning the cluster centre, approximately tracing the thermal bremsstrahlung X-ray radiation emitted by the baryonic mass distribution of the ICM. Giant radio halos are thought to be generated by turbulent (re-)acceleration of relativistic electrons injected into the ICM by mergers. (e.g. Brunetti et al., 2001; Petrosian, 2001). Radio relics are observed primarily as elongated arcs of polarised emission in cluster outskirts. They are thought to trace merger shock waves as they propagate through the ICM (e.g. Enßlin et al., 1998; Roettiger et al., 1999; van Weeren et al., 2010). Observations of discontinuities in the thermodynamical properties of the ICM (density, pressure, temperature), coinciding with relics, support this scenario (e.g. Finoguenov et al., 2010; Bourdin et al., 2013; Akamatsu et al., 2017; Urdampilleta et al., 2018). Diffusive Shock Acceleration (DSA, see Blandford & Eichler, 1987, for a review) is the most likely mechanism driving the particle acceleration at shock fronts. It can explain many properties of relics, such as their morphologies, radio fluxes, polarisation properties and the power-law energy distribution of cosmic rays (Hoeft & Brüggen, 2007; Kang et al., 2012; Brüggen & Vazza, 2020). Observations of some cluster relics suggest that they can be explained by diffusive shock acceleration of electrons from the thermal pool (standard DSA), as in e.g. Abell 2249 (Locatelli et al., 2020), El Gordo and Abell 521 (Giacintucci et al., 2008; Botteon et al., 2016b, 2020a). However, in general this is not the case. The Mach numbers of shocks generated by galaxy cluster mergers are typically low ($\mathcal{M} \lesssim 5$), so the acceleration efficiencies required to reproduce the luminosity of radio relics are too large to be explained by standard DSA (e.g. Kang et al., 2012; Brunetti & Jones, 2014; Vazza & Brüggen, 2014; Eckert et al., 2016; Botteon et al., 2020a). Moreover, in the DSA scenario gamma rays should be produced by collisions between shock-accelerated protons and thermal ICM protons. However, calculations suggest that an abnormally high electron-proton ratio at cluster shocks would be required to reconcile relics with the non-detection of gamma rays from clusters (Ackermann et al., 2010; Vazza & Brüggen, 2014).

The re-acceleration of a pre-existing population of sub-GeV electrons could mitigate the requirement of high acceleration efficiency at weak cluster shocks (e.g. Markevitch et al., 2005; Kang et al., 2012; Pinzke et al., 2013; Kang et al., 2014). In a few clusters there is evidence of relativistic electrons from the tail of a radio galaxy being re-accelerated by a passing merger shockwave, as in Abell 3411-3412 (van Weeren et al., 2017), PLCKG287.0+32.9 (Bonafede et al., 2014) and CIZA J2242.8+5301 (Di Gennaro et al., 2018), for example. However a connection between a radio galaxy tail and a relic is not observed in all galaxy clusters hosting a relic, so it is unclear if this can fully solve the problem. Furthermore, re-acceleration does not solve the non-detection of gamma rays at cluster shocks. Unless galaxy jets and lobes are lepton-dominated, protons are also expected to be re-accelerated and therefore produce gamma rays via hadronic collisions (Vazza & Brüggen, 2014).

The advent of low frequency radio observatories has allowed new insights into the mechanisms producing large-scale emission in galaxy clusters and led to the discovery

of new steep-spectrum sources, essentially invisible to even the most sensitive higher frequency observatories (e.g. de Gasperin et al., 2017; Mandal et al., 2020). These fossil plasma sources might be revealing an additional population of seed relativistic electrons that are available to be re-accelerated by either turbulence or a passing shock wave. As more of these sources are detected, and we are better able to understand the prevalence of fossil plasma pools in clusters, their relevance to other cluster radio emission should become more apparent.

Approximately one third of clusters currently known to contain a radio relic host a pair of diametrically-opposed relics, so-called double radio relics (de Gasperin et al., 2014; van Weeren et al., 2019). From simulations such clusters should be undergoing clean binary mergers on, or close to, the plane of the sky (e.g. van Weeren et al., 2011). Such constraints on the viewing angle minimises the influence of projection effects on analysis. The simple merger geometry makes clusters hosting double radio relics ideal for studying not only relativistic particle (re-)acceleration, but also gas and dark matter distributions (e.g. Golovich et al., 2019b).

In this paper we present follow-up radio observations of PSZ2 G096.88+24.18, a low-mass, double radio relic merging galaxy cluster system, with the Karl G. Jansky Very Large Array (VLA), the Low Frequency Array (LOFAR) and X-ray observations with *Chandra*.

2.1.1 PSZ2 G096.88+24.18

PSZ2 G096.88+24.18 (also known as ZwCL1856.8+6616 Zwicky et al., 1961, $z = 0.3$) was detected through the Sunyaev-Zeldovich (SZ) effect by the *Planck* satellite (Planck Collaboration et al., 2011). A total SZ mass of M_{500}[1]$= (4.7 \pm 0.3) \times 10^{14} \mathrm{M}_{\odot}$ was reported in the second *Planck* data release (Planck Collaboration et al., 2016).

de Gasperin et al. (2014) discovered a pair of radio relics on the northern and southern edges of PSZ2 G096.88+24.18 at 1.4 GHz with Westerbork Synthesis Radio Telescope (WSRT). They also reported a low significance detection of a giant radio halo. Recently Finner et al. (2021) investigated the merger scenario of PSZ2 G096.88+24.18 by combining weak gravitational lensing analysis using *Subaru*, archival X-ray *XMM Newton* data and the radio intensity images presented fully in this paper. They found that the radio relics, mass distribution from weak lensing and X-ray morphologies of PSZ2 G096.88+24.18 are all aligned along the same axis. Combined with the spectroscopic results of Golovich et al. (2019a), who found a single-peak redshift distribution of galaxies associated with PSZ2 G096.88+24.18, the merger is likely a head-on collision on the plane of the sky. Finner et al. (2021) also found that the time since collision is $0.7^{+0.3}_{-0.1}$ Gyr and the mass ratio of the merging subclusters is 1:1, with a total mass of M_{200}[1] $= 2.7^{+1.1}_{-1.5} \times 10^{14} \mathrm{M}_{\odot}$. The two mass estimates of PSZ2 G096.88+24.18 do not agree. However, cluster masses derived from the SZ effect are known to be significantly larger than those derived from

[1] $M_{500(200)}$ is the mass enclosed within the radius $r_{500(200)}$, at which the mean density of the cluster is 500(200) times the critical density of the Universe at the cluster redshift.

Table 2.1: Radio Observations

Telescope	Project ID	Frequency [GHz]	Array Mode/Configuration	Observation Date	Integration Time [s]	On-Source Time [hr]	Primary Calibrator
LOFAR	LC9_036	0.120 - 0.187	HBA_DUAL_INNER	2018 Aug 19	1	8	3C295
VLA	15A-056	1 - 2	C	2016 Feb 01	5	3.5	3C286
VLA	15A-056	1 - 2	CnB-B	2015 Feb 05	3	2.5	3C286
VLA	15A-056	1 - 2	CnB-B	2015 Feb 02-03	3	2.5	3C147

weak lensing, primarily due to departures from hydrostatic equilibrium, to which SZ measurements are sensitive (see von der Linden et al., 2014, and references therein).

This paper is organised as follows. In Section 2.2 we detail the LOFAR, VLA and *Chandra* observations and their data products. We present our results for PSZ2 G096.88+24.18 in Section 2.3. The discussion and conclusions of our results are in Sections 2.4 and 2.5. In this paper we assume a flat ΛCDM cosmology, with $H_0 = 70$ km s^{-1} Mpc^{-1} and $\Omega_M = 0.3$. At the redshift of PSZ2 G096.88+24.18 ($z = 0.3$), $1''$ corresponds to a linear scale of 4.45 kpc.

2.2 Observations & data analysis

In this paper we present LOFAR HBA 140 MHz and VLA 1.5 GHz observations of PSZ2 G096.88+24.18. Details of the observations can be found in Table 2.1. Additionally we present *Chandra* X-ray data of PSZ2 G096.88+24.18. In the following sections we summarise the main data calibration and imaging steps.

2.2.1 LOFAR

PSZ2 G096.88+24.18 was observed for 8 hrs on 2018 August 19 with LOFAR High Band Antenna (HBA) stations in HBA_DUAL_INNER mode as part of the project LC9_036. The total 120 – 187 MHz bandwidth was divided into 243 sub-bands. Prior to the target observation the calibrator 3C295 was observed for 10 minutes. Radio Frequency Interference (RFI) was removed using AOFLAGGER (Offringa et al., 2012), as is done for all datasets before being archived. The standard LOFAR processing pipeline PREFACTOR3 (de Gasperin et al., 2019) was used to calculate direction-independent instrumental and ionospheric effects, including the station-based clock offsets, polarisation offsets, bandpass and ionospheric rotation measure. The calibrator flux density scale was set according to Scaife & Heald (2012).

Earth's ionosphere has a greater effect on observations at low radio frequencies. LOFAR therefore requires advanced calibration techniques to adjust for direction-dependent effects caused by the ionosphere and additionally, imperfect beam models. Following the direction-dependent calibration procedure detailed in van Weeren et al. (2016b)[2], the field around the target was split into roughly 60 facets, each containing a bright (> 0.3 Jy)

[2]https://github.com/lofar-astron/factor

calibrator source. Self-calibration was performed on the calibrator source of the target facet, all those surrounding the target facet and any additional facets containing such a source with flux density of ≥1 Jy. The calibration solutions obtained for each calibrator were then applied to the whole facet. After self-calibration we achieve a typical resolution of ∼ 5″, RMS noise of ∼ 0.11 mJy beam^{-1} and dynamic range of ∼ 5000. The absolute flux scale is consistent, within errors, with the LOFAR Data Release 2 images (Shimwell et al., 2022).

2.2.2 VLA

Three L-Band (1-2 GHz) observations of PSZ2 G096.88+24.18 were completed by VLA on separate days as part of project 15A-056, with a total on-source time of 8.5 hours. For each observation the full bandwidth was split into 16 spectral windows, each comprised of 64 channels of width 1 MHz. Details of the observations are given in Table 2.1. All polarisation products were recorded.

The data were calibrated using CASA version 5.3 (McMullin et al., 2007). Prior to calibration the setup scan, shadowed antennas, first and last integrations of each target scan and any zero amplitude data were flagged. The data were Hanning-smoothed and AOFLAGGER was used to remove RFI from observations of the calibrator sources. The data were then calibrated for the gain curve, efficiency, antenna position offsets, global delays, bandpass and local gains using the primary and phase calibrators. The data were calibrated for cross-hand delays and polarisation angle using a calibrator with known polarisation fraction and angle and for instrumental polarisation using a calibrator with no, or very little, polarised emission. A list of the calibrators used for the three can be found in Table 2.4 The flux density was scaled to the primary calibrator models from Perley & Butler (2017) and all calibrator solutions were applied to the target field. RFI in the target observations was removed using AOFLAGGER. After averaging the data to 10 seconds the solutions for the target field were refined with several rounds of phase and amplitude self-calibration. Once calibrated, the individual datasets were combined, resulting in a typical dynamic range of ∼ 900.

Sources outside the VLA primary beam were subtracted from the *uv*-data to avoid contamination through the VLA beam sidelobes. Stokes I, Q, U and V images were obtained with WSCLEAN (Offringa et al., 2014) using various weightings and taperings (see Table 2.2).

2.2.3 Radio data products

All radio continuum images were produced using WSCLEAN, with different weighting schemes to produce images with different resolutions. All images have a central frequency of 140 MHz and 1.5 GHz for LOFAR and VLA respectively. A list of all radio continuum images included in this paper, along with their most important imaging parameters and properties, can be found in Table 2.2. All images were corrected for primary beam

Table 2.2: Radio Image Properties

Telescope	Beam [″×″]	RMS Noise [μJy beam^{-1}]	Weighting	uv-Tapering [″]	Discrete Sources Removed
LOFAR	13×7	127	Briggs, robust = 0	-	No
LOFAR	20×17	179	Briggs, robust = 0.3	-	Yes/No
LOFAR	15×9	135	Briggs, robust = 0.1	-	Yes
LOFAR	27×24	213	Briggs, robust = 0.4	-	Yes
VLA	10×9	8	Briggs, robust = 0	10	No
VLA	25×25	32	Briggs, robust = 0	30	Yes

attenuation.

Radio intensity images of PSZ2 G096.88+24.18 from both LOFAR and VLA are shown in Fig. 2.1.

The error in measured flux density is calculated using

$$\sigma_S = \sqrt{\left(\sigma_{\rm rms}\sqrt{n_{\rm beams}}\right)^2 + \left(\sigma_{\rm cal}\right)^2}, \tag{2.1}$$

where $\sigma_{\rm rms}$ is the RMS noise, $n_{\rm beams}$ the number of beams within the region of interest and $\sigma_{\rm cal}$ the flux error from calibration. We assumed a 15% flux calibration error for LOFAR (Shimwell et al., 2016) and 5% for VLA (Perley & Butler, 2017).

To remove the contribution of discrete sources embedded within the diffuse emission we subtracted them from the uv-data. To achieve this the data were imaged at high resolution, with an inner uv-cut of 5.15 kλ. At z = 0.3 this corresponds to excluding scales above a linear size of 178 kpc. The uv-cut was chosen to exclude most of the diffuse cluster emission. PYBDSF (Mohan & Rafferty, 2015) was used to detect 5σ point sources in the image and the results were checked by eye. We ignored detections within the radio relics as they likely correspond to the brightest regions of diffuse emission, while the rest of the relic is mostly resolved out in the high resolution image. All remaining point sources were subtracted from the uv-data using the clean components created by WSCLEAN.

2.2.3.1 Spectral index

To account for the different uv-coverages of LOFAR and VLA we imaged both datasets, with discrete sources subtracted, within the same uv-range and tapered to approximately the same beam size, using Briggs weighting, robust=-0.5 (Briggs, 1995). The images were subsequently convolved to the same beam (medium resolution: 10″×10″, low resolution: 25″×25″).

To produce maps of the spectral index across PSZ2 G096.88+24.18 we computed the spectral index α_{1500}^{140} for each pixel, excluding any pixels with a flux density $< 3\sigma_{\rm rms}$ in

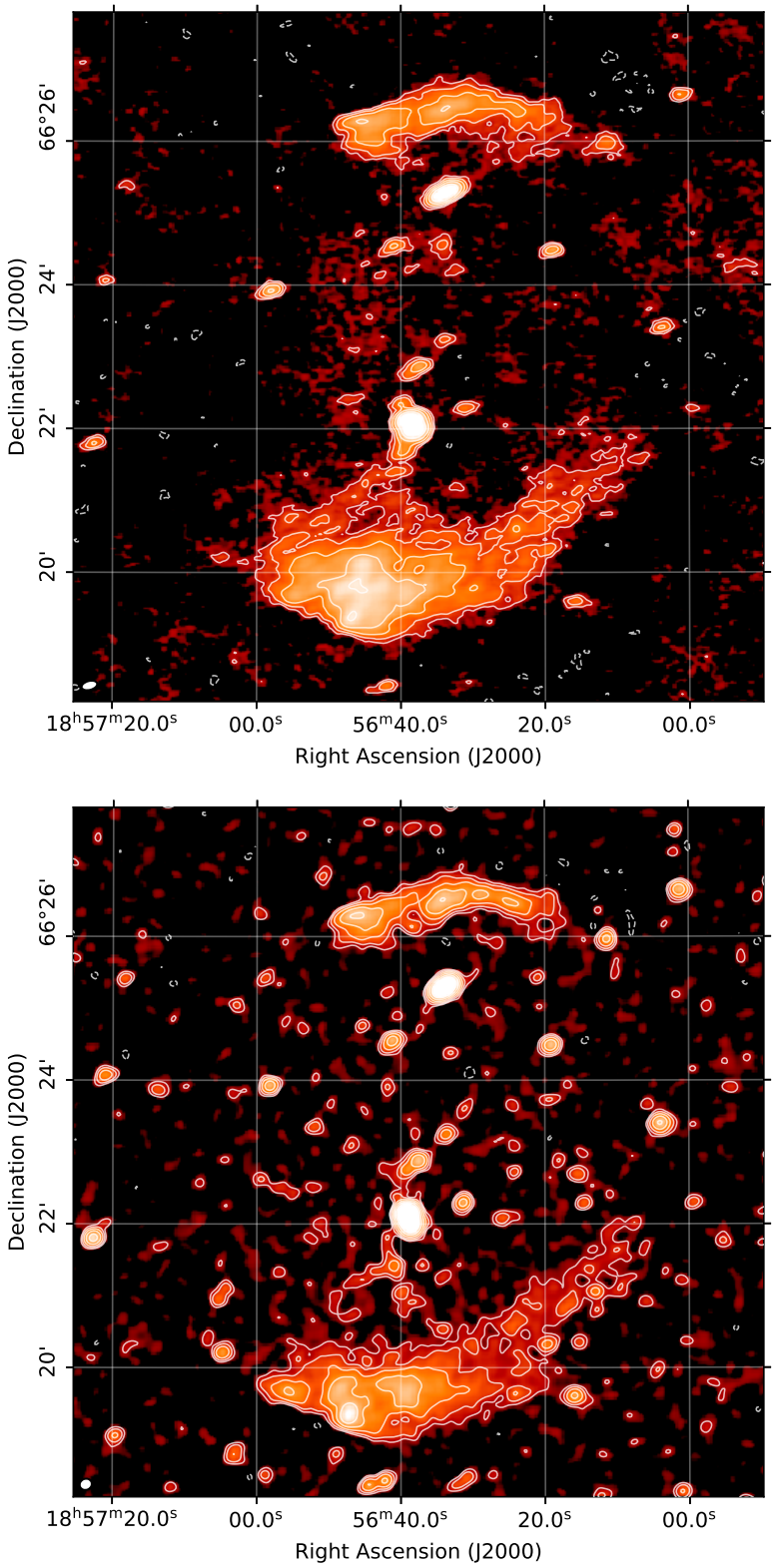

Figure 2.1: Radio intensity images of PSZ2 G096.88+24.18. Left: LOFAR 140 MHz (resolution: 13″×7″, RMS noise: 127 μJy beam^{-1}. Right: VLA 1.5 GHz (resolution: 10″×9″, RMS noise: 8 μJy beam^{-1}). Contour levels for both images are set at $3\sigma_{\rm rms}\times$ [1,2,4...]. Dashed contours at $-3\sigma_{\rm rms}$. Beam shapes are drawn in the bottom left corner of each image.

either image. Throughout the paper we calculate the spectral index error as

$$\sigma_\alpha = \frac{1}{\ln \frac{\nu_1}{\nu_2}} \sqrt{\left(\frac{\sigma_{S,1}}{S_1}\right)^2 + \left(\frac{\sigma_{S,2}}{S_2}\right)^2}, \tag{2.2}$$

where ν_1 and ν_2 are the characteristic frequencies of the images, S_1 and S_2 are the flux densities and $\sigma_{S,1}$ and $\sigma_{S,2}$ the respective flux density errors calculated from Equation 2.1. The spectral index maps produced are shown in Fig. 2.2.

2.2.3.2 Polarisation

All four correlation products were recorded by VLA, so we were able to calculate all Stokes parameters I,Q,U and V. Assuming negligible circular polarisation, fractional polarisation is given by

$$P_{\rm frac} = \frac{S_{\rm Pol}}{S_I}, \tag{2.3}$$

where S_I is the total intensity and $S_{\rm Pol}$ the true polarised intensity. At low signal-to-noise the noise can bias the measured polarisation intensity to higher values (Rice, 1945; Simmons & Stewart, 1985). To account for this we calculate the true polarisation intensity from the measured intensity using the results of Wardle & Kronberg (1974):

$$S_{\rm Pol} \sim S'_{\rm Pol} \sqrt{1 - \left(\frac{\sigma'_{\rm Pol}}{S'_{\rm Pol}}\right)^2}, \tag{2.4}$$

where $\sigma'_{\rm Pol}$ is the measured RMS noise in polarisation intensity and $S'_{\rm Pol}$ the measured polarisation intensity, which is calculated from the measured linear polarisation intensities S_Q and S_U (Stokes parameters Q and U) using

$$S'_{\rm Pol} = \sqrt{(S_Q)^2 + (S_U)^2}. \tag{2.5}$$

The polarisation angle is then calculated using

$$\Psi_{\rm pol} = \frac{1}{2} \arctan\left(\frac{S_U}{S_Q}\right). \tag{2.6}$$

Ionised material, in the presence of a magnetic field, along the line of sight between the observer and the target will rotate the intrinsic polarisation angle by an amount

$$\Delta\Psi = \lambda^2 {\rm RM}, \tag{2.7}$$

where λ is the observation wavelength and RM is the rotation measure. From the map of galactic Faraday rotation presented in Oppermann et al. (2015), we find that our Galaxy accounts for an RM = -4.5 rad m^{-2} in the direction of PSZ2 G096.88+24.18,

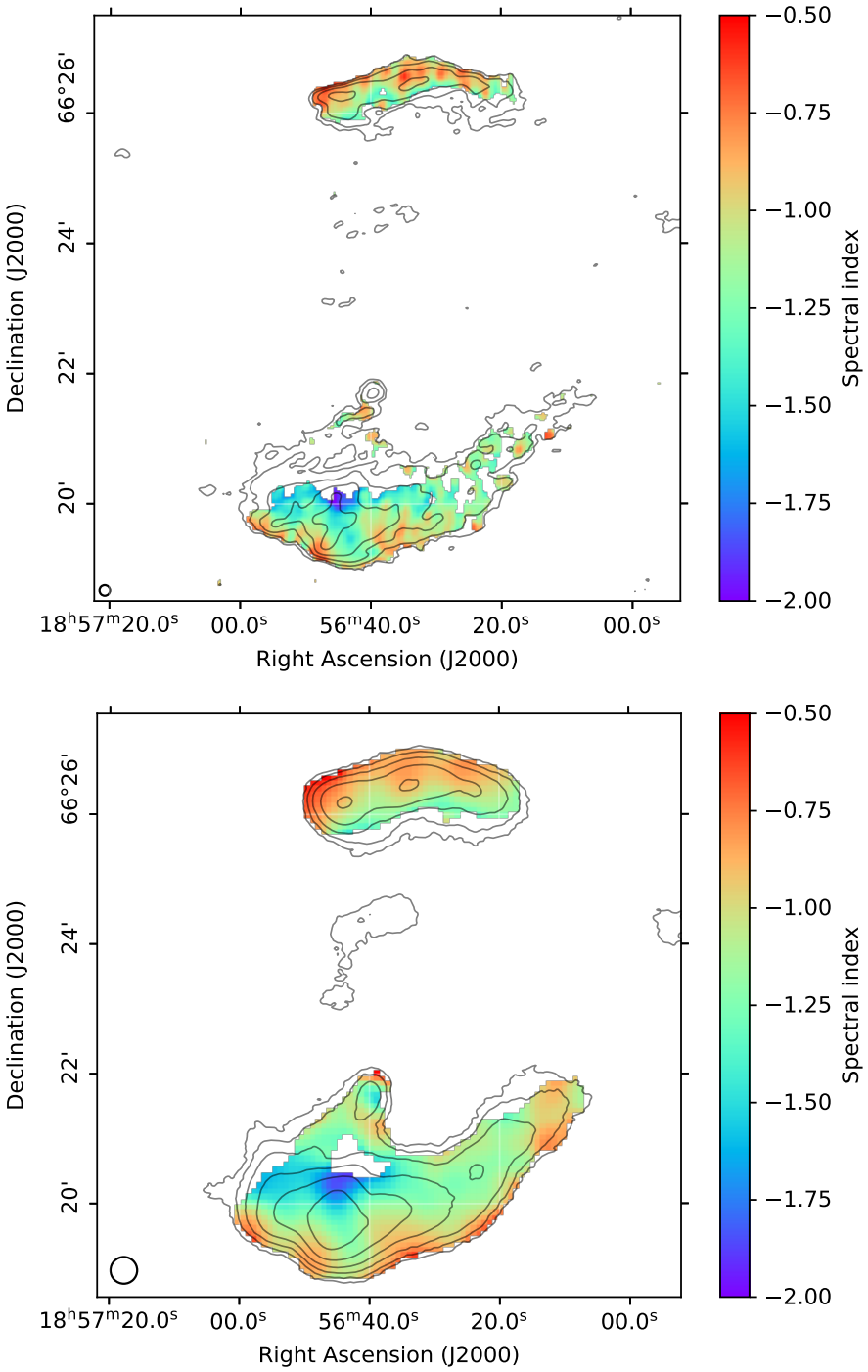

Figure 2.2: Spectral index maps created between 140 MHz and 1.5 GHz. Top: High resolution (10″×10″). Bottom: Low resolution (25″×25″). Corresponding error maps are shown in Fig. 2.9.

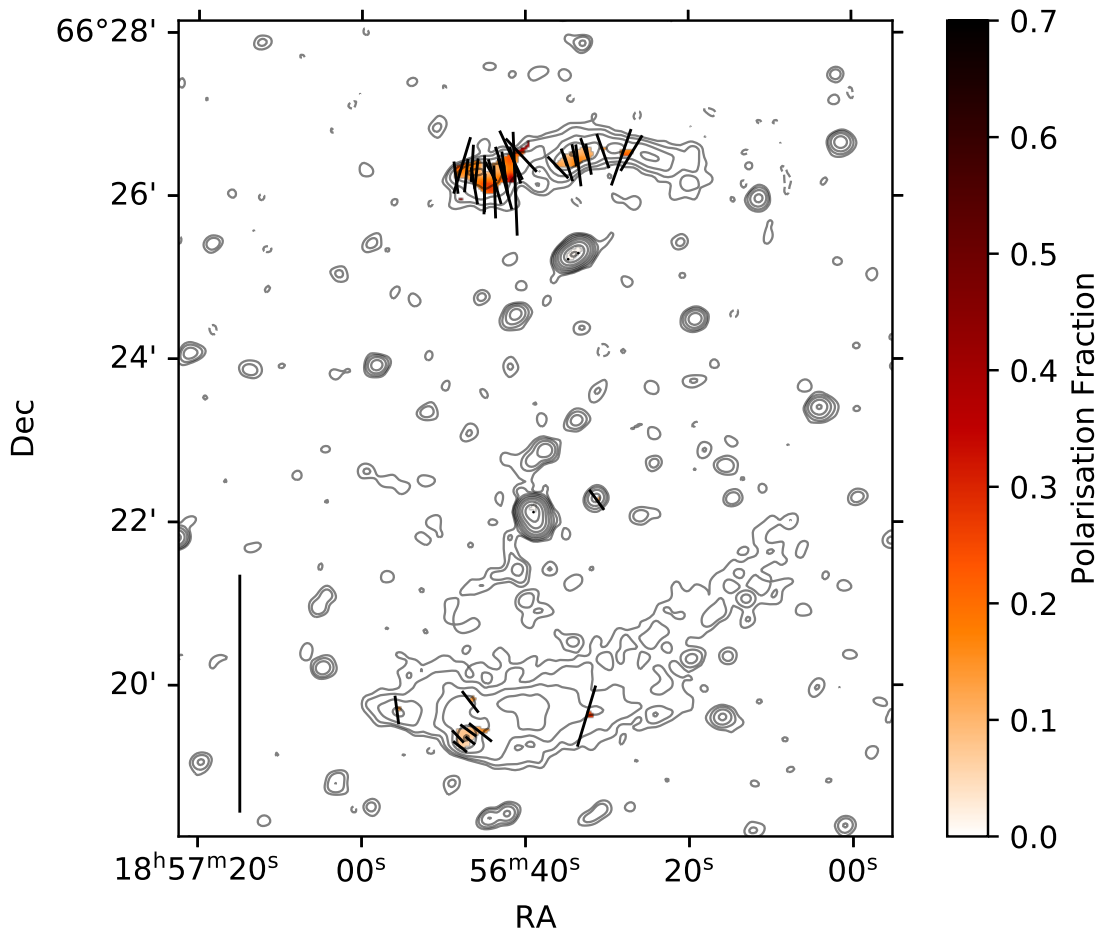

Figure 2.3: Linear polarisation fraction image. E-field vectors are plotted in black, with amplitude proportional to the polarisation fraction. A reference vector, corresponding to 100% polarisation fraction, is plotted in the bottom left. Contours as in Fig. 2.1 (right).

corresponding to a rotation of the polarisation angle $\Delta\Psi = -10°$ at 1.5 GHz. We therefore rotate all polarisation vectors by this amount, to show only the intrinsic polarisation angle.

Fig. 2.3 shows the polarisation vectors, corresponding to the electric field vectors, overlaid on an image of the fractional polarisation measured at 1.5 GHz by VLA.

2.2.4 Chandra

On 2018 June 03 *Chandra* ACIS-I detector observed PSZ2 G096.88+24.18 for 43 ks (ObsID 19752). The data were calibrated with CIAO version 4.12 (Fruscione et al., 2006) using CALDB version 4.9.1. The event files were reprocessed using CHANDRA_REPRO to create new level 2 data products. The data were filtered to 0.5 – 7 keV to exclude contamination at low energies and the high energy particle background. Periods with anomalously low count rates and flares were found and removed using LC_CLEAN. 42ks remained after filtering. Blank sky event files were used to model the instrumental

Table 2.3: Radio Diffuse Emission Properties

Source	$S_{140\,\mathrm{MHz}}$ [mJy]	$S_{1.5\,\mathrm{GHz}}$ [mJy]	α_{int}	α_{inj}	$\mathcal{M}_{\mathrm{int}}$	$\mathcal{M}_{\mathrm{inj}}$
N Relic	76 ± 12	7.8 ± 0.4	-0.95 ± 0.07	-0.87 ± 0.07	-	2.5 ± 0.2
S Relic	276 ± 42	16.5 ± 0.9	-1.17 ± 0.07	-0.97 ± 0.07	3.6 ± 0.7	2.3 ± 0.2
S Relic E	234 ± 35	13.5 ± 0.7	-1.19 ± 0.07	-0.96 ± 0.07	3.4 ± 0.6	2.3 ± 0.2
S Relic W	38 ± 6	2.8 ± 0.2	-1.08 ± 0.07	-1.01 ± 0.09	5.1 ± 2.2	2.2 ± 0.2
Connection	14 ± 2	0.7 ± 0.1	-1.22 ± 0.08	-	-	-

background on the observation date. Point sources were detected using WAVDETECT with wavelet scales of 1, 2, 4, 8 and 16 pixels, visually inspected and excluded for analysis. The $1-4$ keV *Chandra* exposure-corrected flux image is shown in Fig. 2.4, with radio and weak lensing mass distribution contours overlaid.

2.3 Results

2.3.1 Radio relics

Fig. 2.5 shows LOFAR radio contours overlaid on an r-band Subaru image. Regions of particular relevance to this paper are labelled and spectroscopically-confirmed cluster-member galaxies are highlighted (Golovich et al., 2019a). The image shows the presence of two arc-like structures on opposite sides of the cluster (N and S relics). The morphology, location at the cluster periphery and spectral index variation (Fig. 2.2) of the arc-like radio structures in PSZ2 G096.88+24.18, a merging galaxy cluster, all strongly suggest that we are observing a pair of radio relics. If we define the cluster centre as the peak of X-ray emission the outer edges (shock fronts) of the northern and southern relics lie at a distance of ~ 560 kpc and 1.3 Mpc respectively. However PSZ2 G096.88+24.18 is a galaxy cluster comprised of two merging subclusters separated by ~ 600kpc (Finner et al., 2021). The X-ray peak is therefore located at the centre of the brightest subcluster. If instead we take the cluster centre to be at the midpoint between the two mass peaks (cyan cross in Fig. 2.4), the shock fronts of the northern and southern relics lie at a distance of ~ 1.1 and 1.0 Mpc from the cluster centre. We choose the latter as our definition of the cluster centre.

At 140 MHz the radio relics have largest linear sizes (LLS) of ~ 0.9 and 1.5 Mpc and a flux ratio of 1:3.5 for the north and south relics respectively. Both radio relics have a non-uniform brightness along their major axes (Fig. 2.1). The average surface brightness is approximately 4 times greater in the eastern side of the southern relic compared to the west. Higher resolution images (Fig. 2.1) of PSZ2 G096.88+24.18 show filament-like substructures in the northern relic.

The flux densities, spectral indices and Mach numbers of all regions of diffuse emission are listed in Table 2.3. Fig. 2.6 shows the regions used to calculate the flux densities, overlaid on a low resolution ($17'' \times 17''$) VLA image.

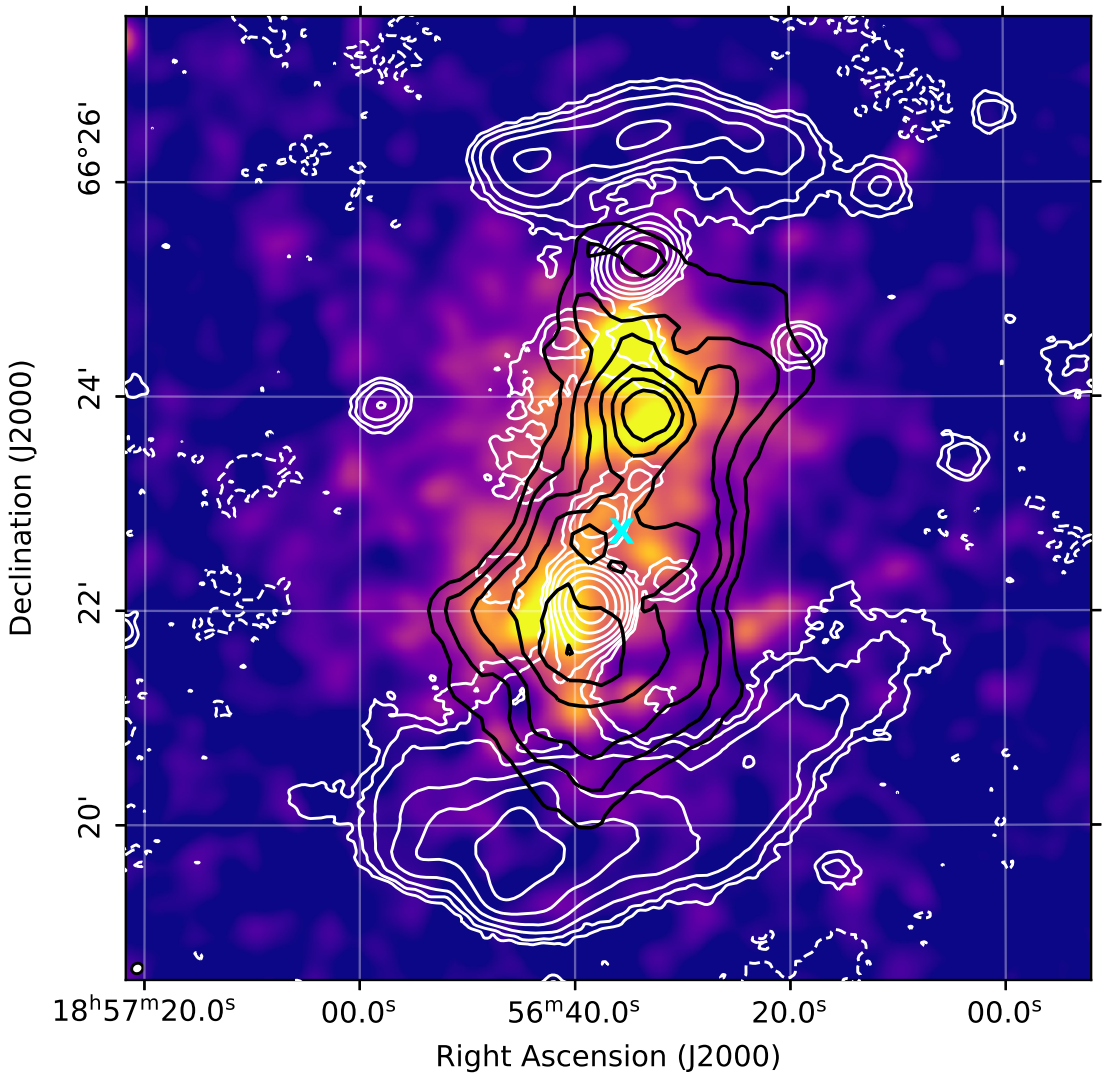

Figure 2.4: Exposure-corrected Chandra X-ray 1.0−4.0 keV image. The image is smoothed with a gaussian kernel of width $\sigma = 7''$. Black contours show the mass distribution from Finner et al. (2021). Levels at: $\sigma_{\rm mass}\times$ [2.1,2.4,2.7,3.1,3.4]. White contours from the LOFAR 140 MHz image (resolution: $20''\times17''$, RMS noise: 179 μJy beam^{-1}). Contour levels at $3\sigma_{\rm rms}\times$ [1,2,4...]. Dashed contours at $-3\sigma_{\rm rms}$. The cyan cross denotes the cluster centre used in this work.

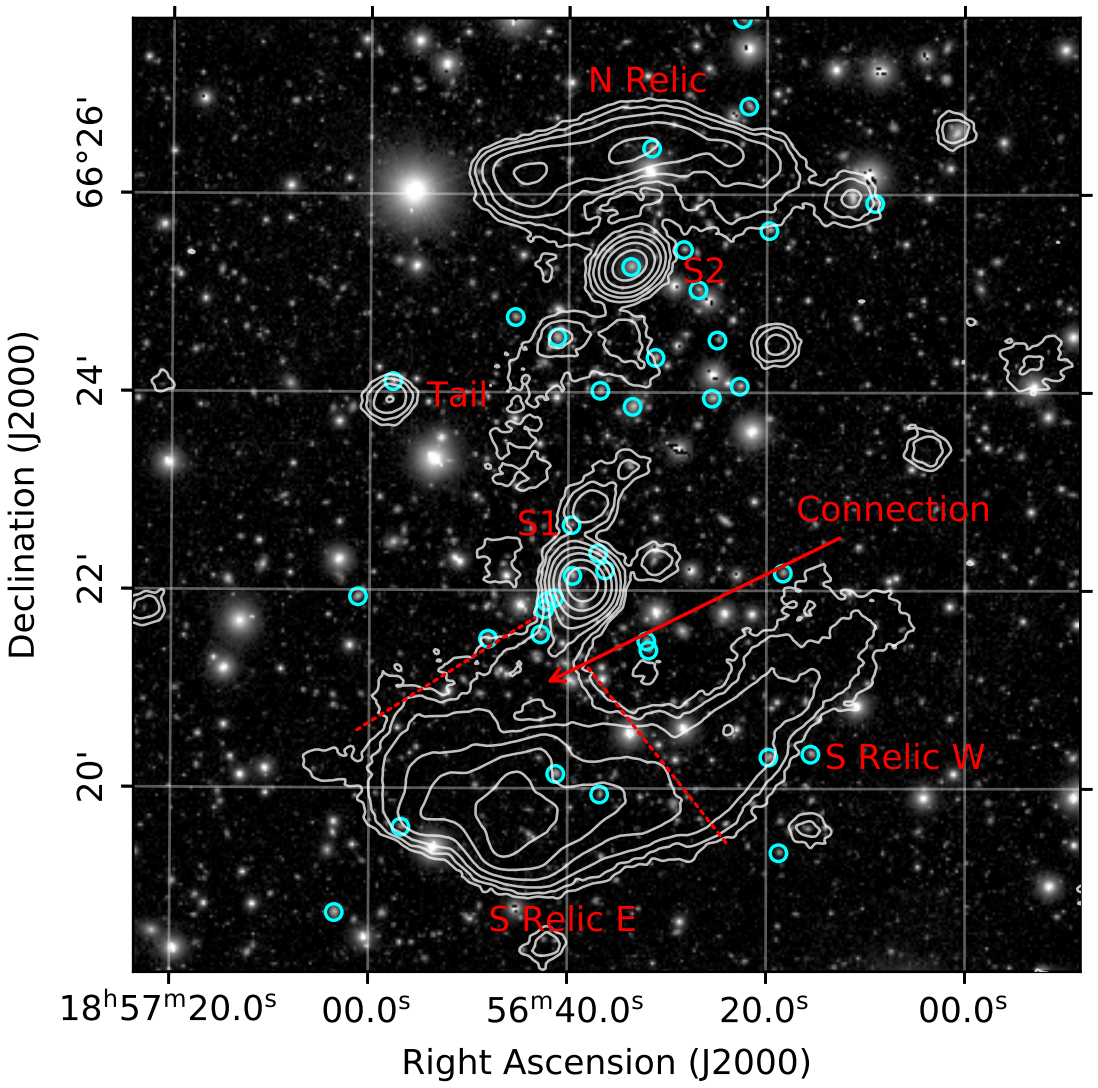

Figure 2.5: Subaru Suprime r-band image from Finner et al. (2021). Overlaid LOFAR contours as in Fig. 2.4. Radio sources of particular relevance to this paper are labelled. Dashed lines are drawn to follow the Connection contours, extrapolated to the radio relic edge. Cyan circles show the spectroscopically-confirmed cluster members.

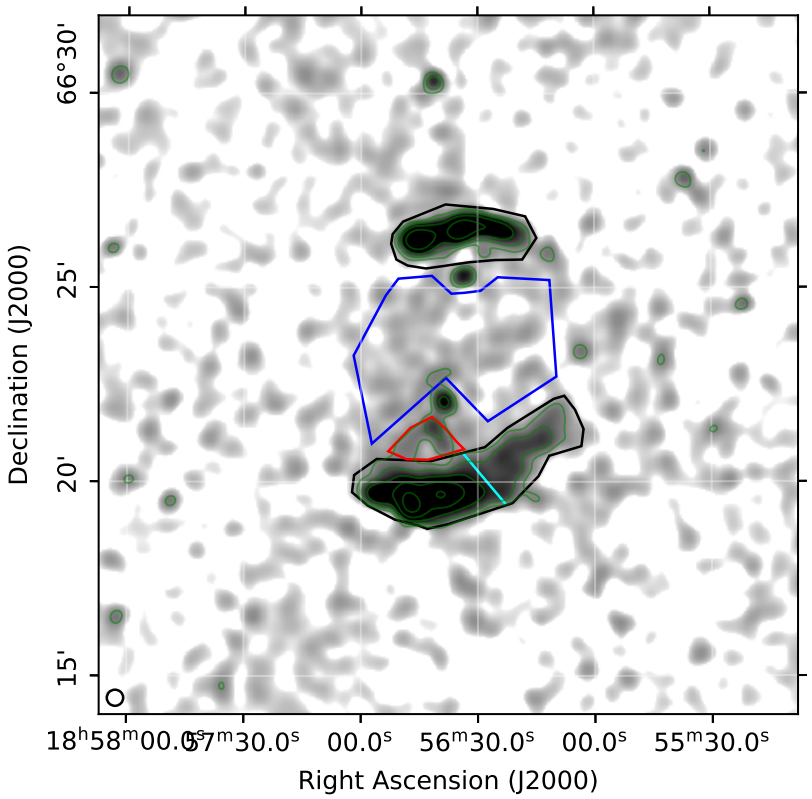

Figure 2.6: VLA intensity image (resolution: 25″×25″, RMS noise: 32 μJy beam^{-1}). Contour levels at $3\sigma_{\rm rms}\times$ [1,2,4...]. Dashed contours at $-3\sigma_{\rm rms}$. Regions of extraction for the flux density measurements in Table 2.3 in black (radio relics), red (Connection), cyan (line dividing east and west sides of the southern radio relic) and for the candidate radio halo in blue (see Section 2.4.3).

Fig. 2.2 shows the spectral index maps at medium (10″) and low resolution (25″). Both the north and south relics exhibit spectral steepening from the shock edge towards the cluster centre, from about $\alpha = -0.6$ to $\alpha = -2.0$ in the case of the southern relic and $\alpha = -0.5$ to $\alpha = -1.5$ for the northern relic. A spectral steepening towards the cluster centre is expected from downstream synchrotron and Inverse Compton (IC) losses, as observed in many other clusters (e.g. Bonafede et al., 2012; van Weeren et al., 2016a; Hoang et al., 2017; Di Gennaro et al., 2018). Whilst the radio relics show a general steepening of the spectral index towards the cluster centre, the distribution in the southern relic is non-uniform. There are regions up to ~ 40 ″ (170 kpc) downstream of the shock front with relatively flat ($\alpha > -1$) spectral indices (red in Fig. 2.2), as well as regions at the relic edge with relatively steep spectral index ($\alpha \sim -1.1$, green in Fig. 2.2).

In Fig. 2.8 we plot the integrated spectral index as a function of distance from the shock front in three different regions of the radio relics (blue, red and yellow). The short side of each region is one restoring beam width and the regions were oriented to follow the direction perpendicular to the shock front, moving downstream of both relics. Using the blue and red sets of regions we are able to compare the spectral behaviour of the east and west sides of the southern relic. In all three sets of regions (blue, red and yellow) the spectrum steepens towards the cluster centre. Up to the southern edge of the Connection (see Section 2.3.3), the east and west sides of the southern relic show similar steepening as a function of distance from the shock front.

Fig. 2.3 shows the linear polarisation fraction image of PSZ2 G096.88+24.18 at 1.5 GHz, with electric field vectors overlaid. In the northern radio relic there are significant regions of polarised emission, mostly corresponding to the brightest parts of the relic. The linear polarisation fraction ranges from $\sim$ 10% - 60%. The polarisation vectors, chosen here to show the electric field direction, are all approximately perpendicular to the shock front. This implies that the magnetic field is ordered and compressed along the shock front, as a consequence of shock passage (Enßlin et al., 1998). The southern relic has polarised emission in only a few small regions and the polarisation fraction is much lower than in the northern relic, reaching a maximum of 20%. In these small regions the electric field vectors do not lie perpendicular to the shock. These findings are in line with those of de Gasperin et al. (2014), although obtained with a different dataset.

2.3.2 Shock Mach numbers

The strength of the shock, or Mach number $\mathcal{M}$, affects the other observed properties of a shock front. DSA predicts that the slope of the spectral energy distribution at the shock front, $\alpha_{\rm inj}$, depends on the Mach number (Blandford & Eichler, 1987), with

$$\alpha_{\rm inj} = \frac{1}{2} - \frac{\mathcal{M}^2 + 1}{\mathcal{M}^2 - 1}. \tag{2.8}$$

If the injection spectral index can be measured accurately, this should provide the most reliable Mach number estimate (assuming DSA), as we expect the merger axis to be on

the plane of the sky and therefore projection effects should be minimised. We do not have the frequency coverage to calculate α_{inj} by spectral ageing (e.g. Harwood et al., 2013; de Gasperin et al., 2015). We instead choose to calculate the average spectral index along the shock front, using a region covering the entire shock front with a width of one beam.

An alternative method of estimating the Mach number of a shock is to use the integrated spectral index, $\alpha_{\rm int}$, as it reduces statistical uncertainties. By considering the shock as a simple planar shock, we can relate the integrated and injection spectral indices through

$$\alpha_{\rm inj} = \alpha_{\rm int} + \frac{1}{2}. \tag{2.9}$$

(Kardashev, 1962). However, such an approximation is likely not valid for spherically-expanding shocks (Kang, 2015) or within a turbulent medium (Domínguez-Fernández et al., 2021). We present Mach numbers calculated by both methods in this paper in Table 2.3. It is also possible to independently measure the shock Mach number from X-ray surface brightness and/or temperature discontinuities. However, our *Chandra* data is too shallow to detect any discontinuity and we are therefore unable to calculate Mach numbers in this way.

2.3.3 Radio relic connection

Between the southern radio relic and S1 there is a continuous patch of diffuse radio emission (Connection), clearly seen in the lower-frequency, LOFAR images (Fig. 2.5). Due to its relatively steep spectrum and low surface brightness, the Connection is only visible in low resolution VLA images (Fig. 2.6). There is a section of the Connection closest to the relic that is only visible in the LOFAR images. Fig. 2.7 shows the variation of the average surface brightness along the shock front of the southern relic. The eastern side of the relic has an average flux density approximately 4 times greater than the western side and all individual regions have a greater average surface brightness than any on the western side. This surface brightness jump aligns perfectly with the Connection (Fig. 2.5).

As there is a gap in Connection emission in the VLA images, the Connection is only visible in the low resolution spectral index map (Fig. 2.2, bottom panel) as two distinct bands of emission connecting S1 to the radio relic. The spectral index steepens along the eastern band, away from S1, from approximately $\alpha = -1.0$ to $\alpha = -1.3$. However, the western band varies between $\alpha = -0.8$ and $\alpha = -1.3$ with no clear spatial trend. The integrated spectral index along the Connection (Fig. 2.8, red line) flattens from $\alpha = -1.6$ in region 5,$\sim$ 380 kpc from the shock front, to $\alpha = -1.0$ in region 8, $\sim$ 620 kpc from the shock front.

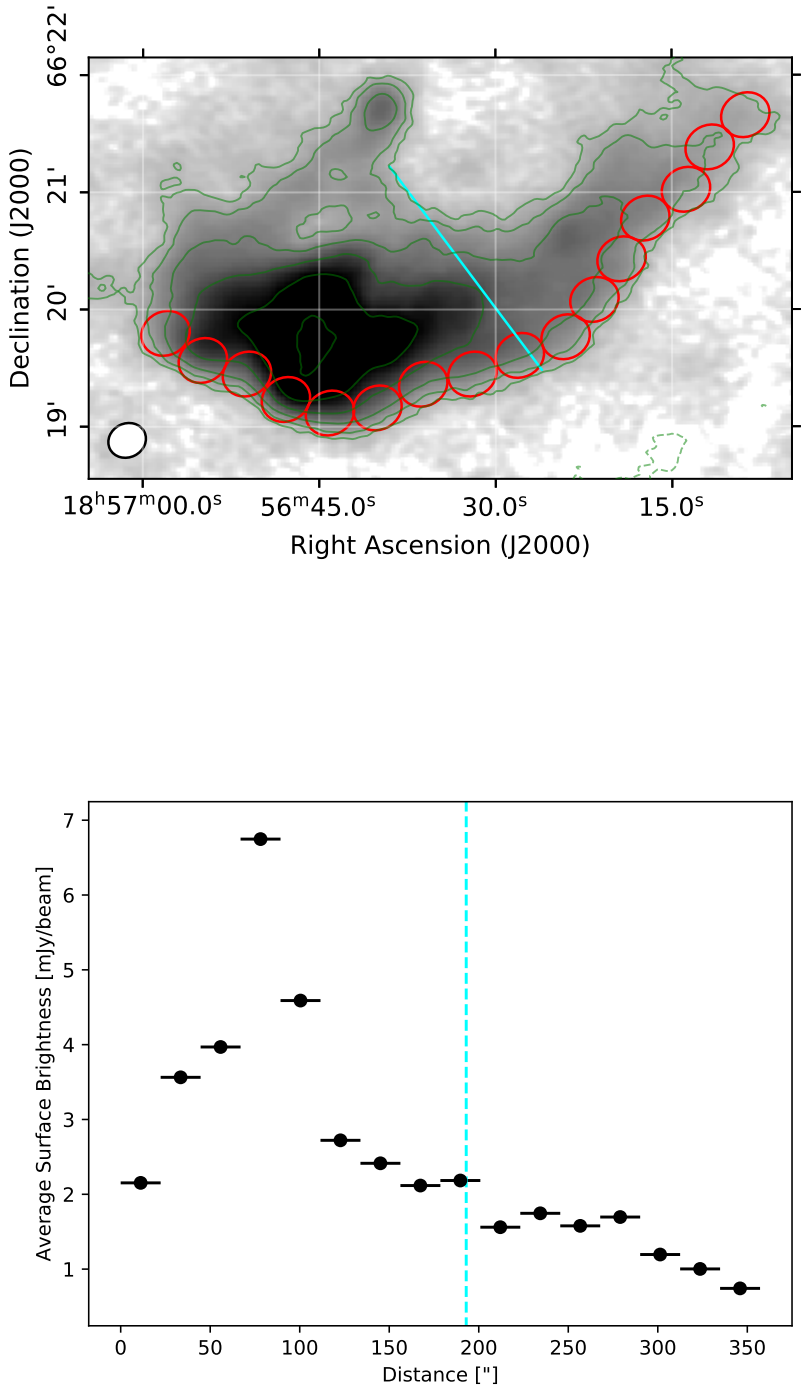

Figure 2.7: Top: Regions in which we calculate the average surface brightness across the southern relic. Each region is the size of the synthesised beam. Bottom: The resulting surface brightness profile as a function of distance from the east edge of the shock front, along the axis of the shock front. The cyan line in both images shows the dividing line between the east and west sides of the relic, as in Fig. 2.5.

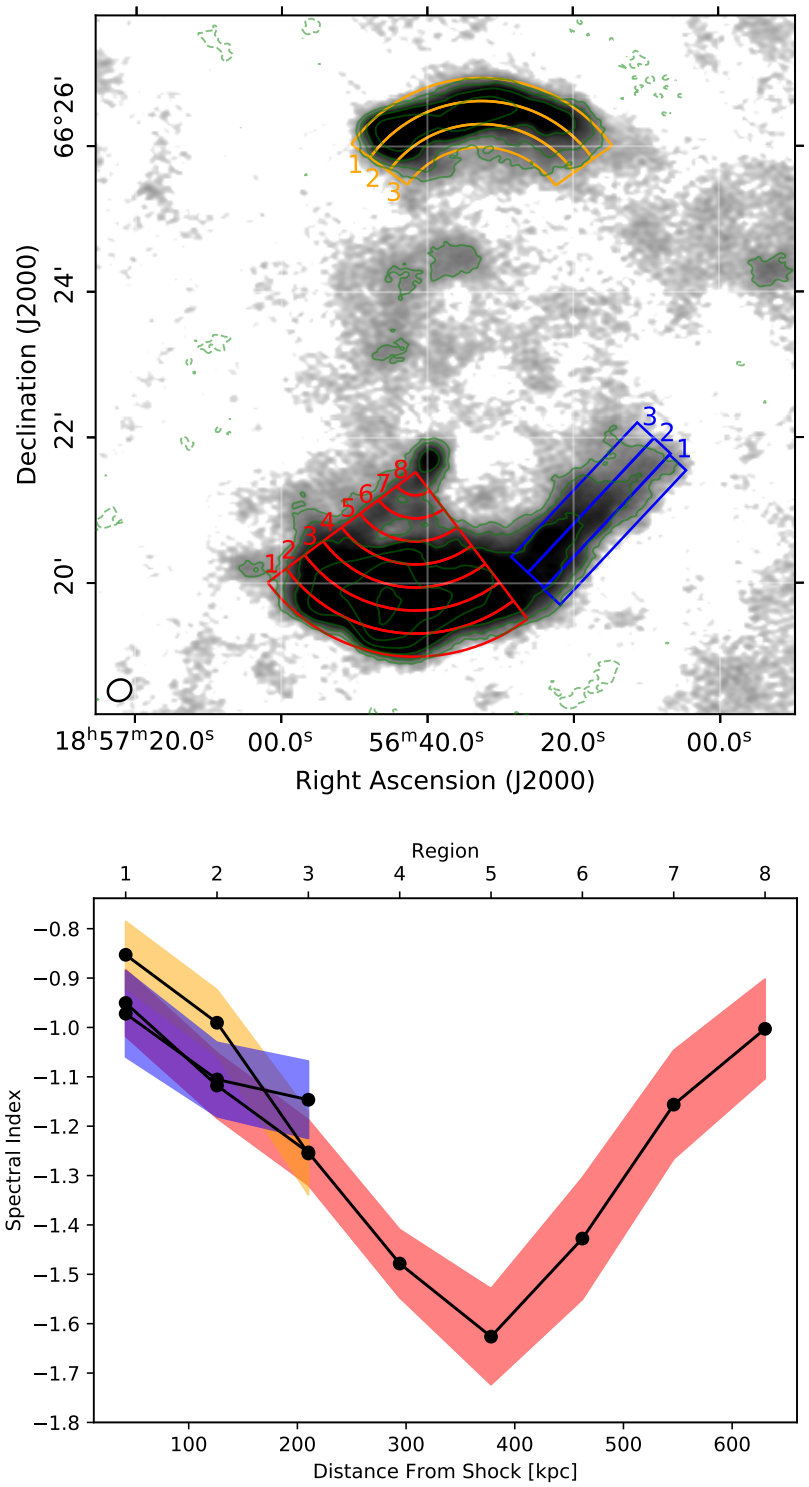

Figure 2.8: Top: Regions where we extract the integrated spectral index. The short sides are exactly one beam width in length (19″). Bottom: The integrated spectral indices extracted from these regions as a function of distance from the shock front.

2.4 Discussion

2.4.1 Radio relics

We are unable to detect evidence of a shock front at the position of either radio relic in the X-ray data. Due to the low count statistics in cluster outskirts, the *Chandra* data are likely not sensitive enough to detect a shock. Finner et al. (2021) also did not detect a shock with a 12 ks *XMM-Newton* observation. The low electron density at the outskirts of galaxy clusters, where radio relics are typically located, makes detection of shocks with X-ray observations challenging. To date, a spatially-coincident X-ray shock has been discovered for only 20 relics (van Weeren et al., 2019). Nonetheless, the relic-shock connection is well-established (see Brunetti & Jones, 2014; van Weeren et al., 2019, for reviews). In the specific case of PSZ2 G096.88+24.18, we expect the radio relics to be associated with merger shocks for a number of reasons, despite the non-detection in X-rays. From the spectral index distribution (Figs 2.2 and 2.8), we see that the spectral index is flattest at the outer edges of both relics, furthest from the cluster centre and that the spectral index subsequently steepens towards the cluster centre. This spectral behaviour is exactly as expected for shock acceleration. The shock front, i.e. the shock edge furthest from the cluster centre, is the site of cosmic ray electron (re-)acceleration. After shock passage, cosmic ray electrons radiate energy away in the form of Inverse-Compton and synchrotron emission. In the absence of another acceleration mechanism, the spectral index of the region downstream of the shock front should therefore be steeper, due to these energy losses. The arc-like morphology of the radio relics in PSZ2 G096.88+24.18 is similar to relics found in other clusters (van Weeren et al., 2019) and to those found in simulations of merger shockwaves (e.g. Skillman et al., 2011; Nuza et al., 2017; Wittor et al., 2017). The longest linear sizes and fluxes of the relics (see Sec. 2.3.1) are in line with the radio relic scaling relations of de Gasperin et al. (2014), though it should be noted that the relics in PSZ2 G096.88+24.18 were included in the sample used to create the scaling relations. Additionally, the location of the relics ($\gtrsim$ 1 Mpc from the cluster centre; see Sec 2.3.1) is in line with the results of Vazza et al. (2012) that, due to the higher kinetic energy dissipated, relics should be preferentially located in cluster outskirts. This also matches with observational findings. Shock waves compress and align the magnetic field along the shock, resulting in high polarisation fractions and electric field vectors that lie perpendicular to the shock front (Brunetti & Jones, 2014). The polarisation properties of the northern relic follow these expectations, but those of the southern relic do not (Fig 2.3). Cluster mergers are expected to launch a pair of shocks in opposite directions along the merger axis. However, favourable viewing conditions, with a merger axis on or almost on the plane of the sky, are required for both shocks to be observable in radio observations (van Weeren et al., 2011). From spectroscopic observations of PSZ2 G096.88+24.18, the merger is expected to be on the plane of the sky and we may therefore expect PSZ2 G096.88+24.18 to host two relics (Golovich et al., 2019a). Additionally, weak lensing analysis of PSZ2 G096.88+24.18reveals that the merger axis lies along the line between the north and south radio relics (Finner et al., 2021). Given these pieces of evidence, we expect that the relics in PSZ2 G096.88+24.18 trace shock waves launched into the ICM by a merger.

The shock wave should compress the magnetic fields within the cluster and align them approximately parallel to the shock front (van Weeren et al., 2010; Brunetti & Jones, 2014, and references therein). This implies that the electric field vectors should lie perpendicular to the shock front and that a significant fraction of the detected radio emission should be polarised. Radio relics typically have polarisation fractions $\geq 10\%$ at GHz frequencies (see Wittor et al., 2019, and references therein) but there are cases where the polarisation fraction can reach up to 70% (e.g. Loi et al., 2017). We observe strongly polarised emission in the northern relic (Fig. 2.3), with all electric field vectors lying approximately perpendicular to the shock front, as expected. Conversely the southern relic shows very little polarised emission. The few polarised regions in the southern relic have very low polarisation fractions ($\leq 10\%$) and show an offset between the electric field vectors and the normal to the shock front. de Gasperin et al. (2014) suggested that this could be caused by the southern relic lying further away from us. In this scenario the radio emission we observe would have to pass through more magnetised, ionised plasma and therefore be subject to more Faraday rotation. However, spectroscopic observations of PSZ2 G096.88+24.18 show that the redshift distributions of the member galaxies are well fit by a single Gaussian (Golovich et al., 2019a). This makes it unlikely that significant additional Faraday rotation due to projection effects is causing the observed difference in polarisation angle.

An alternate reason for the lack of polarised emission in the southern relic could be that turbulence in the relic has mixed the magnetic field lines. Turbulence mixes field lines at scales larger than the Alfvén scale (l_A), i.e. the scale at which the velocity of turbulence is equal to the Alfvén speed (Brunetti & Lazarian, 2016). If this scale is smaller than the beam size, then we would observe no polarised emission. Simulations of cluster mergers show that merger shocks can generate turbulence, with $\leq 10\%$ of the total kinetic energy flux dissipated into the generation of turbulence (e.g. Vazza et al., 2017). The plasma that was (re-)accelerated by the merger shock which created the southern relic could instead have already been turbulent and the shock compression was insufficient to significantly alter its properties. The presence of turbulent motions within the relic may also help explain the irregular spectral values along the relic extension, with the presence of both steep ($\alpha \sim -1.2$) spectral indices close to the shock front and relatively flat ($\alpha \geq -1.0$) spectral index regions downstream (Fig. 2.2).

We can use the polarisation properties of the southern relic to constrain the turbulence within it, assuming the turbulence is generated by the merger shock. The fraction of kinetic energy flux converted to turbulent energy, η, is given by $\frac{1}{2}\eta\rho_u v_s^3 \sim \rho_d \delta v_0^2 v_d$, where ρ_u and ρ_d are the upstream and downstream ICM densities respectively, v_s and v_d the shock and downstream velocities and δv_0 the turbulent velocity at the injection scale. Turbulence needs time to decay from its injection scale, L_0, to l_A before polarisation is removed. Since no polarisation is observed, even close to the shock edge, the decay time ($L_0/\delta v_0$) must be smaller than the time required to travel downstream by a distance of a few beams, (b/v_d), where b represents a few beams. Assuming that the brightness substructures within the relic trace fluctuations in the shock structure caused by the turbulence and that the injection scale is approximately half of these fluctuations, we get that $L_0 \sim 100$ kpc. An injection scale of 100 - 400 kpc is typical for the ICM (Brunetti & Jones, 2014). Given that the beam size is $\sim$ 50kpc and the Mach number $\mathcal{M} = 2.3$, we estimate that the efficiency of

dissipating shock kinetic energy into turbulent energy exceeds 4% at scales below 100 kpc. The stark differences between the north and south relics may be explained if the turbulence in the north relic is generated with lower efficiency, or at larger scales, than in the south relic. The differences may instead suggest that the Connection has played a role in the presence of turbulence in the downstream region of the southern relic (see Section 2.4.2). This could also explain the irregular spectral index distribution in the southern relic (Fig. 2.2).

Some radio relics have been observed with such low polarisation fraction. Bonafede et al. (2009a) reported a mean polarisation fraction of 8% at 1.365 GHz in MACS J0717.5+3745, with regions of strong depolarisation. The polarisation structure of the western relic in Abell 3376 (Kale et al., 2012) shows a striking similarity to that of the southern relic in PSZ2 G096.88+24.18. Kale et al. (2012) reported patchy polarised emission, with electric field vectors not aligned normal to the shock front and suggested that this could be due to turbulence in the backflow of the shock.

The localised nature of the polarised emission and unexpected electric field vector orientation could instead indicate that we are observing emission from a polarised radio galaxy in projection within the relic. However, the area of polarised emission coincides with the brightest part of the radio relic, making it almost impossible to determine from the radio observations if there is indeed a radio galaxy producing the polarised emission we observe. We do not observe any likely optical counterparts in the Subaru image. From examination of the polarisation image, we find that there is low polarisation fraction (<10%) across the entire relic, but below 3 σ. The localised emission seen in Fig. 2.3 is therefore likely a consequence of lying at the brightest part of the relic.

The low signal to noise of the western side of the radio relic does not allow us to analyse the differences in polarisation structure between the two sides of the relic. Due to the complex nature of the southern relic (see Section 2.3.3) it is difficult to draw any firm conclusions from the unusual polarisation structure.

2.4.2 Southern radio relic connection

Radio relics have previously been found with non-uniform brightness. For example, in the Toothbrush (Rajpurohit et al., 2018) and Sausage (Di Gennaro et al., 2018) galaxy clusters, the radio relics have bright filamentary structures. It is not certain what causes these structures, but they have been suggested to be the result of non-homogeneous mach numbers, magnetic field strengths or, in the re-acceleration scenario, fossil plasma distribution. At the resolution of our images, in the southern relic of PSZ2 G096.88+24.18 we do not see filamentary sub-structures but a distinct east-west brightness jump. Instead, lower resolution images show diffuse radio emission expanding from the radio source S1 and bridging the gap to the southern relic (see Fig. 2.1). Extrapolating the lines drawn by the edges of the Connection to the radio relic front shows how the Connection aligns well with the brighter eastern side of the relic as well as with the edge of the brighter part of the relic on the west side (Fig. 2.5).

One possibility is that we are observing two distinct shocks (labelled E and W in Fig. 2.5) which only appear to be connected by projection effects. This is however unlikely as it would require very specific geometry for perfect alignment with the relic brightness jump to occur. Furthermore there are multiple pieces of evidence suggesting that this is indeed one single shock front, including the lack of a spectral index jump and similar spectral index distribution as a function of distance from shock front (Fig. 2.8). de Gasperin et al. (2014) reported that a changing spectral index along a radio relic may be indicative of a changing Mach number. If the southern relic in PSZ2 G096.88+24.18 is in fact composed of two shocks superimposed on each other we might expect the shocks to have different Mach numbers and therefore a sharp change in spectral index at the border of the two shocks. Fig. 2.2 shows a continuous spectral index across the brightness jump, with no sharp changes. Furthermore, the Mach numbers derived separately for the east and west sides of the radio relic agree, suggesting the southern relic can be explained by a single shock (Table 2.3). Although it is also possible that the southern relic is composed of two shocks, each with the same Mach number. Finally, the spectral index change towards the cluster centre is remarkably similar in the east and west sides of the relic (Fig. 2.8). If the magnetic field strength was significantly greater on the east than on the west we would expect the synchrotron losses, and therefore the steepening of the spectral index, downstream of the shock to be greater in the east than the west. However, Inverse Compton scattering of cosmic microwave background (CMB) photons causes additional energy losses in the downstream region and therefore affects the spectral steepening. The equivalent magnetic field for these interactions is $B_{\rm IC} = 3.2\mu G(1+z)^2$ (Longair, 2010), giving $B_{\rm IC} = 5\mu G$ at the redshift of PSZ2 G096.88+24.18. The magnetic field strengths measured in galaxy clusters are typically $\sim \mu G$ (van Weeren et al., 2019, and references therein), so we would expect synchrotron losses to be significant.

The similarities of the two sides of the radio relic suggest therefore that something may have altered the properties of the relic on the eastern side but not on the west. The most obvious candidate is the bright discrete source close to the southern radio relic, labelled S1 in Fig. 2.5. Using the catalogue of Golovich et al. (2019a) we find a cluster-member galaxy ($z = 0.304$) at the position of S1. It is plausible that we are observing sub-GeV electrons originating from the radio galaxy, which have been re-energised by the passing merger shock. There is precedent for such re-acceleration. For example, in Abell 3411-3412 the tail of a radio galaxy is connected to a radio relic (van Weeren et al., 2017). The spectral index steepens along the tail before flattening out again towards the relic, suggesting that the shock wave has re-accelerated particles in the tail. In PSZ2 G096.88+24.18 the integrated spectral index (Fig. 2.8) steepens downstream of the shock front, before flattening again towards S1. This appears to suggest a similar scenario as in Abell 3411-3412. However, the spectral index maps (Fig. 2.2) are not so clear. The parts of the Connection visible in the spectral index maps do not show a clear steepening away from S1. The spectral steepening seen in the integrated spectral index plot is likely driven by the strong surface brightness decrease in the VLA map. This decrease creates a hole in the spectral index map where the VLA flux density is below $3\sigma_{\rm rms}$ and is therefore excluded from local spectral index calculation (see Section 2.2.3.1). However, this region is detected in our LOFAR images, so contributes significantly to the integrated flux density at 140 MHz. By measuring the flux density with LOFAR we calculate an upper limit of the spectral index within the hole

to be $\alpha < -1.9$. The general spectral index steepening from S1 towards the northern edge of the relic suggests that the shock wave has passed through a radio galaxy tail, as in Abell 3411-3412. However, the complex spectral index profile makes interpretation challenging. The coincidence of the Connection with a strong decrease in surface brightness (Fig. 2.7) and the profile of the integrated spectral index along the southern relic and Connection (Fig. 2.8, red line) suggest a scenario in which the merger shock has re-accelerated sub-GeV electrons on the eastern side, whereas the west is produced by standard DSA, i.e. shock acceleration of electrons from the thermal pool. However, recent simulations by ZuHone et al. (2021) show that a merger-driven shock wave passing through the jets of an Active Galactic Nuclei (AGN) can produce an inhomogeneous cosmic ray fraction along the major axis of a shock. If this is the case in PSZ2 G096.88+24.18, this may explain the observed radio surface brightness discontinuity and therefore suggest that the east and west sides of the southern relic are generated by the same acceleration mechanism.

An alternate possibility is that the Connection is simply a product of projection effects and is in fact unrelated to S1 and instead turbulent radio halo emission, although this would not explain the surface brightness jump, polarisation and spectral index properties of the southern relic. Previous studies, for example in MACSJ1752.1+4440 (Bonafede et al., 2012), RXC J1314.4-2515 (Stuardi et al., 2019) and the Toothbrush (van Weeren et al., 2016a) suggest that in some cases there can be a connection between a merging cluster's giant radio halo and its radio relics. We investigate the possible detection of a giant radio halo in PSZ2 G096.88+24.18 in the next section.

Within standard DSA the surface brightness jump could be explained if the brighter parts of the relic mark where the merger shock has interacted with higher density upstream regions. Following the analytical model of Hoeft & Brüggen (2007), the radio power generated by standard DSA is proportional to the electron density in the shock region. If we assume that the magnetic field strength and temperature across the southern relic are constant, the eastern side of the relic would require an electron density four times greater than the western side. Such a scenario would not explain the unusual polarisation structure observed in the southern relic.

2.4.3 Candidate halo

de Gasperin et al. (2014) reported low-significance diffuse emission filling some of the ICM between the two relics in PSZ2 G096.88+24.18. They suggested that the diffuse emission could be from a radio halo. In our low resolution LOFAR images (Fig. 2.8) we observe significant diffuse emission only on the eastern side of PSZ2 G096.88+24.18, coincident with the brightest region of the candidate halo in de Gasperin et al. (2014) (labelled "Tail" in Fig. 2.5). The emission we see in LOFAR connects to uv-subtracted discrete sources (and a cluster-member galaxy, Fig. 2.5). This may suggest that the emission is of galactic origin, or a blend of diffuse emission associated with the galaxies. Within just this tail of emission we measure a flux of 7 ± 1 mJy with LOFAR, but we do not detect significant emission with VLA. We can therefore set an upper limit on the spectral index of $\alpha < -1.3$, suggesting that this is emission from fossil plasma which has become invisible at higher frequencies due to synchrotron and IC losses.

Low resolution VLA images (Fig. 2.6) show a low significance ($\leq 2\sigma_{\rm rms}$) excess at the cluster centre, as reported in de Gasperin et al. (2014). We therefore investigate the possibility that there is a radio halo in PSZ2 G096.88+24.18.

The low-mass end of radio halo correlations, for example radio halo power vs. mass, (Cassano et al., 2013; Cuciti et al., 2021) is relatively unexplored, owing to difficulty detecting radio halos in systems with comparatively low energy budgets available to inject large-scale cluster turbulence into the ICM. Detecting radio halos in low-mass systems and extending the existing studies on the correlation is therefore a crucial step forward and is indeed one of the goals of LOFAR (e.g. Cassano et al., 2012). If we measure the flux of the entire region between the two relics, avoiding S1, S2 and the Connection, we find 11 ± 3 and 0.6 ± 0.3 mJy for LOFAR and VLA respectively. We note that when excluding the bright eastern tail of emission seen in LOFAR we do not get a statistically significant detection with either LOFAR or VLA. Our flux measurements indicate a nearly 4σ detection of diffuse emission in LOFAR but only 2σ with VLA. Using the 3σ error from VLA we set an upper limit on the spectral index of candidate halo emission in PSZ2 G096.88+24.18 of $\alpha < -1.1$. This aligns with the findings of Giovannini et al. (2009), who found that radio halos typically have spectral indices of $-1.4 < \alpha < -1.1$. Our flux measurement with LOFAR corresponds to a power at 150 MHz of $P_{150\rm MHz} = (3.1 \pm 0.7) \times 10^{24}$ W/Hz.

To compare the candidate halo in PSZ2 G096.88+24.18 with confirmed halos found in other clusters we use the correlation of van Weeren et al. (2021), which gives the relation between radio halo power at 150 MHz and cluster mass. It should however be noted that the correlation is not well defined at such low masses, as there are only three clusters included in the sample with masses $<5 \times 10^{14} M_\odot$. The correlation in van Weeren et al. (2021) was calculated using the M_{500} values from *Planck*. We therefore use the *Planck*-derived mass (Planck Collaboration et al., 2016, $M_{500} = (4.7 \pm 0.3) \times 10^{14} M_\odot$) of PSZ2 G096.88+24.18 to compare with the correlation. Using this we find that our candidate radio halo lies within the errors of the correlation.

Additionally, the radio power of the candidate halo in PSZ2 G096.88+24.18 that we measure is in line with the findings of Bonafede et al. (2017). In this work they investigated the lack of giant radio halos in galaxy clusters which host a pair of radio relics, including PSZ2 G096.88+24.18. By injecting mock halos into the WSRT data from de Gasperin et al. (2014) they derived an upper limit on the radio halo power of $P_{1.4\rm GHz} = 3.8 \times 10^{23}$ W/Hz. The flux density upper limit from our VLA measurement corresponds to a power of $P_{1.4\rm GHz} = 1.8 \times 10^{23}$ W/Hz, i.e. a factor of ~ 2 smaller than the upper limit of Bonafede et al. (2017).

From our data we cannot exclude the possibility that PSZ2 G096.88+24.18 hosts a radio halo at its centre. However, most of the emission seen in LOFAR is localised to a small region connecting to discrete radio sources that have been subtracted. Additionally, one of the discrete sources coincides with a confirmed cluster-member galaxy. The brightest part of the candidate halo in VLA is on the eastern side of the ICM, suggesting that it is instead connected with the tail of emission seen in LOFAR. There may also be contribution from emission associated with discrete sources which were not fully subtracted from the *uv*-data.

2.5 Conclusions

In this paper we present LOFAR HBA (140 MHz) and VLA (1.5 GHz) radio observations and X-ray *Chandra* data of PSZ2 G096.88+24.18. With these multi-frequency observations we carry out spectral and polarisation analysis of the double radio relics in PSZ2 G096.88+24.18. Our new, high-sensitivity radio observations have revealed the presence of a patch of diffuse emission (Connection) connecting a radio galaxy (S1) with the southern relic. The Connection coincides with a region in the radio relic in which there is a factor of ∼4 increase in surface brightness. Spectral analysis reveals a complex spectral index profile. The integrated spectral index steepens along the Connection, away from S1, which appears to suggest re-acceleration of an AGN lobe. The radio surface brightness discontinuity across the relic extension may suggest a scenario in which electrons are accelerated from the thermal pool on the western side of the relic, but re-accelerated from a pre-existing population of sub-GeV electrons in the east. Alternatively, some simulations suggest that shock passage across an AGN lobe can naturally reproduce the surface brightness gradient. Our other findings are as follows:

- We confirm the detection of a pair of diametrically opposed radio relics in PSZ2 G096.88+24.18. The relics are approximately equidistant from the cluster centre, ∼ 1.1 and 1.0 Mpc for the northern and southern relics respectively. The radio relics have LLS of ∼ 0.9 and 1.5 Mpc and a flux ratio of 1:3.5.

- The spectral index across the radio relics steepens away from the shock fronts, as expected from synchrotron and IC losses. The spectral index steepens from $\alpha = -0.5$ and $\alpha = -0.6$ to $\alpha = -1.5$ and $\alpha = -2.0$, for the northern and southern relics respectively. By measuring the spectral index along the shock fronts we derive Mach numbers of $\mathcal{M} = 2.5 \pm 0.2$ and $\mathcal{M} = 2.3 \pm 0.2$. These are significantly lower than those derived from the integrated spectral index of both radio relics.

- We were unable to detect evidence of a shock in the *Chandra* X-ray at either of the positions of the radio relics. However, the observation may not be deep enough to detect a shock and the location of the southern relic at the edge of two CCD chips makes observation of a shock even more challenging.

- Measurements of the polarised emission at 1.5 GHz detected by VLA reveal areas of up to 60% linearly polarised emission in the northern relic. The polarisation vectors, corresponding to the electric field, lie approximately perpendicular to the shock front, as expected for shock compression of magnetic fields. In the southern relic only small patches, at the brightest points in the relic, show very weakly polarised emission ($\leq 20\%$). The electric field vectors lie at an angle relative to the shock-normal. We suggest that this could be caused by turbulence in the southern relic. The differences in the north and south relics suggest that the Connection is playing a role in this turbulence.

- Low resolution LOFAR images show significant diffuse emission on the eastern side of PSZ2 G096.88+24.18, between the radio relics. The emission is localised to a tail of emission connecting to discrete radio sources, one of which coincides with

Table 2.4: VLA Calibrator Sources

Observation Date	Calibrators			
	Primary	Polarisation Angle	Instrumental Polarisation	Phase
2016 Feb 01	3C286	3C286	J1407+2827	J2022+6136
2015 Feb 05	3C286	3C286	J1407+2827	J2022+6136
2015 Feb 02-03	3C147	3C138	3C147	J2022+6136

a spectroscopically-confirmed cluster-member galaxy. From the non-detection in VLA we set an upper limit on the spectral index at $\alpha < -1.3$. We suggest that this is most likely emission from previous activity of a radio galaxy.

- We consider the possibility that this emission is instead a candidate radio halo, as previously suggested in de Gasperin et al. (2014). We find that the 150 MHz radio power lies on the $P_{150\mathrm{MHz}} - M_{500}$ correlation of van Weeren et al. (2021), using the *Planck*-derived mass.

2.6 Appendix A: VLA calibrator sources

Multiple calibrator sources are observed by VLA to properly calibrate each observation (see Section 2.2.2). The primary, polarisation and phase calibrators for each observation used in this paper are listed in Table 2.4.

2.7 Appendix B: Spectral index error maps

The 140 - 1500 MHz spectral index was calculated for each pixel above $3\sigma_{\mathrm{rms}}$ in both the LOFAR and VLA images. The resulting spectral index map is shown in Fig. 2.2. Fig. 2.9 shows the corresponding spectral index error maps, calculated using Equation 2.2 for each pixel.

Acknowledgements

FdG and MB acknowledge support from the Deutsche Forschungsgemeinschaft under Germany's Excellence Strategy - EXC 2121 "Quantum Universe" - 390833306. VC acknowledges support from the Alexander von Humboldt Foundation. DNH acknowledges support from the ERC through the grant ERC-Stg DRANOEL n. 714245. AB acknowledges support from the VIDI research programme with project number 639.042.729, which is financed by the Netherlands Organisation for Scientific Research (NWO). WF, CJ and RK acknowledge support from the Smithsonian Institution and the Chandra High Resolution Camera Project through NASA contract NAS8-03060. RJvW acknowledges

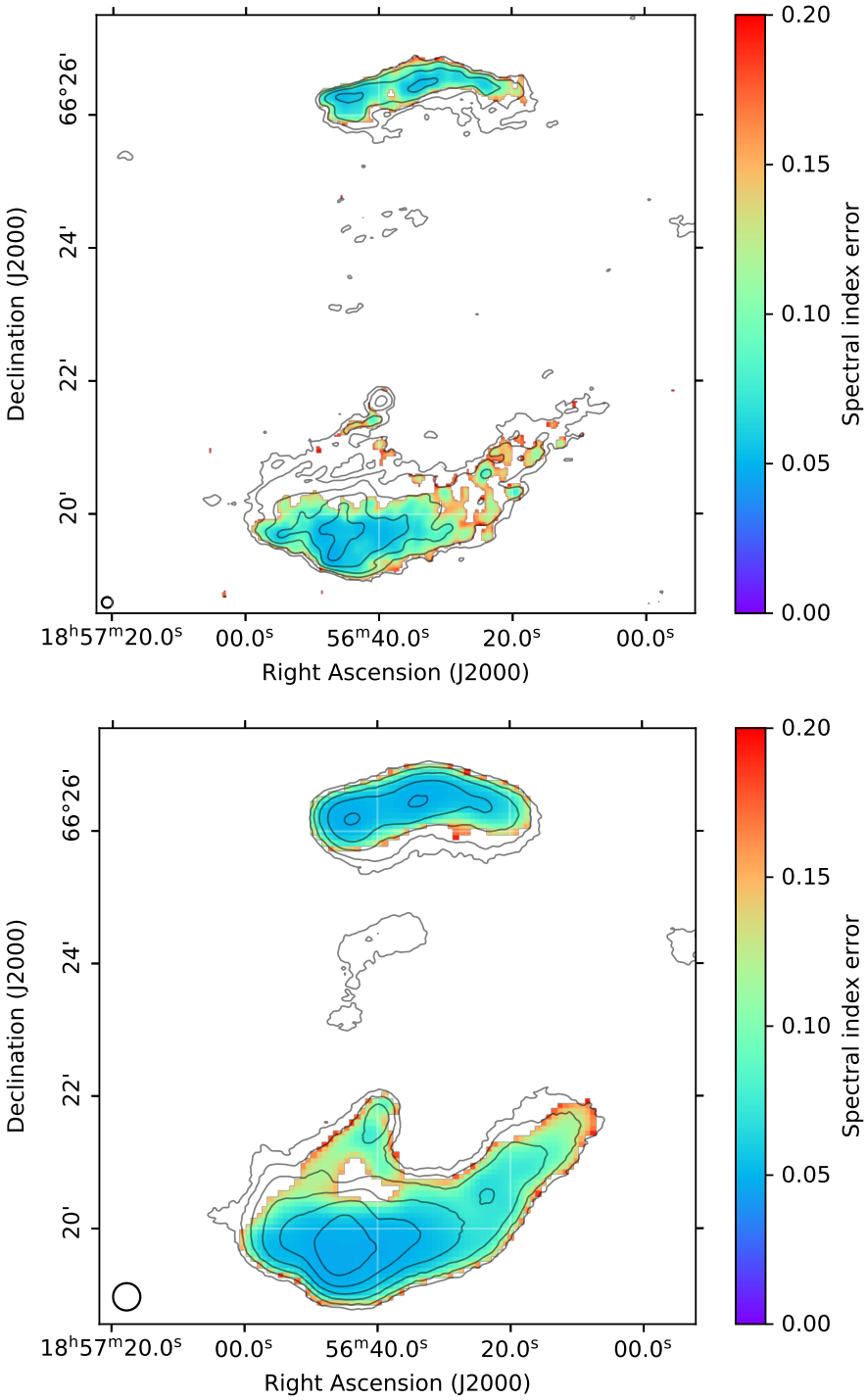

Figure 2.9: Spectral index error maps for Fig. 2.2.

support from the ERC Starting Grant ClusterWeb 804208. This paper is based (in part) on data obtained with the International LOFAR Telescope (ILT) under project code LC9_036. LOFAR (van Haarlem et al., 2013) is the Low Frequency Array designed and constructed by ASTRON. It has observing, data processing, and data storage facilities in several countries, that are owned by various parties (each with their own funding sources), and that are collectively operated by the ILT foundation under a joint scientific policy. The ILT resources have benefitted from the following recent major funding sources: CNRS-INSU, Observatoire de Paris and Université d'Orléans, France; BMBF, MIWF-NRW, MPG, Germany; Science Foundation Ireland (SFI), Department of Business, Enterprise and Innovation (DBEI), Ireland; NWO, The Netherlands; The Science and Technology Facilities Council, UK. The National Radio Astronomy Observatory is a facility of the National Science Foundation operated under cooperative agreement by Associated Universities, Inc. The scientific results reported in this article are based in part on observations made by the Chandra X-ray Observatory.

Chapter 3

The Planck clusters in the LOFAR sky VI. LoTSS-DR2: Properties of radio relics

A. Jones, F. de Gasperin, V. Cuciti, A. Botteon, X. Zhang, F. Gastaldello, T. Shimwell, A. Simionescu, M. Rossetti, R. Cassano, H. Akamatsu, A. Bonafede, M. Brüggen, G. Brunetti, L. Camillini, G. Di Gennaro, A. Drabent, D. N. Hoang, K. Rajpurohit, R. Natale, C. Tasse, R. J. van Weeren

Accepted for publication in Astronomy & Astrophysics, 05 December 2022

Abstract

Context: It is well-established that shock waves in the intracluster medium launched by galaxy cluster mergers can produce synchrotron emission, which is visible to us at radio frequencies as radio relics. However, the particle acceleration mechanism producing these relics is still not fully understood. It is also unclear how relics relate to radio halos, which trace merger-induced turbulence in the intracluster medium.
Aims: We aim to perform the first statistical analysis of radio relics in a mass-selected sample of galaxy clusters, using homogeneous observations.
Methods: We analysed all relics observed by the Low Frequency Array Two Metre Sky Survey Data Release 2 (LoTSS DR2) at 144 MHz, hosted by galaxy clusters in the second *Planck* catalogue of SZ sources (PSZ2). We measured and compared the relic properties in a uniform, unbiased way. In particular, we developed a method to describe the characteristic downstream width in a statistical manner. Additionally, we searched for differences between radio relic-hosting clusters with and without radio halos.
Results: We find that, in our sample, $\sim$ 10% of galaxy clusters host at least one radio relic. We confirm previous findings, at higher frequencies, of a correlation between the relic-cluster centre distance and the longest linear size, as well as the radio relic power

and cluster mass. However, our findings suggest that we are still missing a population of low-power relics. We also find that relics are wider than theoretically expected, even with optimistic downstream conditions. Finally, we do not find evidence of a single property that separates relic-hosting clusters with and without radio halos.

3.1 Introduction

Mergers of galaxy clusters generate shock waves that propagate through the intracluster medium (ICM). Since the characterisation of a cluster shock by Markevitch et al. (2002) with *Chandra*, many more have been found using measurements of the X-ray surface brightness, entropy, and temperature profiles of cluster outskirts (e.g. Ogrean & Brüggen, 2013; Shimwell et al., 2015; Eckert et al., 2016; Akamatsu et al., 2017; Urdampilleta et al., 2018). The connection between radio relics (RRs) and merger shocks has been well-established by a number of shocks detected in X-rays, as ICM density and temperature discontinuities, at the location of a RR (e.g. Finoguenov et al., 2010; Bourdin et al., 2013; Akamatsu & Kawahara, 2013; Botteon et al., 2016a,b). There is also clear evidence of the relation between RRs and galaxy cluster merger events from both weak lensing studies (e.g. Jee et al., 2016; Finner et al., 2017) and optical spectroscopy (e.g. Golovich et al., 2019a). Not all RRs have a known associated shock, though this is likely the result of difficulties in shock detection from the low X-ray counts in cluster outskirts, where relics are typically located (Vazza et al., 2012; Ogrean et al., 2013). Fermi-I, diffusive shock acceleration (DSA) is typically adopted to explain the generation of RRs from cluster shocks (Enßlin et al., 1998). In DSA, charged particles are accelerated to relativistic energies by scattering upstream and downstream off magnetic inhomogeneities (Fermi, 1949; Blandford & Eichler, 1987). Due to the presence of cluster-scale magnetic fields, they emit synchrotron emission, which is observable as diffuse, roughly arc-like RRs (also known as cluster radio shocks, see Brunetti & Jones, 2014; van Weeren et al., 2019, for reviews). The power-law energy spectrum of cosmic-ray electrons (CRes) produced by DSA generates a radio brightness profile in line with observations (e.g. Hoeft & Brüggen, 2007; Kang et al., 2012). Additionally, relics are typically observed to have high polarisation fractions ($\gtrsim 20\% - 60\%$), matching expectations of magnetic field alignment along the shock surface (Enßlin et al., 1998). However, DSA from the thermal pool cannot entirely explain the properties of RRs. A study by Botteon et al. (2020a) found that acceleration of CRes from the thermal pool via DSA, in such weak shocks ($\mathcal{M} \lesssim 3$), is in most cases insufficient to explain the acceleration efficiencies required to produce the luminosity of relics. Re-acceleration of a pre-existing population of mildly relativistic CRes could relieve some of this tension (e.g. Markevitch et al., 2005; Kang & Ryu, 2011; Pinzke et al., 2013). There is morphological and spectral evidence that the tails of radio galaxies can provide seed electrons that are re-accelerated by shocks (e.g. Bonafede et al., 2014; van Weeren et al., 2017; Di Gennaro et al., 2018). For example, van Weeren et al. (2017) found that the RR in Abell 3411-3412 is connected to the tail of a cluster-member radio galaxy. Moreover, the energy spectrum steepens along the tail, consistent with radiative losses, and subsequently flattens again at the inner boundary of the RR, implying re-acceleration. There are, however, still relatively few relics for which there is evidence

of a connection/re-acceleration in general.

In addition to giant shock waves, galaxy cluster mergers generate turbulence in the ICM. This turbulence cascades down to smaller scales and can (re-)accelerate CRes and produce radio synchrotron emission, in the form of a radio halo (RH, see Brunetti & Jones, 2014, for a review). These RHs are typically located in the cluster centre and follow the morphology of the X-ray-emitting gas. Numerous statistical studies of RHs have been performed and have shown a correlation between the RH power and its host cluster mass (e.g. Basu, 2012; Cassano et al., 2013; van Weeren et al., 2021; Cuciti et al., 2021), as well as with the X-ray luminosity (e.g. Liang et al., 2000; Brunetti et al., 2009). In contrast, there have been relatively few statistical studies of RRs. Such investigations of relic properties are more challenging than for RHs due to a number of observational constraints. For example, the lower abundance of RRs (in $\sim$ 5% of clusters, Kale et al., 2015), compared to that of RHs (in $\sim$ 40% of clusters, e.g. Cuciti et al., 2021), and the typical location in the cluster periphery, where X-ray counts are low, make such studies challenging. Additionally, an unbiased measurement of the properties of relics is difficult, due to projection effects and their irregular morphologies. In the first statistical study of RRs, van Weeren et al. (2009) compiled all of those discovered (26 individual RRs) at that time from the literature. They discovered a correlation between the longest linear size (LLS) of a relic and its distance from the cluster centre. This finding was corroborated by de Gasperin et al. (2014) (hereafter FdG14) and was found at low significance by Bonafede et al. (2012), who both restricted their analysis to only double radio relics (dRRs), that is to say pairs of diametrically opposed relics in the same cluster. The advantage of using dRRs is that the merger axis is relatively well-known and approximately on the plane of the sky (van Weeren et al., 2011; Golovich et al., 2019a), minimising projection effects. FdG14 also reported a correlation between host-cluster mass and RR power at 1.4 GHz, that is to say that more powerful relics are typically located in higher-mass clusters. However, simulations by Nuza et al. (2017) and Brüggen & Vazza (2020) suggest that we are missing a significant number of low-power relics, likely only detectable at low frequencies, and that the cluster mass provides a maximum radio power a relic can reach, rather than directly determining its power. The advent of sensitive, all-sky surveys at low radio frequencies will enable discovery of these low-power relics, if such a population exists.

In this paper we present the first statistical study of RRs at 150 MHz and their connection to RHs, using galaxy clusters covered by both the *Planck* PSZ2 catalogue (Planck Collaboration et al., 2016) and the Low Frequency Array (LOFAR) Two Metre Sky Survey Data Release 2 (LoTSS DR2, Shimwell et al., 2022). Wherever possible, this was supplemented with archival *Chandra* and *XMM-Newton* data, to determine the X-ray properties of the sample clusters, which are described fully in Zhang et al. (2023). The biggest advantage of using such a sample is that it allows us to study RRs observed by the same telescope, and therefore approximately the same uv-coverage, observing frequency and sensitivity to compact and diffuse emission. Additionally, the observations were calibrated and the images produced in a uniform manner (see Tasse et al., 2021; Shimwell et al., 2022). The use of the PSZ2 catalogue allows us to produce a mass-selected sample, ensuring that our results are representative of those RRs observable at the sensitivity of LOFAR. This paper

is the sixth in a series of papers[1] utilising the LoTSS DR2 - PSZ2 cluster sample to explore the properties of diffuse radio emission in the ICM. (Botteon et al., 2022) describes the sample in detail, the methods and data used and the source classification. The occurrence and scaling relations of all RHs in this sample are presented in Cassano et al. (2023) and Cuciti et al. (2023), respectively, whilst upper limits on RH power in clusters with no detected diffuse emission are in Bruno et al. (2023). An analysis of the X-ray properties of the sample is presented in Zhang et al. (2023). See also Hoang et al. (2022) for analysis of diffuse radio emission within LoTSS DR2 in non-PSZ2 clusters.

The paper is structured as follows. Sec 3.2 describes the sample of relics and how we measured their properties. In Sec. 3.3 we present our results. In Sec. 3.4 and Sec. 3.5 we discuss our results and conclude. We adopt a fiducial ΛCDM cosmology with $\Omega_\Lambda = 0.7$, $\Omega_m = 0.3$, and $H_0 = 70$ km s^{-1} Mpc^{-1}. All errors are at 1σ, unless otherwise stated.

3.2 The sample

We provide here a summary of the sample of relics used in this paper, its composition and the measurement of relic properties. For a full description of the cluster sample, including the data calibration, imaging procedure, and radio source classification, we refer the reader to Botteon et al. (2022).

3.2.1 Relics in LoTSS DR2

Of the 1653 galaxy clusters contained in the *Planck* PSZ2 catalogue (Planck Collaboration et al., 2016), 309 lie within the LoTSS DR2 footprint (Shimwell et al., 2022). The LoTSS DR2 data were reprocessed to produce 144 MHz radio images, at various resolutions, for each cluster (Botteon et al., 2022). The radio images were then visually inspected for evidence of diffuse emission not associated with an AGN. Elongated ($\gtrsim$ 300 kpc) diffuse emission with a sharp radio edge, lying outside the bulk of X-ray emission, in the cluster outskirts, was classified as a RR. Of those, relics diametrically opposed to another relic on the opposite side of its cluster were defined as dRRs. Some clusters host more than one RR, but do not fit this criterion and were therefore classified as multiple radio relics (mRRs). We use archival *Chandra* and *XMM-Newton* data to determine the cluster X-ray properties. The data are processed and used to produce images, smoothed to 30 kpc at the cluster redshift (see Botteon et al., 2022, for further details). A full analysis of the X-ray properties of the LoTSS DR2 - PSZ2 sample will follow in Zhang et al. (2023). For clusters with no *Chandra* or *XMM-Newton* observation, the emission was classified as a candidate radio relic (cRR), since it is not possible to define the location of the diffuse emission with respect to the ICM. In this case, the position of the radio emission with respect to the cluster optical overdensity was used. The resulting sample consists of 26 relic-hosting clusters, of which 20 have accompanying X-ray observations. Of the 35 individual relics residing in these clusters, 12 were defined as dRRs, 5 as mRRs and 6 as

[1] https://lofar-surveys.org/planck_dr2.html

cRRs. The rest (12) were defined as RRs. There are no double, or multiple, candidate radio relics. For an image gallery of all RRs in our sample, and, where possible, their location with respect to the ICM X-ray emission, see Appendix 3.6. Images and tables are taken from Botteon et al. (2022) and can be found at full resolution on the project website [2].

Radio halos in the LoTSS DR2 - PSZ2 sample were classified by Botteon et al. (2022). They were defined as extended radio sources occupying the same region as either the bulk ICM X-ray emission (RHs) or an overdensity of optical galaxies (cRHs). Of the 26 relic-hosting clusters, 12 also host a radio halo (11 RHs and 1 cRH). For some radio objects, originally classified as RHs, the low signal-to-noise ratio did not allow fitting of the model used to estimate RH flux (denoted RH*s/cRH*s, see Botteon et al., 2022, for more detail). We treated clusters which host such RH*s/cRH*s as hosting a RH, though there is only 1 relic-hosting cluster for which this is the case (PSZ2 G116.50-44.47, classified as RH*).

Fig. 3.1 shows the mass distribution of all clusters in the LoTSS DR2 - PSZ2 sample, as a function of redshift, where the mass is M_{500} from the PSZ2 catalogue (Planck Collaboration et al., 2016). Clusters which host at least one RR are shown as red points. PSZ2 G107.10+65.32 is comprised of two sub-clusters, each undergoing its own merger (Abell 1758, Botteon et al., 2020b). We have plotted this cluster separately, as a red star, since only the S sub-cluster hosts a RR, but, since the resolution of *Planck* is not sufficient to separate the two sources, the mass given in the PSZ2 catalogue is likely from a combination of the two sub-clusters. The blue dashed line shows the mass at which Planck is 50% complete, as a function of redshift. This line comes from converting the selection function from the *Planck* archive from SZ signal - cluster size to mass - redshift (Planck Collaboration et al., 2016) and taking the boundary at which the probability of detecting a cluster is 50%. The only relic-hosting cluster which lies below this line is PSZ2 G069.39+68.05. Throughout this paper, we consider only clusters lying above this line as our representative cluster sample and restrict our analysis to only these clusters. However, since there is only one relic-hosting cluster below the line (PSZ2 G069.39+68.05) and one for which we cannot be certain (PSZ2 G107.10+65.32), we plot these two relics whenever possible and label them accordingly, despite their absence from our analysis.

3.2.2 Relic measurements

All measurements used in this paper are presented in Botteon et al. (2022) (Table A.4.). For completeness, we describe the procedures used below.

Radio relics, owing to their often complex morphologies, do not lend themselves well to parametric model-fitting procedures, such as those used for RHs (Boxelaar et al., 2021). Connections of relics to radio galaxies, or even RHs, makes automatically separating relic from non-relic emission very challenging. Therefore, to best enable fair comparison of relic properties, we adopted a hybrid approach to their measurement. For each relic we manually defined a region which best covers it, whilst avoiding non-relic emission, by visually

[2] https://lofar-surveys.org/planck_dr2.html

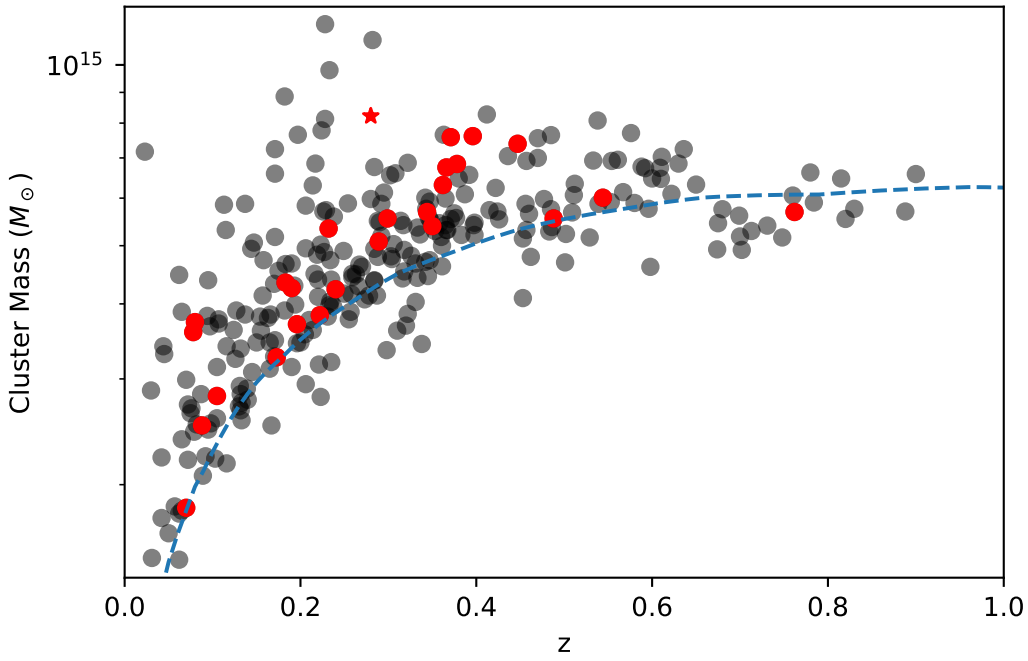

Figure 3.1: Cluster M_{500} mass vs. redshift for all clusters in the LoTSS DR2 - PSZ2 sample. Red circles denote clusters which host at least one RR. Black circles denote all other clusters in the LoTSS DR2 - PSZ2 sample (Botteon et al., 2022). PSZ2 G107.10+65.32 S is plotted as a red star, since the mass reported in the PSZ2 catalogue likely comes from both sub-clusters, PSZ2 G107.10+65.32 N and PSZ2 G107.10+65.32 S. The 50% PSZ2 completeness line is shown in blue.

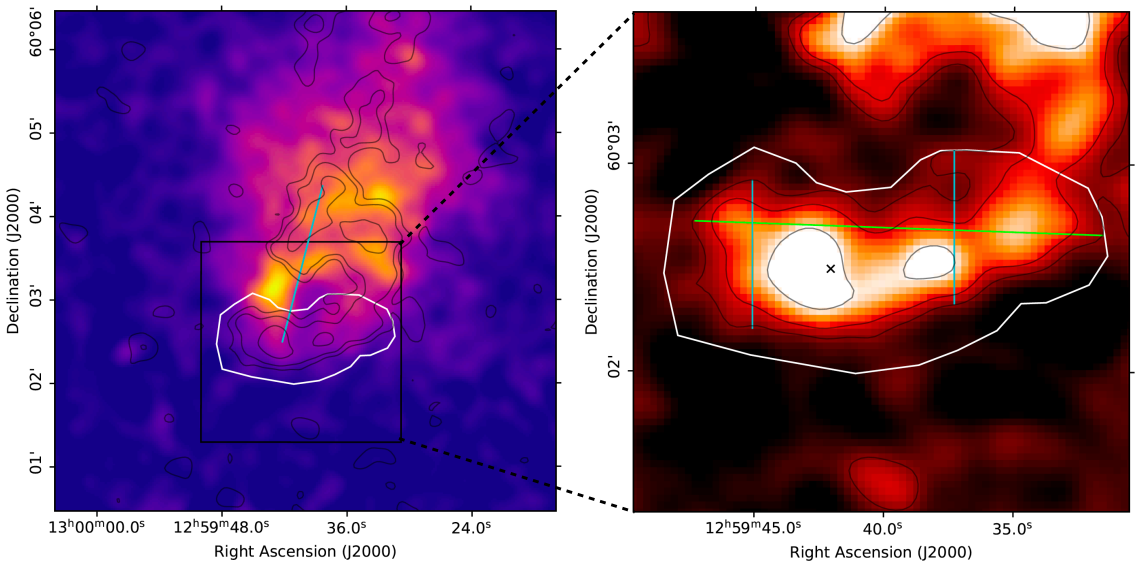

Figure 3.2: Reference images of the relic in PSZ2 G121.03+57.02. The white region shows the region used to compute the properties of the relic. Black lines show the $2\sigma_{rms} \times [1, 2, 4, ..]$ contours from the 50 kpc-taper, compact-source-subtracted LOFAR image from Botteon et al. (2022). **Left**: *Chandra* X-ray image. The cyan line scales the distance between the relic position and the cluster centre, as defined in Sec. 3.2.2. **Right**: Zoom-in of the 50-kpc-taper, compact-source-subtracted LOFAR, centred on the relic. The green line shows the LLS of the relic. Two example lines used to measure the relic width are shown in cyan. The black cross is where we define the relic coordinate.

inspecting the radio and X-ray images. In general, we uniformly computed the properties of each relic from the 50 kpc-taper, compact-source-subtracted image of each cluster, where we defined relic emission as emission above $2\sigma_{rms}$ within the pre-defined region. σ_{rms} is the rms noise of the image. A few relics required slightly different treatment. The relics PSZ2 G089.52+62.34 N2 (Abell 1904), PSZ2 G091.79-27.00, PSZ2 G113.91-37.01 S, PSZ2 G166.62+42.13 E (Abell 746), and PSZ2 G205.90+73.76 N/S are not fully visible in the 50 kpc-taper images. We therefore chose to use the 100 kpc-taper images instead. Additionally, visual inspection of the model used to subtract compact sources in images of PSZ2 G190.61+66.46 revealed that it included some relic emission. Since there are no compact sources within the relic, we chose to use the 50 kpc-taper image without compact-source subtraction for this relic.

Fig. 3.2 shows a reference image of PSZ2 G121.03+57.02, demonstrating the measurement of relic properties, as detailed below. The left panel shows the location of the relic, outside the bulk of ICM X-ray emission. The right panel shows a zoom-in of the relic from the 50 kpc-taper LOFAR image. The region used for this relic and the $\geq 2\sigma_{rms}$ contours are shown as white and black lines, respectively.

Since the LOFAR images are at a nominal frequency of 144 MHz, we computed the relic flux and power at 150 MHz, assuming $\alpha = -1$, where α is the spectral index

($S_\nu \propto \nu^\alpha$). The spectral index of RRs is typically in the range $-1 \lesssim \alpha \lesssim -1.5$ (e.g. Feretti et al., 2012, FdG14). Since the frequency conversion is small and the clusters in our sample are relatively nearby, the choice of α in this range is somewhat arbitrary. If we instead choose $\alpha = -1.5$, corresponding to a steep-spectrum RR, the k-corrected 150 MHz RR power is $\lesssim 10\%$ greater, in most cases. Since the k-correction factor for a source with spectral index $\alpha = -1$ is zero, we did not need to k-correct our luminosities. The errors take into account a combination of the error from the rms noise and a 10% calibration error (Shimwell et al., 2022). We also included an error to account for residuals from the compact-source subtraction process. We split the images into four groups, based on their total discrete-source flux density, $S_{discrete}$, and assigned an appropriate fractional error which increases with $S_{discrete}$ (see Botteon et al., 2022).

The LLS was calculated as the distance between the two pixels with maximum separation which were defined as part of the relic emission. Since the synthesised beam is the smallest angular scale across which we can trust the flux, the error in the LLS corresponds to one beam width. We used the same approach for all other distance measurements presented in this paper. We note that this can be considered a lower limit of the LLS, since we are limited by how much of the RR is detected. The LLS of PSZ2 G121.03+57.02 is shown in Fig. 3.2 as a green line.

Due to the often complex relic morphologies, the measurement of the relic extent downstream of the shock front, or relic width, is strongly dependent on the location at which it is measured. This makes it extremely difficult to measure a single width value in a consistent way which is fair for all relics in our sample. We therefore took a statistical approach, by measuring the width at many positions along the relic. In the case of a shock propagating outwards, the LLS should be oriented approximately perpendicular to the direction of propagation, that is perpendicular to the upstream - downstream direction. This orientation was verified by eye, though we do not account for any curvature of the relic. We could therefore, at each pixel along the LLS, draw a line perpendicular to the LLS and calculate the maximum distance between relic pixels which lie on it. The blue lines in Fig. 3.2 (right) show two example lines used to calculate the width of the relic in PSZ2 G121.03+57.02. We then took the median of all values measured as the characteristic relic width and one standard deviation as its error. We chose to take the median as our characteristic width because it minimises the effect of small width measurements at the relic edges and areas with abnormally large widths. As with the LLS, the width measurements we made are lower limits, since the entire downstream extent of the RRs may be too faint to detect.

Without a direct detection of a shock front, it is not necessarily clear where the shock front producing a RR is located. There is still debate over the nature of the bright filaments often observed in RRs. However, a detailed, high-resolution study of the relics in Abell 3667 by de Gasperin et al. (2022) suggests that the filaments trace regions of shock acceleration. Recent simulations support the scenario that the brightest RR regions correspond to the highest Mach numbers (e.g. Domínguez-Fernández et al., 2021; Wittor et al., 2021). We therefore took the flux-weighted centre of the brightest 10% of relic pixels as the location of the RR. The coordinate calculated for PSZ2 G121.03+57.02 is shown as a black cross in Fig. 3.2 (right). We subsequently used this point to calculate

the distance to the cluster centre, D_{RR-c}, where we considered the X-ray centroid of a cluster, measured within R_{500}, its centre (shown as black crosses in Fig. 3.15) and to other relics, D_{RR-RR}, for dRRs. We note that, since the cRRs in our sample are those without accompanying X-ray images (see Sec. 3.2.1), we do not measure D_{RR-c} for any cRRs. We included an additional error in these distance measurements to account for possible projection effects. The merger axes of dRR-hosting clusters are expected to lie on, or close to, the plane of the sky (van Weeren et al., 2011). We therefore set this additional error as the distance corresponding to a 10°offset. For all other relics, we use an offset of 30°.

3.3 Results

In this section, we report our results on the statistical properties of RRs and their host clusters. In general, throughout the figures, cRRs are denoted by triangular data points, dRRs by plusses, and all other relics, including mRRs, by circles. This notation extends to graphs with one data point per cluster, that is to say that clusters which host dRRs are plotted as a plus, etc.. Additionally, though not included in all graphs, data points with surrounding red circles denote clusters which also host an RH/cRH. Due to the ambiguity in PSZ2 G069.39+68.05 (below 50% *Planck* completeness, see Fig. 3.1) and PSZ2 G107.10+65.32 (double cluster, see Sec. 3.2.1 for more details), whenever possible, we label the points as '069' and '107' respectively, if they are included. We did not include these relics at all when plotting histograms, since they are not easily labelled. Since we did not include them when assessing the presence of a correlation, we also excluded them from the corresponding plots.

3.3.1 X-ray morphological disturbance

The dynamical state of the clusters in our sample is assessed using the 30 kpc-smoothed *Chandra* and *XMM-Newton* images. With these we are able to calculate the cluster concentration parameter (Santos et al., 2008),

$$c = \frac{F(r < R_{core})}{F(r < R_{ap})}, \tag{3.1}$$

where F is the X-ray flux, R_{core} the aperture of the core region and R_{ap} the outer aperture, and centroid shift (Mohr et al., 1993; Poole et al., 2006),

$$w = \left[\frac{1}{N_{ap} - 1} \sum_i \left(\Delta_i - \bar{\Delta}\right)^2 \right]^{1/2} \frac{1}{R_{ap}}, \tag{3.2}$$

where N_{ap} is the number of apertures, Δ_i the centroid of the ith aperture, and $\bar{\Delta}$ the average centroid. R_{core} and R_{ap} were set following the convention of Cassano et al. (2010), that is 100 kpc and 500 kpc, respectively.

In Fig. 3.3 we plot the cluster concentration parameter, c against the centroid shift, w, for all clusters in the LoTSS DR2 - PSZ2 sample above the *Planck* 50% completeness line.

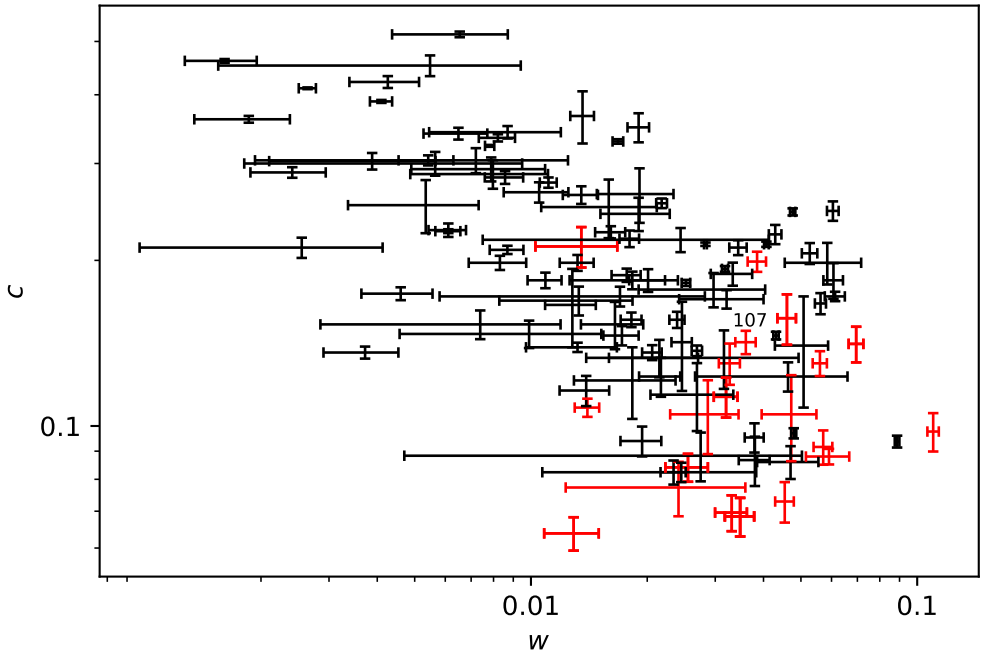

Figure 3.3: Concentration parameter, c vs. centroid shift, w for all clusters with X-ray observations above the *Planck* 50% completeness line in the DR2 sample. Relic-hosting clusters are denoted by red points. All other clusters are black. PSZ2 G107.10+65.32 is labelled, with the label directly above the data point.

The values, and corresponding errors, for all clusters are given in Botteon et al. (2022) and Zhang et al. (2023).

The plot shows the c and w parameters with their corresponding errors. We note that the combination of *Chandra* and *XMM-Newton* measurements and corresponding uncertainties, where available, gives rise to large errors in clusters where the two instruments disagree significantly. This is likely caused by differences in PSF and X-ray count rate between the two instruments. In general, however, there is good agreement of the concentration parameter and centroid shift between the two instruments (see Zhang et al., 2023, for a full discussion). However, there are no relic-hosting clusters which have large discrepancies between their *Chandra*-derived and *XMM-Newton*-derived morphological parameters. There is no clear bi-modal distribution representing disturbed and relaxed clusters, but, in general, clusters with smaller c and larger w are more dynamically disturbed. Relic-hosting clusters are shown in red, with all other clusters in black. We see that relic-hosting clusters primarily reside in the bottom right corner of the plot, corresponding to the most disturbed systems. Interestingly, the least disturbed cluster in the RR sample, PSZ2 G205.90+73.76, hosts both a RH and a dRR pair.

Cuciti et al. (2023) define a quantity, 'disturbance', using the c and w values of the clusters in our sample. This quantity has no physical meaning, but is useful to compare 'disturbed' and 'relaxed' clusters, since larger values correspond to more dynamically

disturbed clusters. For clarity, we summarise its calculation here. We first normalised the values of c and w, to account for the different ranges covered by each, with

$$\mathcal{P}_{\rm norm} = \frac{\log(\mathcal{P}_i) - \min(\log(\mathcal{P}))}{\max(\log(\mathcal{P})) - \min(\log(\mathcal{P}))}, \tag{3.3}$$

where $\mathcal{P}$ represents either c or w. We then fit a line of the form $\log_{10}(c_{\rm norm}) = m \log_{10}(w_{\rm norm}) + q$ to the $c_{\rm norm}$ and $w_{\rm norm}$ data for all clusters with accompanying X-ray observations in the full LoTSS DR2 - PSZ2 sample. We derived the projected position of each cluster along this line and assumed that the cluster with X-ray disturbance = 0 is the first along the line starting from the top left corner of the plot. The disturbance of the other clusters was calculated as the distance along the same line from the cluster with disturbance = 0. We note that this quantity is similar to the relaxation score, $\mathcal{R}$, calculated by Zhang et al. (2023). Both quantities combine the two morphological parameters we have, c and w, into one, which describes the dynamical state of a cluster. The two quantities approximately anti-correlate, that is to say that lower $\mathcal{R}$ is associated with higher values of disturbance. In our analysis, we chose to use the disturbance, since we remain consistent with the disturbance values for the RHs in the LoTSS DR2 - PSZ2 sample from Cuciti et al. (2023) and Cuciti et al. (2021). This disturbance represents the same information as the disturbance calculated by Cuciti et al. (2021), that is the logarithmic distance from the bisector of the median c and w values from Cassano et al. (2010) ($c = 0.2$, $w = 0.012$). The advantage of our method is that it does not rely on the somewhat arbitrary bisector slope and median c and w values. In Fig. 3.4 we plot the cluster disturbance distribution for all clusters above the *Planck* 50% completeness line in the LoTSS DR2 - PSZ2 sample with c and w measurements. The disturbance of all clusters is shown in grey, with all clusters hosting a RR in red. The clusters which host both a RR and a RH are shown by hatched black bars. As seen in the c - w plot, relic-hosting clusters are among the most disturbed in our sample. There is no obvious difference between the disturbances of relic-hosting clusters which also host a RH and those that don't.

3.3.2 Radio relic scaling relations

For each of the relations reported in the following subsections, we calculated Spearman's rank correlation coefficient and report its associated p-value. We assessed the presence of a correlation both including and excluding cRRs. PSZ2 G069.39+68.05 and PSZ2 G107.10+65.32 were excluded in both cases. The p-values for the correlations in the following subsections are reported in Tab. 3.1. We considered the null hypothesis to be rejected if $p < 0.05$, where the null hypothesis we are testing is that the variables X and Y are not correlated.

If the null hypothesis was rejected, we fit our data, using BCES linear regression methods (Akritas & Bershady, 1996), to the equation $\log_{10}(X) = B \log_{10}(Y) + A$. This was done separately, both including and excluding the cRRs in our sample. We then calculated the 95% confidence interval of our line of best fit as

$$\Delta Y = \pm \sqrt{\left[\sum_{i=0}^{N} \frac{(Y_i - Y_m)^2}{N-2}\right]\left[\frac{1}{N} + \frac{(X - X_m)^2}{\Sigma_{i=0}^{N}(X_i - X_m)^2)}\right]}, \tag{3.4}$$

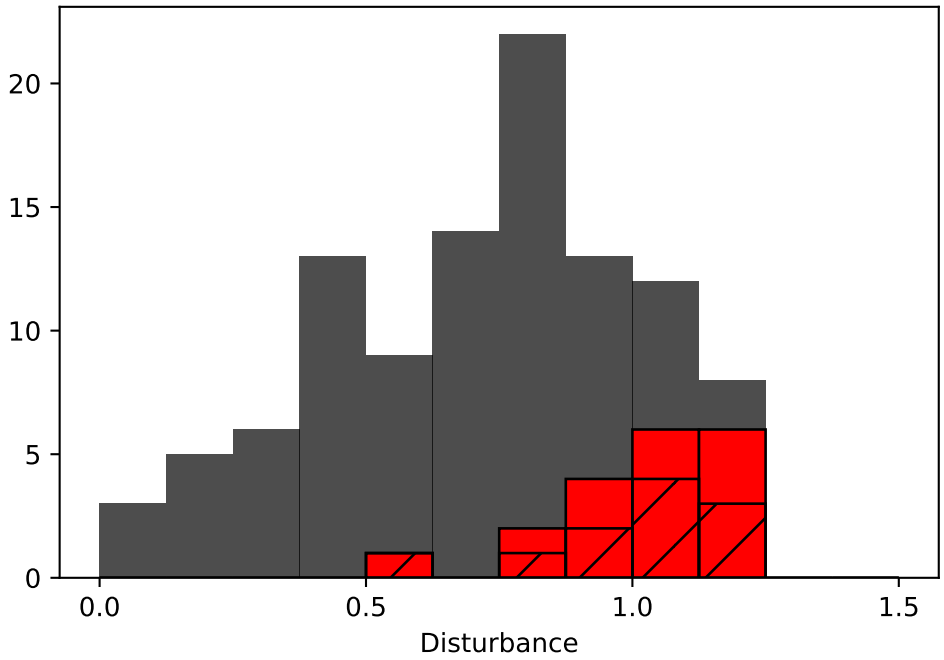

Figure 3.4: Histogram of cluster disturbances. The grey bars show the distribution of all clusters above the *Planck* 50% completeness line in the LoTSS DR2 - PSZ2 sample with c and w measurements. The red bars show the distribution of all clusters which host a RR and the hatched bars show the clusters which host both a RR and RH. PSZ2 G107.10+65.32 is excluded entirely.

Correlation	p-value	
	cRRs Excluded	cRRs Included
$P_{150\mathrm{MHz}}$ - M_{500}	0.003	0.003
$P_{150\mathrm{MHz}}$ - LLS	0.261	0.029
LLS - D_{RR-c}	0.002	-
LLS - D_{RR-c}/R_{500}	< 0.001	-

Table 3.1: Spearman rank correlation coefficient p-values for RR power - cluster mass, RR power - LLS, LLS - distance from cluster centre and LLS - distance from cluster centre as a fraction of R_{500} correlations. The p-value is calculated separately with and without candidate relics included. There is no p-value including cRRs in the LLS - D_{RR-c}, nor the LLS - D_{RR-c}/R_{500} correlation, since the distance from the cluster centre is computed using the cluster X-ray centroid. We note that PSZ2 G069.39+68.05 and PSZ2 G107.10+65.32 are not included in either sub-sample.

Fit Method	cRRs Excluded		cRRs Included	
	B	A	B	A
Y|X	2.24 ± 0.44	−7.92 ± 6.46	2.30 ± 0.45	−8.94 ± 6.59
X|Y	5.45 ± 1.25	−55.00 ± 18.32	6.11 ± 1.35	−64.70 ± 19.93
Bisector	3.22 ± 0.14	−22.37 ± 2.05	3.40 ± 0.15	−25.04 ± 2.13
Orthogonal	5.19 ± 1.20	−51.27 ± 17.60	5.84 ± 1.32	−60.84 ± 19.39

Table 3.2: Radio relic power - cluster mass line of best-fit parameters for different fitting methods. The parameters are calculated separately with and without candidate relics included. We note that PSZ2 G069.39+68.05 and PSZ2 G107.10+65.32 are not included in either sub-sample.

where $Y_m = BX_i + A$ and $X_m = \Sigma_{i=0}^{N} X_i/N$ for each observed X_i.

3.3.2.1 Radio power - cluster mass

Fig. 3.5 shows the 150 MHz radio power of each relic in our sample against the host cluster mass (M_{500}, from *Planck*). The cluster redshift is shown on the colour bar. More massive relic-hosting clusters tend to be found at higher redshifts, due to the *Planck* cluster selection function (see Fig. 3.1). Low-mass clusters in our sample host only low-power RRs. Relics in more massive clusters span a larger range in radio power, but tend to host more powerful RRs than low-mass clusters. To quantify the scatter in the power distribution of RRs residing in high-mass ($> 5.2 \times 10^{14} M_{\odot}$, where $5.2 \times 10^{14} M_{\odot}$ is the median cluster mass in our sample) and low-mass clusters ($\leq 5.2 \times 10^{14} M_{\odot}$), we calculate the coefficient of variance for each sub-sample. The coefficient of variance, defined as $c_v = \sigma/\mu$, where σ is the standard deviation and μ the mean, allows us to compare the scatter in two sub-samples with very different mean values. We find that in the high-mass bin, $c_v = 1.5$ and in the low-mass bin $c_v = 0.9$.

We find a positive correlation between the relic power and cluster mass (p = 0.003, both with, and without, cRRs). Tab. 3.2 shows the best-fit gradient (B) and y-intercept (A) values for the different fitting methods used, for the sample with and without cRRs included.

In Fig. 3.6 we plot the lines of best fit with (cyan dashed line) and without (black solid line) cRRs, from the orthogonal fit. The confidence interval, calculated using Eq. 3.4, is shown by the grey shaded region. We choose to plot the orthogonal-fit line, that is to say the line that minimises the orthogonal distances, as this is the same method used by FdG14 to compute their lines of best fit and enables fair comparison of the two relic studies. Their line of best fit is plotted as a dashed red line. For consistency, we plot the orthogonal-fit line for all other correlations in this paper.

The FdG14 sample selection is considerably different to ours. Their sample is comprised of all dRRs known at the time, in addition to the "elongated" relics of Feretti et al. (2012) (41 individual RRs, of which 30 are part of a dRR pair). The dRR-

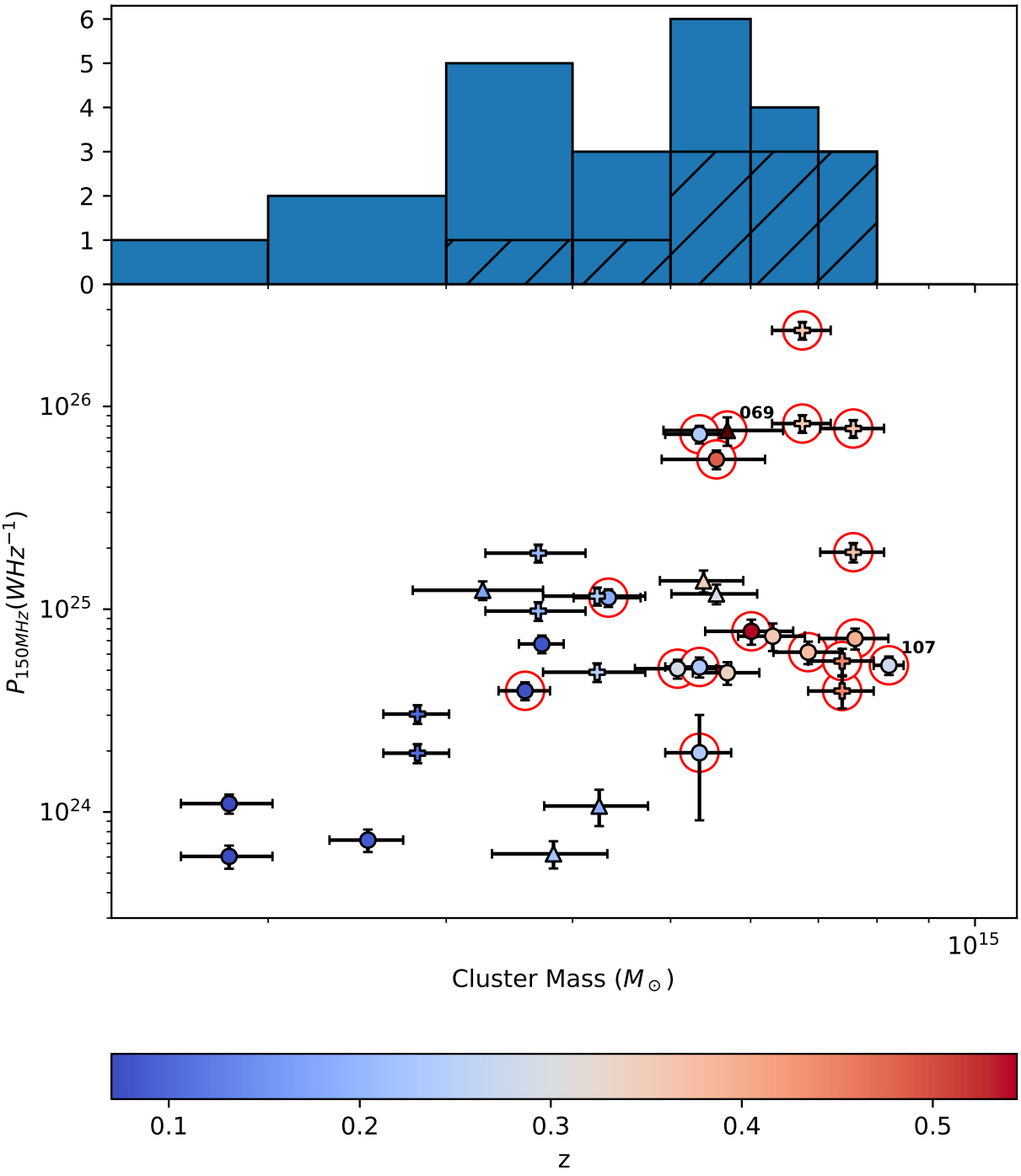

Figure 3.5: Mass distribution of our RR sample. **Top**: As a histogram. The hatched bars show the distribution for only clusters which also host a RH. PSZ2 G069.39+68.05 and PSZ2 G107.10+65.32 are both excluded. **Bottom**: Relic power vs. cluster mass with redshift on the colour bar. Triangles denote candidate relics and plusses those relics which are part of a double relic pair. All other relics are plotted as circles. Red circles surround relics in clusters which also host a RH. PSZ2 G069.39+68.05 and PSZ2 G107.10+65.32 are labelled, with the labels above and right of the data points.

cluster sample of FdG14 contains only two clusters included in our sample, PSZ2 G071.21+28.86 (MACS J1752.0+4440) and PSZ2 G165.46+66.15 (Abell 1240). Additionally, PSZ2 G048.10+57.16 (Abell 2061) is also contained in the sample of Feretti et al. (2012). The cosmology used to calculate distances and luminosities (flat ΛCDM, $H_0 = 71$ km s^{-1} Mpc^{-1}, $\Omega_m = 0.27$) and the frequency (1.4 GHz) are both different to our sample. The cluster masses are also the M_{500} values given by *Planck*, though from the PSZ1 catalogue (Planck Collaboration et al., 2014). The line, and corresponding red data points, were taken at a frequency of 1.4 GHz, so must be converted to 150 MHz, for comparison with our dataset. We do this using two slightly different approaches, shown in the top and bottom sections of Fig. 3.6. The first method (top) is to assume a constant spectral index, $\alpha = -1$, for all relics and scale the full FdG14 dataset and the line of best fit to 150 MHz uniformly. The advantage of using a constant spectral index to scale the FdG14 sample data is that we can also scale the line of best fit by the same factor, thereby allowing direct comparison of the slopes measured at both frequencies. We keep the original cosmology of the FdG14 data, since it was used to derive the line of best fit. Though the cosmology used for our dataset is slightly different to that used for FdG14, the results are almost identical (see Appendix 3.7). Radio relics typically have spectral indices in the range $-1 \lesssim \alpha \lesssim -1.5$. Choosing the flattest spectrum in this range allows the closest comparison of the two samples, since even with this flatter spectral index, the RRs in our sample are, on average, less powerful. In this case, the slope of the line of best fit we obtain does not overlap with that of FdG14 ($B_{orth} = 5.19 \pm 1.20$ vs. $B_{fdg} = 2.83 \pm 0.39$). The second rescaling method (bottom) is to use only the relics with measured spectral index in FdG14 and scale each relic power by its actual spectral index. Since, in this case, the line of best fit reported by FdG14 does not fit the rescaled data, we then recomputed the line of best fit (orthogonal method) ourselves. We obtained best-fit parameters of $B_{fdg} = 5.99 \pm 1.58$ and $A_{fdg} = -62.85 \pm 23.38$ for the rescaled FdG14 data. We do not include any of our sample in the fitting procedure. In this case, the gradient of the line is within the errors of the line calculated for our sample. Qualitatively, we see that our dataset contains more low-mass clusters and more low-power relics in relatively high-mass systems, though it does not contain clusters as massive as in FdG14.

3.3.2.2 Radio power - longest linear size

We did not find a correlation between the power of RRs and their LLS, with cRRs excluded, that is to say we found that the null hypothesis could not be rejected (p = 0.261). However, when we included cRRs, we found that the null hypothesis was rejected (p = 0.029). Tab. 3.3 shows the best-fit gradient (B) and y-intercept (A) values for the different fitting methods used. Since the null hypothesis was only rejected when cRRs were included, we only calculated the best-fit parameters, A and B, for the entire sample. In Fig. 3.7 we plot the power against the relic LLS. The line of best fit (orthogonal fit) is plotted as a dotted cyan line and its corresponding confidence interval the grey shaded region.

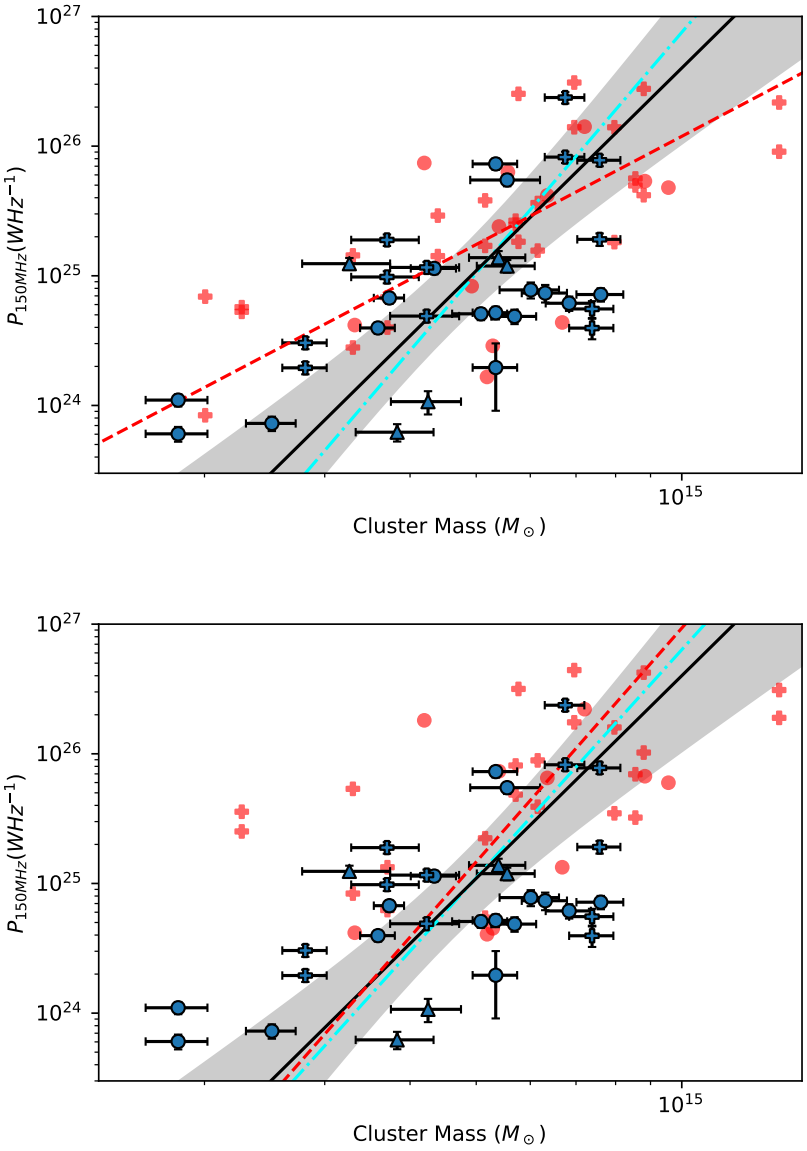

Figure 3.6: Relic power vs. cluster mass with regression lines. Triangles denote candidate relics and plusses those relics which are part of a double relic pair. The black (solid) and cyan (dot-dash) lines are the orthogonal least squares regression lines for the relics in the DR2 sample. Black is if no candidate relics are included, with its corresponding confidence interval shaded, and cyan is if they are. Red points are the RRs from FdG14, with their corresponding regression line in red (orthogonal fit). Both PSZ2 G069.39+68.05 and PSZ2 G107.10+65.32 are excluded, since they are not used to calculate the regression lines. **Top**: FdG14 relic powers and regression line scaled to 150 MHz assuming $\alpha = -1$ for all relics. We note that the cosmologies used to calculate powers are slightly different between this sample data and the FdG14 data. See Fig. 3.16. **Bottom**: FdG14 powers scaled to 150 MHz using the actual spectral indices of each relic. Relics with no spectral information in FdG14 are excluded. The regression line (orthogonal fit) is recomputed on the scaled data.

Fit Method	B	A
Y|X	1.23 ± 0.46	21.19 ± 1.36
X|Y	8.28 ± 4.10	0.112 ± 12.32
Bisector	2.36 ± 0.19	17.82 ± 0.58
Orthogonal	7.60 ± 3.80	2.15 ± 11.42

Table 3.3: Radio relic power - LLS line of best fit parameters for different fitting methods. The values quoted are only for cRRs included, since the null hypothesis was only rejected with their inclusion. PSZ2 G069.39+68.05 and PSZ2 G107.10+65.32 are not included.

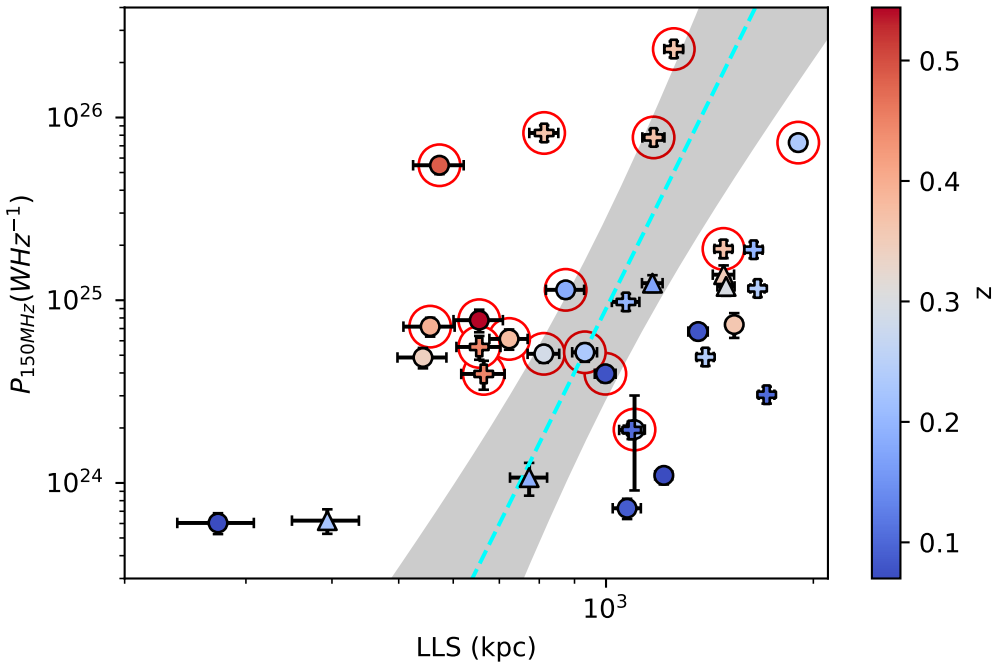

Figure 3.7: Radio relic power vs. LLS. The host cluster redshift is on the colour bar. Triangles denote candidate relics and plusses those relics which are part of a double relic pair. All other relics are plotted as circles. Red circles surround relics in clusters which also host a RH. The dotted cyan line is the regression line (orthogonal fit) for our sample, including cRRs, with its corresponding confidence interval shaded. We note that there is no line of best fit excluding cRRs, since the null hypothesis could not be rejected in this case. Both PSZ2 G069.39+68.05 and PSZ2 G107.10+65.32 are excluded.

Fit Method	LLS - D_{RR-c}		LLS - D_{RR-c}/R_{500}	
	B	A	B	A
Y|X	0.93 ± 0.21	0.14 ± 0.64	0.89 ± 0.21	2.97 ± 0.03
X|Y	1.88 ± 0.38	-2.76 ± 1.16	1.96 ± 0.37	2.95 ± 0.04
Bisector	1.30 ± 0.13	-1.00 ± 0.38	1.29 ± 0.16	2.96 ± 0.03
Orthogonal	1.49 ± 0.27	-1.55 ± 0.82	1.50 ± 0.35	2.96 ± 0.03

Table 3.4: Radio relic LLS - cluster-centre distance and LLS - cluster-centre distance as a fraction of R_{500} line of best fit parameters for different fitting methods. PSZ2 G069.39+68.05 and PSZ2 G107.10+65.32 are not included.

3.3.2.3 Longest linear size - cluster centre distance

We find that there is a positive correlation between the LLS of a relic and its distance from the cluster centre, D_{RR-c}, ($p = 0.002$) and its distance as a fraction of the cluster R_{500} ($p < 0.001$), that is to say larger relics are preferentially found further from the cluster centre. Tab. 3.4 shows the best-fit gradient (B) and y-intercept (A) values for the different fitting methods used. The slopes of both correlations are within errors for all fitting methods. We did not compute the Spearman rank correlation coefficient and perform fitting including cRRs, since we do not have any D_{RR-c} or R_{500} measurements (see Sec. 3.2.2).

In Fig. 3.8 we plot the LLS of our relic sample against their projected distance from the cluster centre and as a fraction of the cluster R_{500}. The solid black line shows the orthogonal fit to our data, with its corresponding 95% confidence interval shown as the grey shaded region. The dashed red line shows the LLS - D_{RR-c} correlation of FdG14 ($B = 1.34 \pm 0.38$ and $A = -1.04 \pm 1.16$) for comparison. Both the gradients and intercepts of the regression lines for each sample are within the errors of each other. There is no LLS - D_{RR-c}/R_{500} correlation in FdG14 against which to compare. The colour bar denotes the median relic width. We see, qualitatively, that larger relics typically have larger widths. It should however be noted that the errors on the width measurements are large, since we assigned the standard deviation of the width distribution measured as the error (see Sec. 3.2.2). For this reason, we did not perform a Spearman rank correlation coefficient test for any relic properties with the downstream width.

3.3.3 Relic - cluster centre distance

Fig. 3.9 (top) shows the distribution of the projected RR-cluster centre distances, with a dashed (red) reference line at 800 kpc. The bottom panel shows the distribution as a fraction of R_{500}. The hatched bars show the distribution only for RH-hosting clusters. The solid and dashed black lines correspond to the median distances for all relics with D_{RR-c} measurements (except PSZ2 G107.10+65.32) and just those which also host a RH, respectively. The medians are very similar, in both cases and, in general, the distances of relics in RH-hosting clusters follow the distribution of the full sample relatively well. For simplicity, we exclude PSZ2 G107.10+65.32 from both plots entirely. PSZ2 G069.39+68.05 is automat-

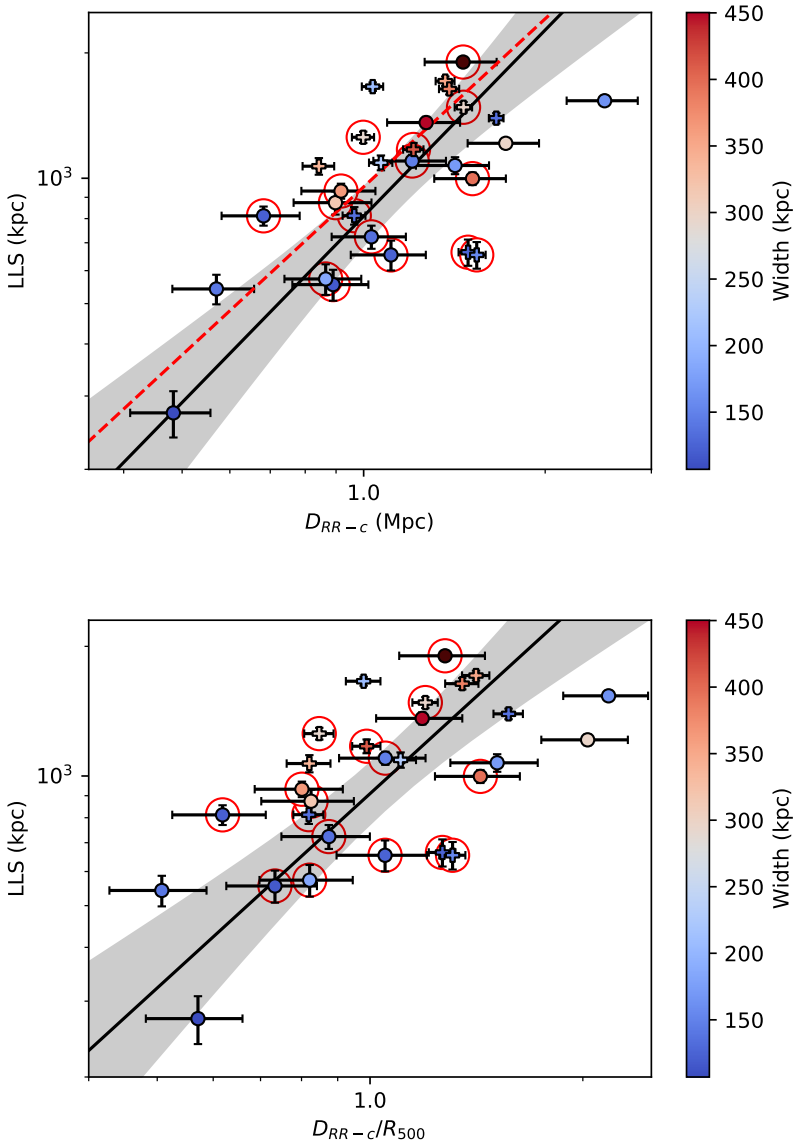

Figure 3.8: Radio relic LLS as a function of its projected distance to the cluster centre. **Top:** LLS vs. cluster centre distance. The relic width is plotted on the colour bar. Plusses denote relics which are part of a double relic pair. All other relics are plotted as circles. Red circles surround relics in clusters which also host a RH. PSZ2 G107.10+65.32 is excluded. The black line is the regression line (orthogonal fit) for our sample, with its corresponding confidence interval shaded. The dashed red line is the regression line from FdG14. We note that there are no candidates, since the cluster centre is found from X-ray observations. **Bottom:** The same for the cluster centre distance as a fraction of the cluster R_{500}. There is no corresponding FdG14 correlation against which to compare.

ically excluded, since it is a cRR-hosting cluster, and therefore has no D_{RR-c} or R_{500} measurements. Excluding PSZ2 G107.10+65.32, $25/28 = 89 \pm 19\%$ of the relics in our sample are > 800 kpc from the cluster centre. For the sub-sample of RR-hosting clusters which also host a RH, this is $14/15 = 93 \pm 19\%$. One relic, in PSZ2 G091.79-27.00, is located 2.5 Mpc from its cluster centre, which is much further than for the other relics in our sample. $20/28 = 71 \pm 17\%$ of relics lie within the range $0.75 \leq D_{RR-c}/R_{500} \leq 1.5$. For RH-clusters in our sample, this becomes $14/15 = 93 \pm 19\%$. The relics PSZ2 G089.52+62.34 N2 and PSZ2 G091.79-27.00 are located $\gtrsim 2R_{500}$ from their cluster centres.

3.4 Discussion

3.4.1 Occurrence of RRs

Radio relics are relatively uncommon phenomena. Previous studies have found that $\sim 5\%$ of galaxy clusters host a RR (at 610/235 MHz, Kale et al., 2015). To calculate the RR occurrence at 150 MHz, we considered only clusters above the *Planck* 50% completeness line, except PSZ2 G107.10+65.32, since we do not know the mass of the relic-hosting, S subcluster (see Sec. 3.2.1). 273 of the 309 clusters in the full LoTSS DR2 - PSZ2 sample have adequate image quality to assess the presence of diffuse radio emission (see Botteon et al., 2022, for further details). Of these, 194 lie above the *Planck* 50% completeness line (excluding PSZ2 G107.10+65.32). In our sample, $19/194 = 10 \pm 6\%$ of galaxy clusters host at least one RR. If we also include all cRRs, we get that $24/194 = 12 \pm 7\%$ of clusters host at least one RR. We note that this is a soft lower limit at the sensitivity of LoTSS DR2, since there may be relics which are too faint to be detected with our observations. There are 42 clusters in the LoTSS DR2 - PSZ2 sample which contain diffuse radio emission of uncertain origin (classified as U in Botteon et al., 2022), but no RR or cRR classification. 33 of these lie above the *Planck* 50% completeness line. It is possible that some of these clusters also host RRs. However, it is unlikely that this would change our results meaningfully, as, from visual inspection, a significant fraction of these appear to have a morphology more similar to RHs.

We assessed the effect of cluster mass on RR occurrence by splitting our sample into two mass bins: high ($> 5.2 \times 10^{14} M_{\odot}$) and low ($\leq 5.2 \times 10^{14} M_{\odot}$), where $5.2 \times 10^{14} M_{\odot}$ is the median mass of our sample. We find that $10/89 = 11 \pm 7\%$ of high-mass clusters host at least one RR, which becomes $13/89 = 15 \pm 8\%$ when cRRs are included. For low-mass clusters, these occurrences are $9/105 = 9 \pm 6\%$ and $12/105 = 11 \pm 7\%$. The occurrences at high and low mass are within errors, suggesting that there is no dependence of the occurrence on the cluster mass, unlike for RHs (e.g. Cassano & Brunetti, 2005; Cuciti et al., 2015, 2021).

Radio relics typically have steep spectra ($-1.0 \gtrsim \alpha \gtrsim -1.5$, e.g. FdG14, Feretti et al., 2012). The increase in relic occurrence at LOFAR frequencies, as compared to higher frequencies, is therefore unsurprising. Nuza et al. (2012) used the MARENOSTRUM UNIVERSE cosmological simulation to estimate the expected number of RRs that LOFAR

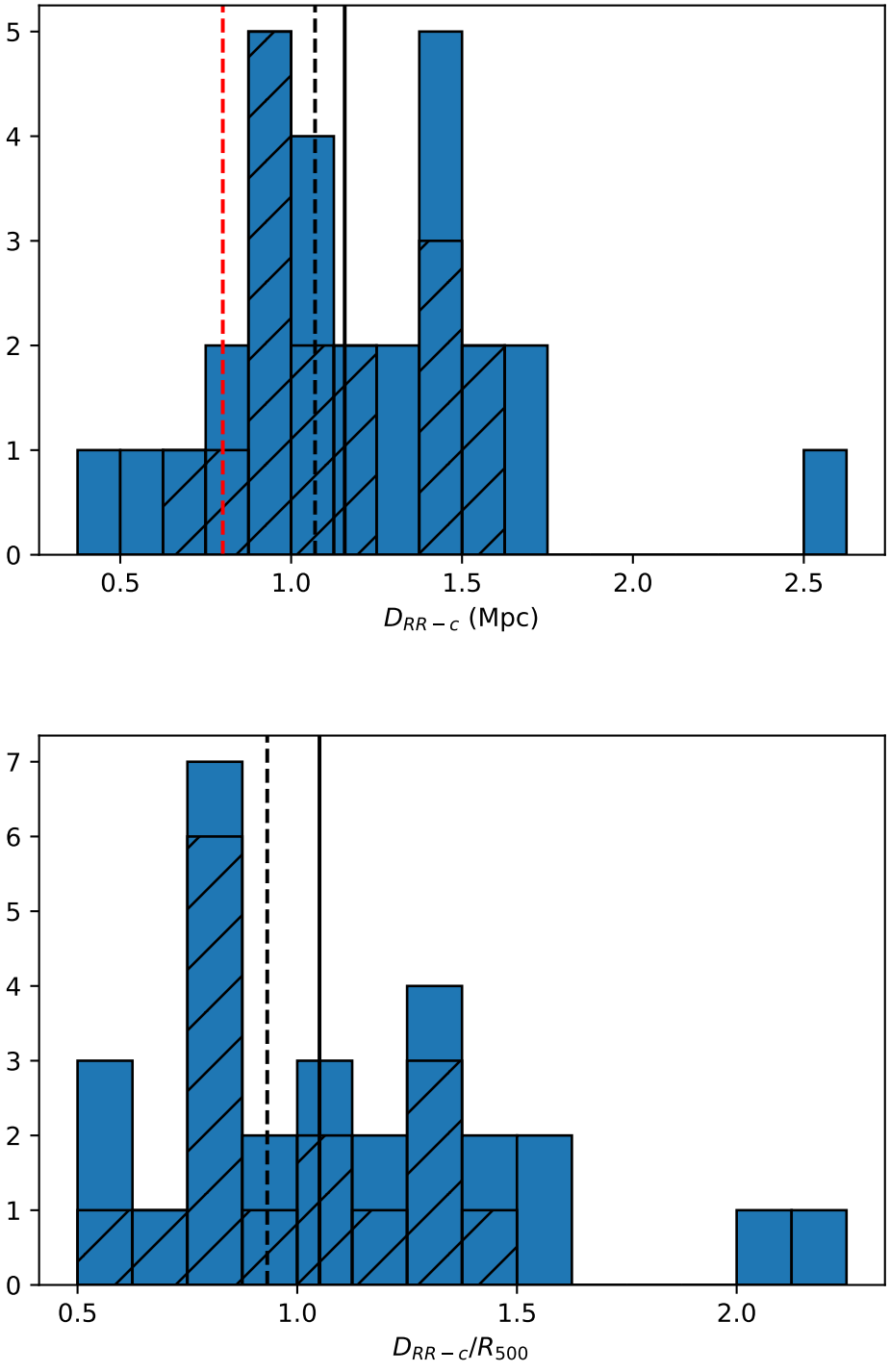

Figure 3.9: Distribution of projected RR distances from their host-cluster centres. **Top**: Histogram of the RR - cluster centre distances, D_{RR-c}. The red dashed line is at 800 kpc. **Bottom**: Histogram of the RR - cluster centre distances as a fraction of the cluster R_{500}. The hatched bars in both plots show the distribution for only relics in RH-hosting clusters. The solid and dashed black lines correspond to the median distances for all relics and just those which also host a RH, respectively. We note that PSZ2 G107.10+65.32 is excluded for both histograms and the median calculations.

would discover. By normalising the number of relics above a certain radio flux against the number of RRs observed at that point at 1.4 GHz, they predicted that LOFAR would discover $\sim$ 2500 new relics, in $\sim$ 50% of galaxy clusters. Even including cRRs and the relics in clusters below the *Planck* 50% completeness line, our sample contains only 35 RRs. If we extrapolate the number of relics detected in LoTSS DR2 to the entire northern sky, that is the area that will be covered upon the completion of LoTSS, we expect to observe 109 ± 58 RRs in the 835 PSZ2 detections that lie above 0°declination (see Botteon et al., 2022).

The absolute number of RRs observed is dependent on the underlying sample of galaxy clusters. The number of RRs predicted by Nuza et al. (2012) was not calculated using PSZ2 galaxy clusters, but rather on the X-ray NORAS+REFLEX sample. Additionally, Nuza et al. (2012) predicted that $>$ 50% of the relics detected by LOFAR would reside in clusters with $z > 0.5$. In the entire LoTSS DR2 - PSZ2 sample, only 46 clusters lie at such high redshift, and, of those, only 2 (including PSZ2 G069.39+68.05) host a RR. However, whilst not a complete study of all non-PSZ2 clusters covered by the LoTSS DR2 area, the results of Hoang et al. (2022) do not suggest that we are missing a large number of RRs because of our restriction to only PSZ2 clusters. Also, the fraction of clusters predicted to host RRs detectable by LOFAR is much greater than in our sample ($\sim$ 50% vs. 10%). Therefore, unless the fraction of relic-hosting clusters varies significantly between the PSZ2 and NORAS+REFLEX samples, the number of relics able to be detected by LOFAR is significantly less than predicted by simulations.

One key assumption that governs the number of RRs observable is the efficiency of CRe acceleration by the shock. If the real acceleration efficiency is much lower than that assumed in simulations, the number of observable RRs will be overestimated, since the relic power is dependent on the efficiency ($\mathrm{d}P(\nu)/\mathrm{d}\nu \propto \xi_\mathrm{e}$, where ξ_e is the fraction of kinetic energy dissipated at the shock, Hoeft & Brüggen, 2007). Using the same cosmological simulation as Nuza et al. (2012), Araya-Melo et al. (2012) found that an acceleration efficiency of only $\xi_\mathrm{e} = 0.0005$, that is to say a factor of ten lower than that assumed by Nuza et al. (2012), was sufficient to reproduce the NRAO VLA Sky Survey (NVSS) RR luminosity function.

An alternative cause of the discrepancy between simulations and the observed number of RRs could be the assumption of shock acceleration of electrons to relativistic energies from the thermal pool (standard DSA). Numerous studies have suggested that re-acceleration of a pre-existing population of relativistic electrons is required to produce the observed brightness of RRs (e.g. Kang & Ryu, 2011; Kang et al., 2012; Botteon et al., 2020a). Such a scenario relies on the existence of populations of mildly energetic electrons in the ICM available to be re-accelerated. The tails of radio galaxies could provide such a population, as has been suggested for Abell 3411-3412 (van Weeren et al., 2017). Another potential source is fossil plasma energised by ICM motions (e.g. de Gasperin et al., 2017; Mandal et al., 2020). Their ultra-steep spectra make such sources challenging to observe, so it is unclear how ubiquitous such populations are. If re-acceleration of relativistic electrons, instead of acceleration from the thermal pool, is required in some or all cases, many fewer RRs will be observed than predicted by simulations assuming standard DSA. This is because, in this scenario, only those shocks which cross a population of relativistic

electrons will produce a RR.

3.4.2 Radio power of relics

In their statistical study of RRs, FdG14 found a positive correlation between the radio power of relics at 1.4 GHz and the mass of the host cluster, similar to that found for giant RHs (e.g. Basu, 2012; Cassano et al., 2013; Cuciti et al., 2021). The physical explanation is that RRs are driven by shock waves caused by galaxy cluster mergers, for which the energy budget is set by the total mass of the merging clusters. The total energy released by a merger between two clusters of mass M and virial radius $R_{vir} \propto M^{1/3}$ is $E \propto M^2/R_{vir}$. Assuming that the kinetic energy dissipated at the shock is a fixed fraction of the total energy, and that it scales with the RR power, P, the power should scale like $P \propto E/t_{cross}$, where t_{cross} is the sound crossing time of the cluster and is related to the sound speed at the shock through $t_{cross} = R_{vir}/c_s$. X-ray studies show that cluster temperature, T, scales with $M^{2/3}$ (e.g. Pratt et al., 2009; Lovisari et al., 2020) and, since it also scales with c_s^2, we would expect the radio power of relics to be related to the cluster mass by $P \propto M^{5/3}$.

For the first time, we show that the P-M correlation extends to frequencies below 200 MHz (see Sec. 3.3.2.1). However, we find that the relation is much steeper than that predicted by our simple estimate based on the total energy budget of the infalling mass, independent of the fitting method used (see Tab. 3.2). This could suggest that the assumption that a constant fraction of the total energy is dissipated at the shocks does not hold. Alternatively, it could suggest a dependence of the shock magnetic field or particle acceleration efficiency on the cluster mass. Additionally, observational bias may contribute to the measured slope of the P-M relation. We assess this effect in more detail in Sec. 3.4.2.1.

We also find a different mass dependency than that found by FdG14, who found that $P_{1.4\mathrm{GHz}} \propto M^{2.8\pm0.4}$, whereas we find $P_{150\mathrm{MHz}} \propto M^{5.2\pm1.2}$ using the same fitting procedure (orthogonal least squares). Fig. 3.6 (top) shows the two correlations plotted on top of each other, with all data points and the correlation scaled to 150 MHz using a constant spectral index of $\alpha = -1$. Radio relics typically have spectral indices in the range $-1.0 > \alpha > -1.5$ (e.g. FdG14, Feretti et al., 2012). Even using the flattest spectrum within this range, we see that the majority of the relics in our sample lie below the correlation of FdG14. This is unsurprising, since RRs have relatively steep spectra. This, combined with the increased sensitivity of LOFAR and low operating frequencies, makes detection of low-power RRs easier. For a large number of relics in the FdG14 sample, spectral information is available. We therefore took all relics for which this is the case, calculated the expected power at 150 MHz and recomputed the line of best fit on our re-scaled data (orthogonal fit). We note that this approach assumes no spectral curvature. The presence of which would cause the radio power at 150 MHz to be overestimated. The most detailed study of the integrated spectrum of a relic to-date however shows that the spectrum is straight (e.g. Rajpurohit et al., 2020). The re-scaled data, and its corresponding line of best fit, are plotted in Fig. 3.6 (bottom), along with the same line of best fit for the LoTSS DR2 - PSZ2 sample as before. We find that the lines of best fit are now remarkably similar, despite the greater number of low-power relics in our sample. These results suggest that taking the spectral

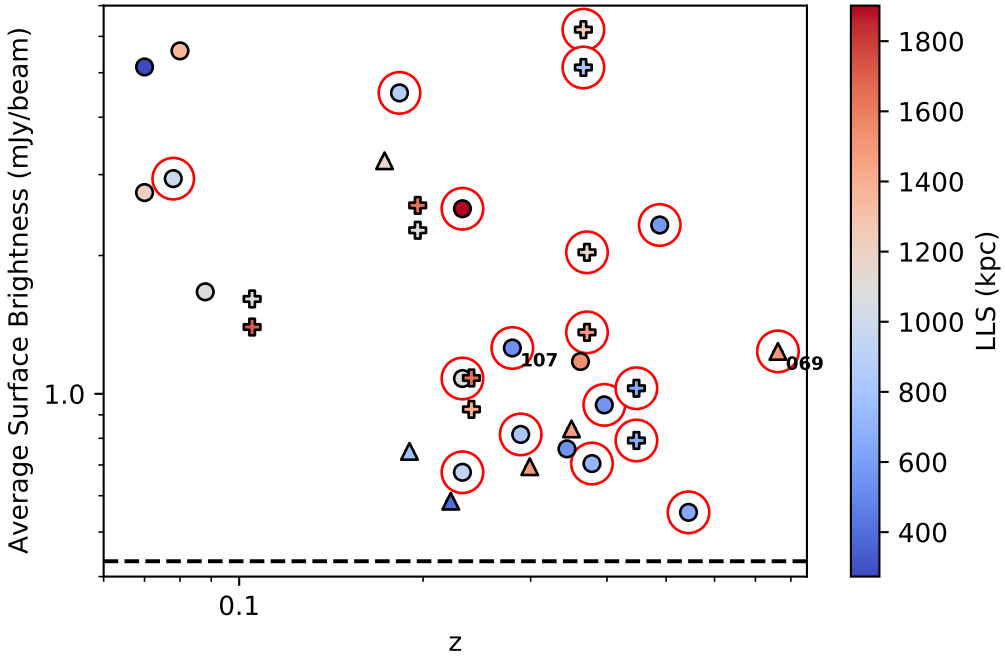

Figure 3.10: Average relic surface brightness vs. redshift. The colour of the points shows the relic LLS. Triangles denote candidate relics and plusses those relics which are part of a double relic pair. All other relics are plotted as circles. Red circles surround relics in clusters which also host a RH. PSZ2 G069.39+68.05 and PSZ2 G107.10+65.32 are labelled, with the labels below and right of the data points. The dotted black line is at $2\sigma_{50\mathrm{kpc}}$, where $\sigma_{50\mathrm{kpc}} = 0.216$ mJybeam^{-1} is the average rms noise of the 50 kpc-tapered images in our sample.

index of each relic into account can entirely compensate for the discrepancy between the mass-dependence of each line of best fit.

3.4.2.1 Low-power RRs

If there exists a population of lower-power relics, especially at high redshifts, where most massive clusters are found, we may be unable to detect them. The power-mass correlation we measure would, in this case, be biased towards higher-power relics, since we only observe low-power RRs in nearby, low-mass clusters. Unlike for RHs, we do not have a robust method for determining upper limits for RRs in clusters defined as non-RR-hosting (e.g. Bonafede et al., 2017; Bruno et al., 2023). Instead, we must rely on simpler estimates from the typical noise of our observations. Fig. 3.10 shows the surface brightness averaged across each relic as a function of cluster redshift. The black dashed line shows the approximate detection limit of our observations, given by two times the average rms noise of the 50 kpc-tapered images in our sample ($\sigma_{50\mathrm{kpc}}$). Many of the higher-redshift relics lie just above the estimated detection limit.

We also assess this bias by estimating the radio power required for a RR to be observable, as a function of redshift. To do this we calculated the power of a box with dimensions of the minimum ($\sim$ 300 kpc $\times$ 100 kpc) relic LLS and widths of our sample and average surface brightness equal to $2\sigma_{50\mathrm{kpc}}$ (as above), for a 50 kpc beam. This is shown as a red dot-dashed line in Fig. 3.11. Since we kept the beam at a fixed physical size, independent of redshift, the relic flux is constant. The least powerful, high-z relics in our sample lie close to the 300 kpc $\times$ 100 kpc line. Since the smallest relic (PSZ2 G089.52+62.34 N1, both smallest LLS and width) is considerably smaller than the other relics in our sample (see Fig. 3.8), we also calculated the same sensitivity limit for the average relic. The box dimensions were, in this case, the median LLS and width values of our sample ($\sim$ 1100 kpc and 200 kpc). This is plotted as a dashed black line in Fig. 3.11. A few relics lie between the two sensitivity lines, but most lie above the median line. As in FdG14, we find that the faintest relics we observe are at the detection limit of our observations. This implies that the missing low-power relic population might just be a selection effect.

Additionally, the least powerful relics are found only in nearby clusters. Of the 7 relics with radio powers $< 3\times10^{24}$ WHz^{-1} (PSZ2 G080.16+57.65, PSZ2 G086.58+73.11, PSZ2 G089.52+62.34 N2, PSZ2 G089.52+62.34 N1, PSZ2 G099.48+55.60 S, PSZ2 G144.99-24.64, PSZ2 G166.62+42.13 E), all are located at z < 0.25. This is unsurprising, since, for a given power, the flux observed decreases with distance. However, since in our sample more massive clusters are generally located at higher redshifts (see Fig. 3.1), this effectively places an approximate lower limit on the power detectable with LOFAR at a given cluster mass. If we take the approximate sensitivity limit calculated for an average relic in our sample (Fig. 3.11, black dashed line), we would expect that a relic with radio power 3×10^{24} WHz^{-1} would be too faint to be observable in LoTSS DR2 if it were located $z \gtrsim 0.27$. Comparing the masses of the clusters in our sample located above and below this redshift, we find that the median mass above (6.2×10^{14} $M_\odot$, from 14 clusters) is much greater than below (3.7×10^{14} $M_\odot$, from 12 clusters). This implies that if such a population of low-power RRs also exists at high redshift, and therefore mass, we would be unable to detect them.

Studies focussing on the properties of large samples of simulated RRs (e.g. Nuza et al., 2017; Brüggen & Vazza, 2020) suggest that there is a large number of low-power RRs, especially in low-mass clusters. The low-mass systems in our sample are among the least massive clusters known to host RRs, with only the relics in Abell 168 being hosted by a lower-mass cluster ($M_{500} = 1.2 \times 10^{14}$ $M_\odot$ from the X-ray mass - luminosity correlation, Piffaretti et al., 2011; Dwarakanath et al., 2018) than PSZ2 G089.52+62.34 ($M_{500} = 1.8 \times 10^{14}$ $M_\odot$) in our sample. LOFAR has allowed for the discovery of relics in low-mass clusters, such as in PSZ2 G145.92-12.53 ($M_{500} = 1.9 \times 10^{14}$ $M_\odot$ from PSZ2, Botteon et al., 2021). In fact, of the 11 clusters $< 5 \times 10^{14}$ $M_\odot$ in our sample, the RRs in 9 of them were discovered for the first time with LOFAR, or in combination with another instrument. The low-mass end of our sample is nonetheless sparsely populated. Our results suggest that we could well be missing a number of low-power RRs, especially in low-mass clusters. This would appear to weaken the finding of a correlation between cluster mass and the power of a RR and may suggest that, in contrast to RHs, the merging mass is not a direct driver of the relic power, as suggested by Nuza et al. (2017). However, it should be noted that the discrepancy between observed and simulated relic counts

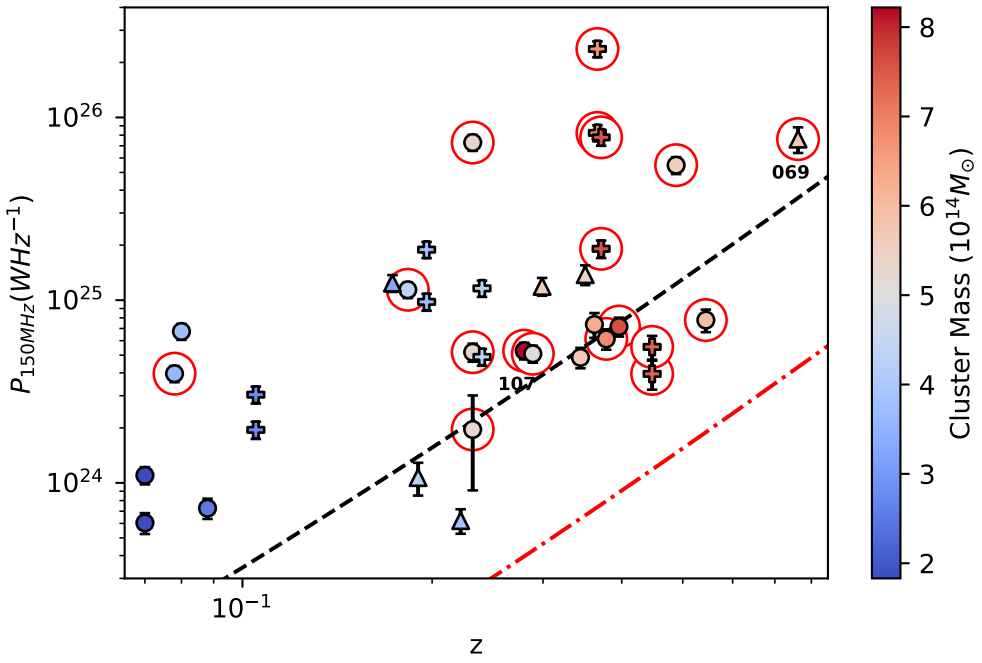

Figure 3.11: Relic power vs. cluster redshift. The colour of the points shows the cluster mass. Plusses denote relics which are part of a double relic pair. All other relics are plotted as circles. Red circles surround relics in clusters which also host a RH. The black (dashed) and red (dot-dashed) lines show the estimated detection limit for the median ($\sim$ 1100kpc $\times$ 200kpc) and minimum ($\sim$ 300kpc $\times$ 100kpc) relic LLSs and widths of our sample, respectively. PSZ2 G069.39+68.05 and PSZ2 G107.10+65.32 are labelled, with the labels directly below the data points.

(see Sec. 3.4.1) cast doubt on the existence of a large population of undetected relics and suggest that cosmological simulations are unable to fully produce the observed RR population properties. Indeed, this would support the idea that the cluster mass sets an approximate upper limit on the power of a relic, but additional factors drive the differences in observed brightness. For example, the particle acceleration efficiency is a function of the underlying shock Mach number (Hoeft & Brüggen, 2007) and could therefore drive differences in RR power. Additionally, if relics are produced by re-acceleration of mildly relativistic fossil electrons, the properties of the electron population would also affect the power of the relic.

3.4.2.2 On the scatter in the power-mass correlation.

Cuciti et al. (2021) found that the scatter in the $P_{150MHz} - M_{500}$ for giant RHs can be, at least in part, explained by the morphological cluster disturbance. Radio halos that lie above the correlation tend to be found in more disturbed clusters. We investigate whether this can also explain the scatter for the $P_{150\mathrm{MHz}} - M_{500}$ correlation for relics. We calculated the error in the distance from the correlation with bootstrapping methods. We assigned the cluster mass and radio power of each relic a random number drawn from a Gaussian distribution with mean of the measured value and standard deviation the corresponding errors. We then re-fitted the data with an orthogonal fit and measured the distance of each point from the new correlation. This was repeated 1000 times and we use the standard deviation of the distance measurements as the random error. The total error is from a combination of this error and the power error of each relic.

In Fig. 3.12 (top) we plot the logarithmic distance, along the $P_{150\mathrm{MHz}}$ axis, of a RR from the $P_{150\mathrm{MHz}} - M_{500}$ correlation for all relics (orthogonal fit) against the cluster disturbance (see Sec. 3.3.1). As the lines of best fit including, and excluding, cRRs (see Tab. 3.2) are so similar, we use the line of best fit including cRRs. We do not find a correlation between the disturbance and the distance from the correlation. In Fig. 3.12 (bottom) we plot the distance from the same correlation against the relic LLS. Smaller relics tend to lie below the $P_{150\mathrm{MHz}} - M_{500}$ correlation and larger relics above. This finding is expected, since for a given surface brightness, a larger relic should be more powerful. The correlation found between the RR power and the LLS supports this (see Sec. 3.3.2.2), although this correlation is only found when cRRs are included. The smallest relic (PSZ2 G089.52+62.34 N1) is an outlier, in that it is a very small relic (~300 kpc) which lies well above the correlation. This relic is connected, at least in projection, to an AGN (see van Weeren et al., 2021, for more details), which could have had an effect on the relic's brightness. Such an effect has been observed in other relics, such as PSZ2 G096.88+24.18 (Jones et al., 2021). However, PSZ2 G089.52+62.34 is also a low-mass cluster, where we observe very few relics and therefore the correlation is poorly constrained.

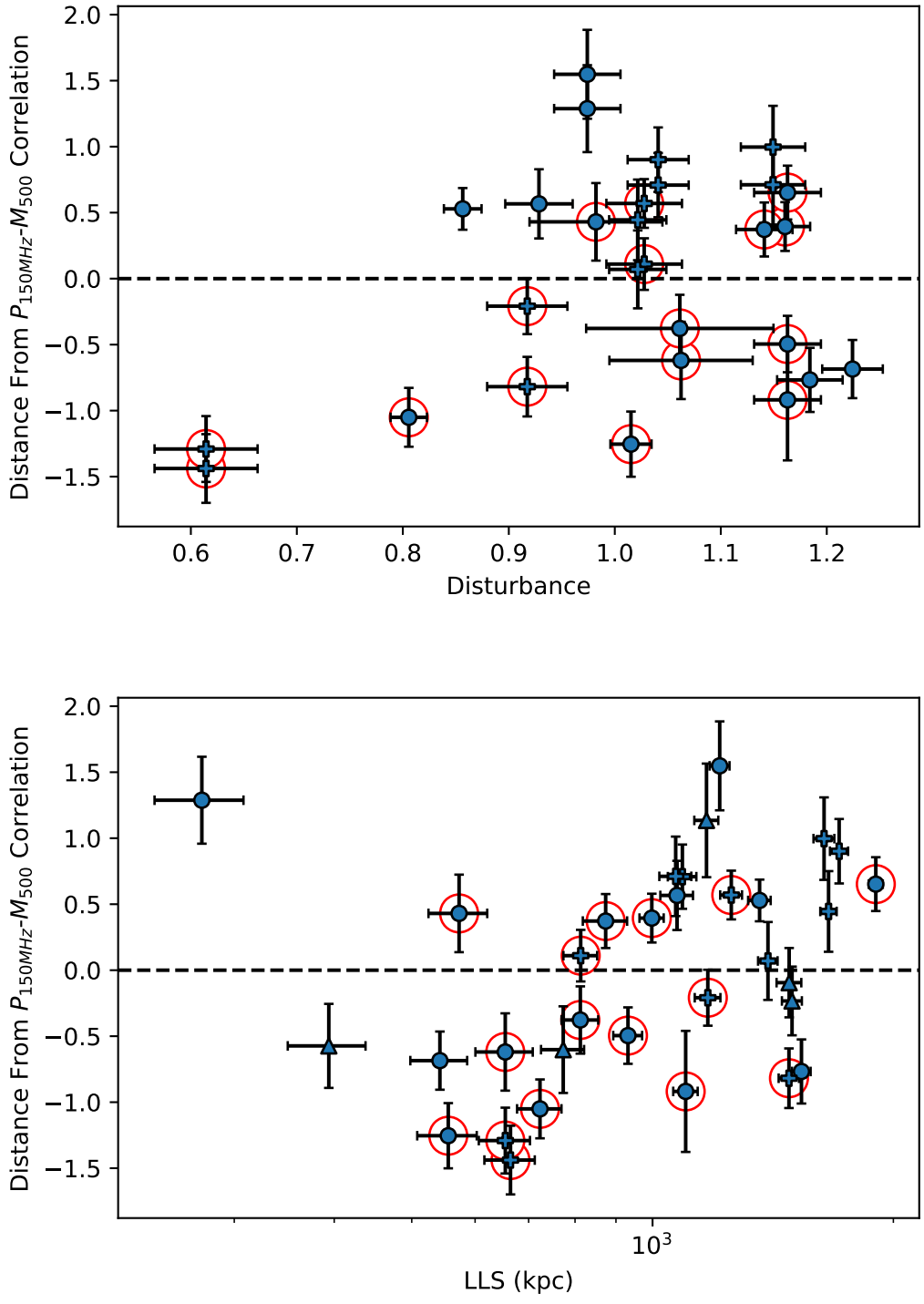

Figure 3.12: Logarithmic distance from P-M correlation (along $P_{150\mathrm{MHz}}$ axis, Fig. 3.6) vs. LLS (top), disturbance (bottom). The distance is calculated from the orthogonal fit on all relics (except PSZ2 G069.39+68.05, PSZ2 G107.10+65.32; see Tab. 3.2). PSZ2 G069.39+68.05, PSZ2 G107.10+65.32 are excluded from the plots.

3.4.3 Downstream relic width

The downstream width of a RR is set by the radiative lifetime of the CRes producing the relic. In the case of DSA, electrons at a shock front in the ICM are (re-)accelerated to relativistic energies. However, as the shock propagates through the ICM, in the absence of another acceleration mechanism, the electrons left behind the shock lose energy through inverse Compton (IC) and synchrotron emission until they become too faint to observe. For some relics, there is evidence that the downstream width is too large to be fully explained in this scenario. By estimating the expected width of a relic, given synchrotron and IC losses, Kang et al. (2017) found a discrepancy of a factor of ~ 2 in the Toothbrush relic at 610 MHz. The effect is particularly pronounced at low radio frequencies however. Performing similar estimations, de Gasperin et al. (2020) found that the width of the relic was ~ 4 times larger than predicted at 58 MHz. A similar discrepancy was found for the Sausage relic (Kang, 2016) and in Abell 3667 (de Gasperin et al., 2022).

For the first time, we systematically measure the downstream widths of relics, by calculating the width at many points along the relic to produce a distribution of widths (see Sec. 3.2.2). Fig. 3.13 shows the medians of the measured relic width distributions as a function of redshift. The error bars correspond to the standard deviation of the width distributions. To compare our width measurements against theoretical expectations, we use Kang et al. (2017) (Eq. 1), who estimated the characteristic downstream width behind a spherical shock at a given frequency, due to IC and synchrotron losses. The width is then given by

$$\Delta l_\nu \approx 120 \text{ kpc} \left(\frac{u_{down}}{10^3 \text{ kms}^{-1}} \right) \cdot Q \cdot \left[\frac{\nu_{obs}(1+\text{z})}{0.61 \text{ GHz}} \right]^{\frac{1}{2}}, \tag{3.5}$$

where u_{down} is the downstream shock speed, ν_{obs} is the observing frequency, and Q depends on the downstream magnetic field, B_{down}, as

$$Q \equiv \left[\frac{(5\ \mu\text{G})^2}{B_{down}^2 + B_{CMB}^2} \right] \left(\frac{B_{down}}{5\ \mu\text{G}} \right)^{\frac{1}{2}}, \tag{3.6}$$

where $B_{CMB} = 3.24(1+z)^2\ \mu$G is the equivalent magnetic field strength of the cosmic microwave background (CMB). Since we do not have information on the downstream magnetic field strength, we assumed the magnetic field strength which minimises radiative losses, that is $B_{down} = B_{CMB}/\sqrt{3}$. The theoretical widths we calculated therefore correspond to the *maximum* expected width. The expected width is also strongly dependent on the downstream flow speed, u_{down}, which depends on the shock Mach number, $\mathcal{M}$, and upstream sound speed, $c_{s,up}$. $c_{s,up}$ is then related to the downstream sound speed, $c_{s,down}$, by $c_{s,down}/c_{s,up} = \sqrt{\frac{(5\mathcal{M}^2-1)(\mathcal{M}^2+3)}{16\mathcal{M}^2}}$. We estimated u_{down}, using $u_{down} = c_{s,up}\frac{\mathcal{M}^2+3}{4\mathcal{M}}$, and $c_{s,down} \approx 1480 \text{ kms}^{-1} \left(\frac{T_d}{10^8 \text{K}}\right)^{1/2}$. By assuming a number of reasonable $\mathcal{M}$, and downstream temperatures, T_d, we could therefore estimate the maximum expected relic width. The resulting expected widths are plotted in Fig. 3.13. The maximum downstream speed reached with these parameters is $\sim 10^3$ kms^{-1}. Only PSZ2 G089.52+62.34 N1, the smallest relic in our sample, lies completely below the uppermost line. The widest relic

(PSZ2 G166.62+42.13 W, median width $\sim$ 700 kpc) would require $u_{down} \sim 5000$ kms^{-1} to agree with the prediction.

Clearly, the width of RRs is greater than expectations in almost all cases, for our sample. In most cases, even optimistic assumptions of the downstream temperature and Mach number are insufficient to explain the median values of our calculated width distributions. One possible solution to this is that downstream turbulence further accelerates the relic-producing CRes, extending their radiative lifetime (e.g. Fujita et al., 2016). Evidence of turbulence in the downstream regions of relics has been discovered in some clusters. For example, Kale et al. (2012) and Jones et al. (2021) found patchy polarised emission in the Abell 3376 and PSZ2 G096.88+24.18 relics, respectively, which they each attributed to turbulence. Di Gennaro et al. (2021) performed an extensive analysis of the polarisation structure in the Sausage relic using RM-synthesis. They found that the observed depolarisation could be explained by a turbulent magnetic field strength of $B_{turb} \sim 5.6$ μG. Simulations of the Sausage and Toothbrush relics, by Kang (2016) and Kang et al. (2017) respectively, found that they could be explained by shock re-acceleration of fossil electrons with post-shock turbulence. It is not clear if this can explain the systematic offset between the expected and observed relic widths, since the downstream region of only a few relics show indications of turbulence. Another possibility is that, in general, the shock is broken and complex in shape, so multiple shocks can travel one after the other, artificially expanding the post-shock region. This is a proposed scenario to explain the filaments in Abell 3667 (de Gasperin et al., 2022), and many other RRs show a complex, filamentary sub-structure (e.g. George et al., 2015; Di Gennaro et al., 2018; Rajpurohit et al., 2022).

3.4.4 Radio halos in relic-hosting clusters

The connection between galaxy cluster mergers and both RRs and giant RHs is well-established. It is however unclear why, in addition to clusters which host both RR(s) and RH(s), there are numerous clusters which only host one or the other. In a study of dRR-hosting clusters, Bonafede et al. (2017) investigated the differences between clusters with and without RHs. In their work, they found no relation between the merger mass ratio and the presence of RHs. However, they did find a possible relation with the time since merger, though the statistics were too low to be conclusive.

In our sample, only 6 clusters host dRRs and, of these, 3 also host a giant RH. The statistics are therefore much too low to limit our analysis to only dRRs. If the difference between RH-hosting and RR-hosting clusters is evolutionary, that is to say that they are produced at different times over the course of a merger, we might expect that there is a characteristic time since merger when RHs are produced. MHD simulations of two clusters by Donnert et al. (2013) support this scenario. They found that the power of the RHs produced evolved throughout the merger from radio-quiet during the infall phase, to radio-loud as turbulence is driven throughout much of the cluster volume and finally decays to become radio-quiet again. Using the distance between a relic and the cluster centre as a proxy for the time since merger, we can investigate such an effect. In Fig. 3.9 we plot histograms of the distance of the relics to the cluster centre and the distance as a fraction of the cluster R_{500}. The black, hatched bars show those relics which are in RH-hosting

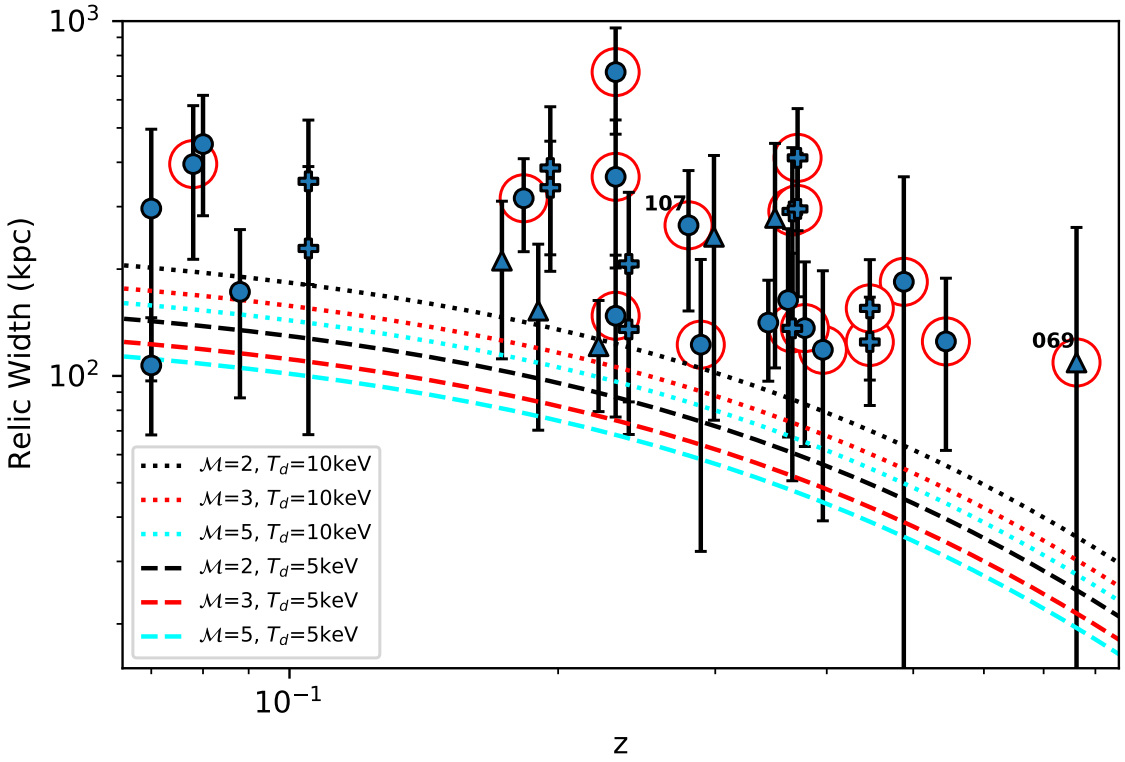

Figure 3.13: Median relic width vs. redshift. The error bars correspond to the standard deviation of the relic widths measured. Triangles denote candidate relics and plusses those relics which are part of a double relic pair. All other relics are plotted as circles. Red circles surround relics in clusters which also host a RH. The dashed and dotted lines show the largest expected relic width from Kang et al. (2017) for different shock properties. PSZ2 G069.39+68.05 and PSZ2 G107.10+65.32 are labelled, with the labels above and left of the data points.

clusters. There is no clear distinction in the relic distance, nor as a fraction of cluster R_{500}, between clusters with and without RHs. The distribution of relics in RH-hosting clusters is similar to those without, though at the most extreme distances none of the clusters also host a RH. The statistics are low, but this is similar to the results of Bonafede et al. (2017), where clusters with a giant RH occupied the centre of the time-since-merger distribution. They suggested that, in early mergers, turbulence has not had enough time to cascade down to scales at which particles can be (re-)accelerated and, in late mergers, the CRes producing RHs may have already become too faint to observe, due to IC and synchrotron losses. Relics on the other hand, due to continued shock acceleration, would be able to stay visible for longer. Though this assumes that the shock passage lasts longer than the timescale of turbulence able to produce RHs. In their study on the observed fraction of RHs in merging galaxy clusters, Cassano et al. (2016) found that the absence of RHs in some merging clusters could be explained by an RH-lifetime of $\sim (0.7 - 0.8)\tau_{merger}$, where τ_{merger} is the merger timescale. If RRs have longer lifetimes, this may go some way to explaining the difference between RH-hosting and RR-hosting clusters, though this would not explain why many clusters are observed with RHs but not RRs. Cassano et al. (2016) also found evidence that RHs may instead be produced only in larger mass ratio merger events. If RR generation has a different dependence on the mass ratio, this could also contribute to the discrepancy we observe. Unfortunately, we do not have data on the merging mass ratio for our sample and are therefore unable to investigate the effect.

Another possibility is that the difference between the two populations is due to the merging state. Turbulence is injected into the ICM directly by the merger. Minor mergers may therefore be unable to inject enough turbulence into the ICM to produce visible RHs (Cassano & Brunetti, 2005). If this were the case, we might expect that clusters with both relics and halos are more morphologically disturbed than those with only relics. From Fig. 3.3 (bottom) and Fig. 3.4 we see however that clusters with both populate the same regions as those with only relics. Furthermore, the least morphologically disturbed cluster (PSZ2 G205.90+73.76) hosts a dRR and a RH.

In almost all plots we include red circles to denote clusters hosting both a RH and relic(s), and see no clear distinction between the two populations in any, except in the $P_{150\mathrm{MHz}} - M_{500}$ plot (Fig. 3.5). In this plot, we see a clear split in the number of halos in relic-hosting clusters between low-mass and high-mass clusters. The histogram in Fig. 3.5 shows the mass distribution of clusters in our sample. The hatched bars show the distribution for only clusters which also host a RH. Of the 19 clusters which host at least one relic, 11/19=58 ± 15% also host a RH. Including cRRs, this becomes 11/24 = 46 ±14%, as no cRR-hosting cluster also hosts a cRH[3]. The number of RH increases sharply with cluster mass. The fraction of relic-hosting clusters below the median cluster mass, $5.2 \times 10^{14}\mathrm{M}_{\odot}$, which also host an RH, is 3/9= 33±12%, of which none are below $3.5 \times 10^{14}\mathrm{M}_{\odot}$, though there are only 4 such clusters in our sample. Above $5.2 \times 10^{14}\mathrm{M}_{\odot}$ the fraction rises to 8/10=80±18%. If we include cRRs, these become 3/12=25 ±10% and 8/12=67±16%, respectively.

It is already well-established that the occurrence of RHs drops significantly as cluster mass decreases (Cuciti et al., 2015, 2021). Our results suggest that the difference between

[3]PSZ2 G069.39+68.05 hosts a cRH, but we exclude it from occurrence calculations.

the two populations of merging galaxy clusters could be explained by the mass-dependence of RH occurrence (see Cassano et al., 2023). However, since the cluster redshift also plays a significant role in RH occurrence, full comparison of the occurrence in relic-hosting clusters to all clusters in the LoTSS DR2 - PSZ2 sample requires restricting analysis to a relatively small redshift range. Due to the low numbers of RRs, and the correlation of the cluster mass with redshift (Fig. 3.1), even the most-populated redshift bin of Cassano et al. (2023) does not allow for statistical analysis. Larger surveys, with greater numbers of observed relics, will be required to test if the cluster mass can explain the differences between merging cluster populations. We expect that the number of RHs and relics in PSZ2 clusters should more than double by the completion of LoTSS (see Botteon et al., 2022), which should allow greater constraints to be set on the connection between RHs and relics.

3.4.5 Location and size of relics

Radio relics are typically found in cluster outskirts. Vazza et al. (2012) found that this could be explained by the increase in kinetic energy dissipated at the shocks with radius and the fact that relics propagating in the line of sight should be both rare and faint. In their study of simulated relics, they found that most should be located $>$ 800 kpc from the cluster centre. For reference, we plot a line at 800 kpc in Fig. 3.9 (top), which shows the distribution of our relic - cluster centre distances. In line with expectations, most (25/28=89 $\pm$ 19%, excluding PSZ2 G107.10+65.32) relics are located beyond this projected distance from the cluster centre, and none below 450 kpc. Additionally, only a few relics lie at very large distances from the cluster centre, in line with Vazza et al. (2012), who showed that the kinetic flux through a shock peaks around $\sim$ 1 Mpc and subsequently decreases towards larger radii. When plotted instead as a fraction of the cluster R_{500} (Fig. 3.9, bottom), we see a similar picture, that is to say that all relics lie $> 0.5R_{500}$ from the cluster centre, and more than half lie $> R_{500}$ (15/28). This is in line with simulations by Zhang et al. (2019), who argued that the steep gas density profiles in cluster outskirts $\gtrsim R_{500}$ create a "habitable zone" for long-lived, runaway merger shocks. The selection criteria used to define relics likely plays a role in the lack of relics at small radii. Since relics were classified as such by their location outside the bulk of ICM emission, our results may be biased towards larger cluster centre distances. However, relics located near the cluster centre are rare (e.g. Bonafede et al., 2012; Feretti et al., 2012, FdG14).

As in previous statistical studies of relics (van Weeren et al., 2009; Bonafede et al., 2012, FdG14), we find that relics further from their cluster centre are typically larger, that is to say that they have a larger LLS (see Fig. 3.8). We also find that a larger LLS tends to be associated with a larger downstream width. This suggests that shock surfaces expand as they propagate into lower-density environments. For comparison, we also plot the LLS-D_{RR-c} correlation of FdG14. We find that the slopes are very similar, despite the large difference in observing frequency. This shows that the LLS does not change much as we move to lower frequencies, which we might expect, since the line joining the most distant relic regions typically lies parallel to the shock front.

3.5 Conclusions

In this paper we have presented the first statistical sample of RRs observed at 150 MHz, systematically measuring the relic properties in a uniform manner. We used the LoTSS DR2 - PSZ2 sample of galaxy clusters (Botteon et al., 2022). Where available, archival X-ray data has been utilised to aid in source classification and cluster property measurements (full anaylsis of the sample in X-rays will follow in Zhang et al., 2023). Our main results are as follows:

- We find that RRs are relatively rare phenomena, even when moving to low frequencies. In the LoTSS DR2 - PSZ2 sample, $\sim$ 10% of clusters host at least one relic. This is greater than at higher frequencies, however it is nonetheless much lower than predicted by simulations.
- We confirm the relationship between RRs and merging galaxy clusters. Radio relic-hosting clusters are among the most dynamically disturbed in the LoTSS DR2 - PSZ2 sample.
- We have revisited previous correlations of RR properties. We find a positive correlation between the RR power and the cluster mass (p = 0.003). We do however find evidence that cluster mass actually sets an upper limit on the power of a relic, rather than being a direct driver. We find a correlation between relic power and its LLS, though only when cRRs are included (p = 0.029). We also find a correlation between relic LLS and its radial distance from the cluster (p = 0.002) and as a fraction of cluster R_{500} (p < 0.001), that is to say that relics located further from the cluster centre tend to be larger.
- We have developed methods to measure the properties of a relic in a systematic and homogeneous way. In particular, we have introduced a statistical method of defining the relic downstream width as the median of the distribution of widths measured along the relic's extent. Using this, we have shown that, even given optimistic downstream shock properties, the width of RRs in almost all cases is too large to be explained by only synchrotron and inverse Compton losses.
- We have compared the properties of the relic-hosting clusters in our sample which do, and do not, also host a RH. We do not find any evidence for the two populations being at different evolutionary stages, nor differences in the merging state of the host cluster. We find that the change in halo occurrence as a function of mass and redshift could go some way to explaining the discrepancy, but the sample is too small for conclusive evidence.
- We find that most relics lie in the cluster outskirts. $\sim$ 90% of relics lie >800 kpc from their cluster centre, in line with cosmological simulations. All relics lie $> 0.5R_{500}$ and more than half lie above R_{500}.

The low occurrence of RRs means that large samples are necessary to understand their statistical properties. Extrapolating from LoTSS DR2 to the full LoTSS survey, the number

of detected relics in *Planck* PSZ2 clusters is expected to more than double (Botteon et al., 2022). This work will therefore be expanded in future, improving the constraints we can set on RR properties.

Acknowledgements

FdG and MB acknowledge support from the Deutsche Forschungsgemeinschaft under Germany's Excellence Strategy - EXC 2121 "Quantum Universe" - 390833306. ABotteon acknowledges support from the ERC-StG DRANOEL n. 714245 and from the VIDI research programme with project number 639.042.729, which is financed by the Netherlands Organisation for Scientific Research (NWO). FG, MR, and RC acknowledge support from INAF mainstream project 'Galaxy Clusters Science with LOFAR' 1.05.01.86.05. ABonafede acknowledges support from ERC Stg DRANOEL n. 714245 and MIUR FARE grant "SMS". VC and GDG acknowledge support from the Alexander von Humboldt Foundation. AD acknowledges support by the BMBF Verbundforschung under the grant 05A20STA. DNH acknowledges support from the ERC through the grant ERC-Stg DRANOEL n. 714245. KR acknowledges financial support from the ERC Starting Grant "MAGCOW" no. 714196. RJvW acknowledges support from the ERC Starting Grant ClusterWeb 804208.

The Low Frequency Array, designed and constructed by ASTRON, has facilities in several countries, that are owned by various parties (each with their own funding sources), and that are collectively operated by the International LOFAR Telescope (ILT) foundation under a joint scientific policy.

The Jülich LOFAR Long Term Archive and the German LOFAR network are both coordinated and operated by the Jülich Supercomputing Centre (JSC), and computing resources on the supercomputer JUWELS at JSC were provided by the Gauss Centre for Supercomputing e.V. (grant CHTB00) through the John von Neumann Institute for Computing (NIC).

This research has made use of SAOImage DS9, developed by Smithsonian Astrophysical Observatory. This research has made use of NASA's Astrophysics Data System.

3.6 Appendix A: Radio relic image gallery

Fig. 3.14 shows LOFAR 50kpc-taper, discrete source-subtracted images of all RRs in the LoTSS DR2 - PSZ2 galaxy cluster sample. The images are taken from Botteon et al. (2022) and are also available on the project website[4]. All images are centred on the PSZ2 cluster coordinates, except PSZ2 G165.46+66.15 which is centred on the X-ray centroid. The RRs in PSZ2 G089.52+62.34, PSZ2 G091.79-27.00, and PSZ2 G165.46+66.15 were not fully covered by the images, so we have re-imaged these clusters. The black circle denotes

[4]https://lofar-surveys.org/planck_dr2.html

the cluster R_{500}, centred on the PSZ2 coordinates. Each image includes a 1 Mpc scalebar and information on the cluster mass, redshift, and image r.m.s. The blue ellipse shows the image beam size. White crosses denote the coordinates used as the relic positions (see Sec. 3.2.2).

Fig. 3.15 shows the same radio images as white contours, overlaid on *Chandra*/*XMM-Newton* X-ray images. The instrument used is shown in the image title. The radio contours are spaced by factor of 2, starting at $2\sigma_{rms}$. PSZ2 G089.52+62.34, PSZ2 G091.79-27.00, and PSZ2 G165.46+66.15 are again re-imaged. The R_{500}, centred on the PSZ2 coordinates, is shown as a white circle. The position of the X-ray centroids, used as the cluster centres in our analysis, are denoted by black crosses. We note that, for PSZ2 G107.10+65.32, only the X-ray centroid of the S subcluster is plotted. All other information is as in Fig. 3.14.

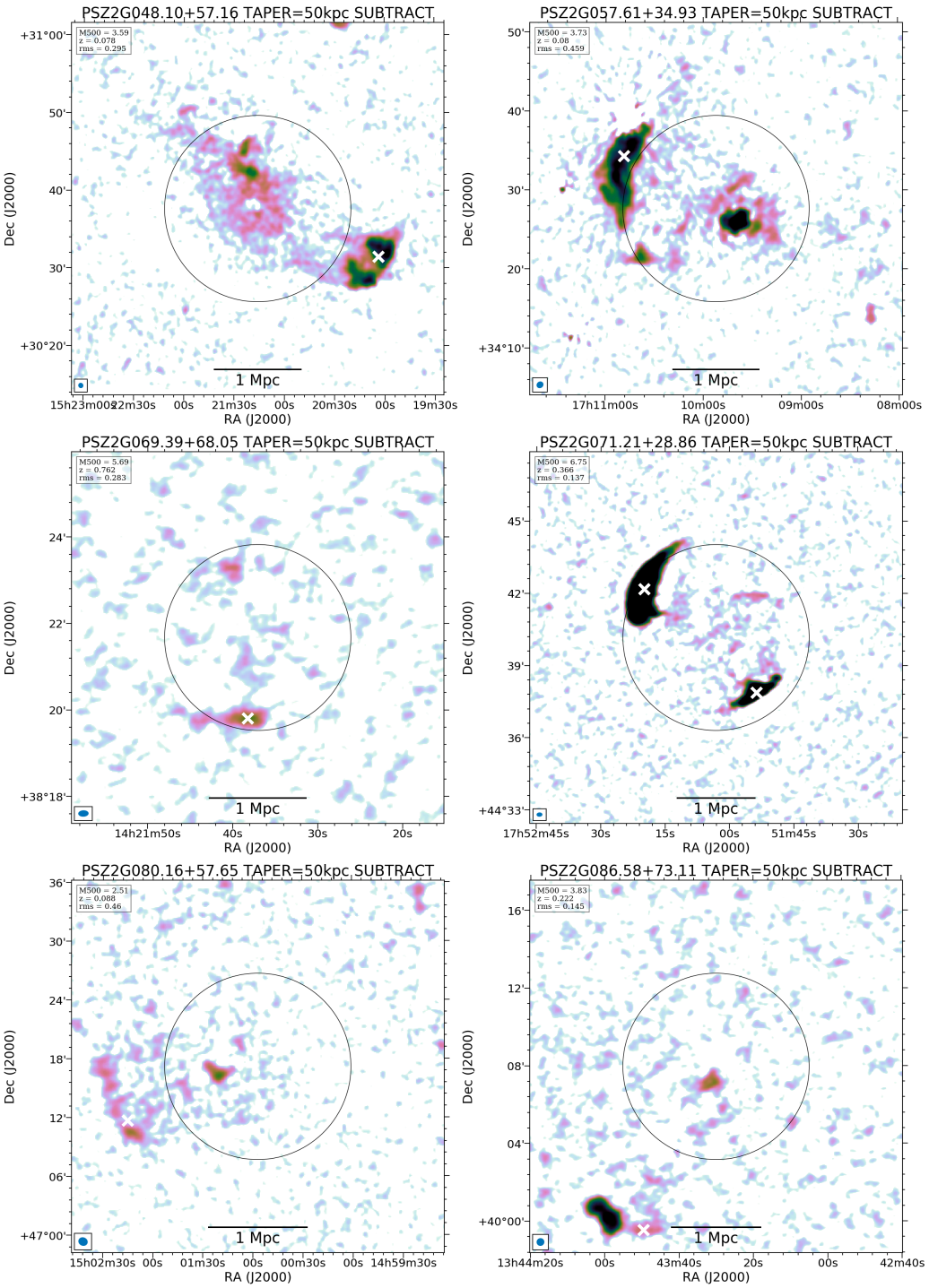

Figure 3.14: LOFAR 50kpc-taper, discrete source-subtracted images of the RRs in the LoTSS DR2 - PSZ2 sample, from Botteon et al. (2022). The images and R_{500} (black circles) are centred on the PSZ2 coordinate. The image of PSZ2 G165.46+66.15 is centred on the X-ray centroid. PSZ2 G089.52+62.34, PSZ2 G091.79-27.00, and PSZ2 G165.46+66.15 have been re-imaged. A scalebar, denoting 1 Mpc, is shown in black. The beam is shown in the bottom-left corner, and the mass (M_{500}, in units of $10^{14} M_{\odot}$), redshift (z), and image noise (rms, in units of mJy beam^{-1}) are reported in the top-left corner. White crosses mark the location of the relics, as used throughout the paper (see Sec. 3.2.2 for a description of their calculation).

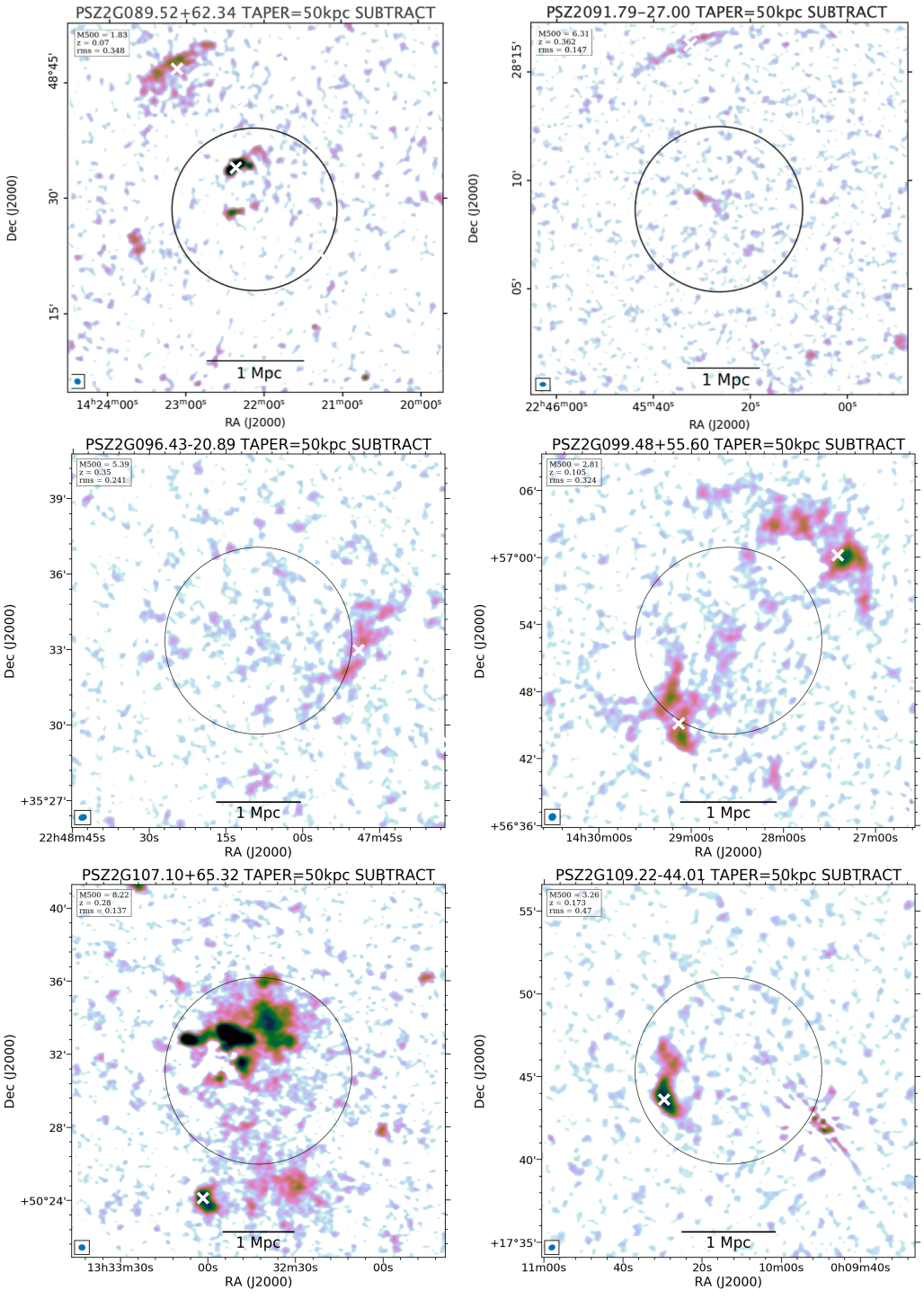

Figure 3.14: continued.

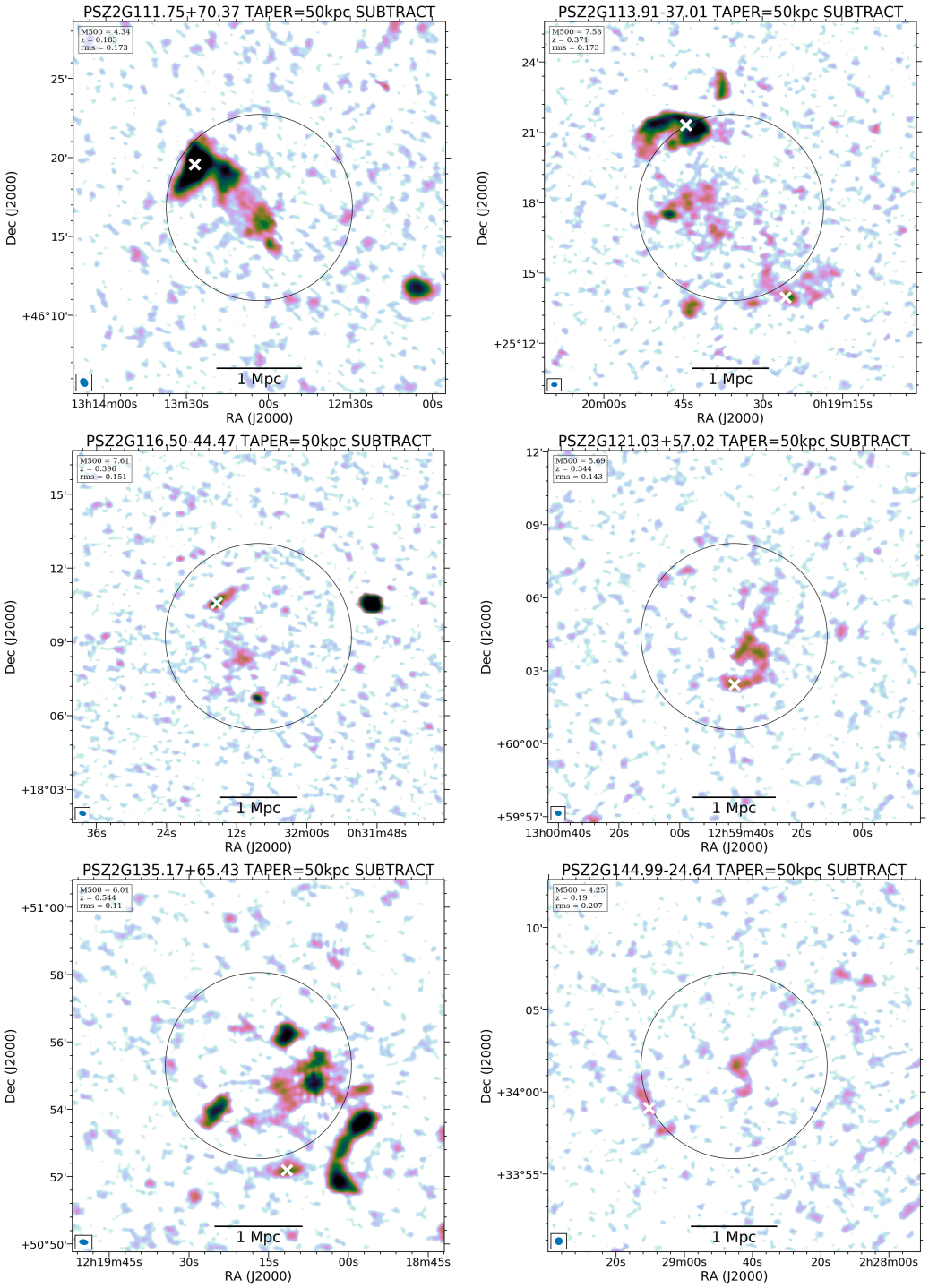

Figure 3.14: continued.

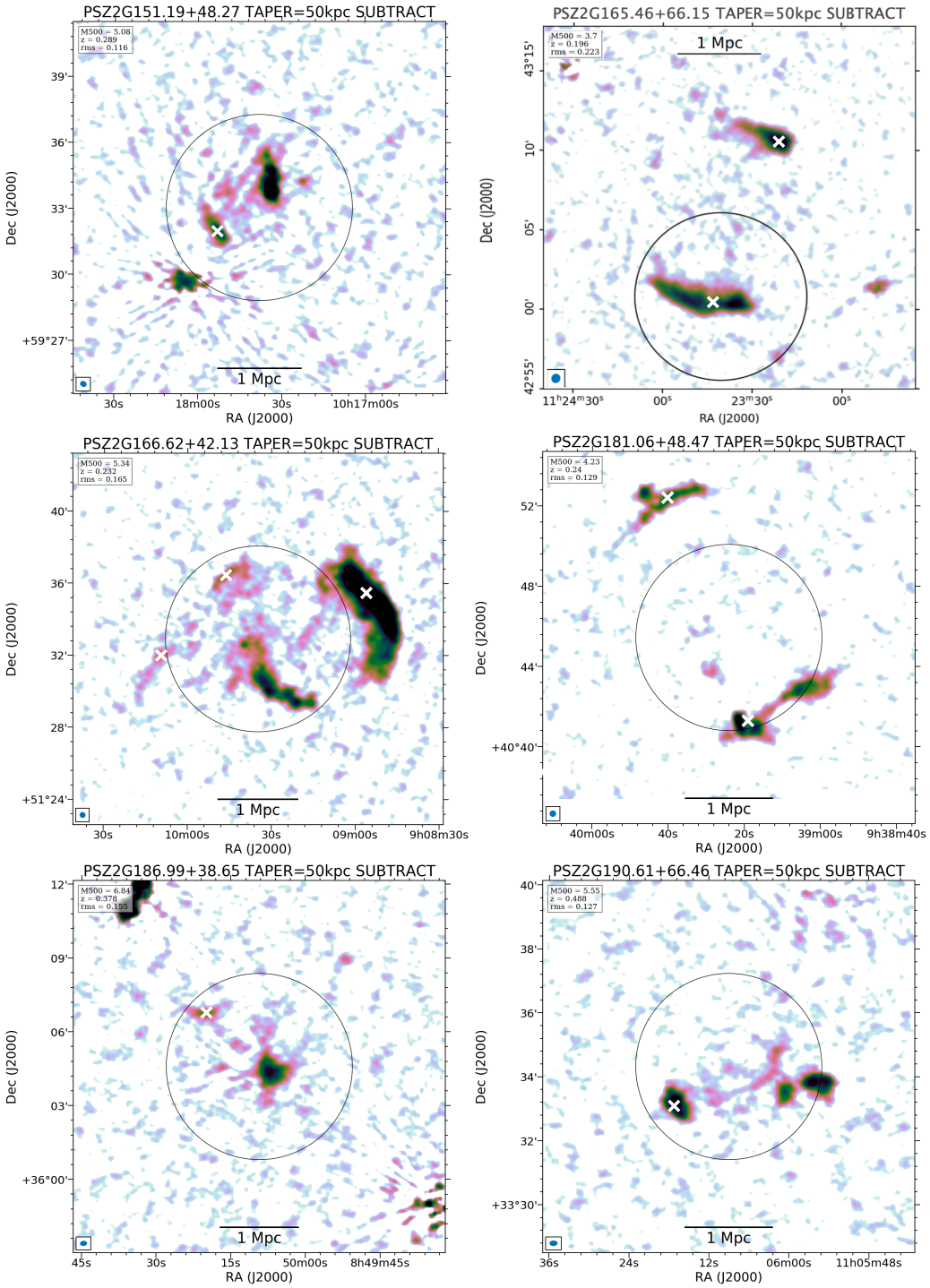

Figure 3.14: continued.

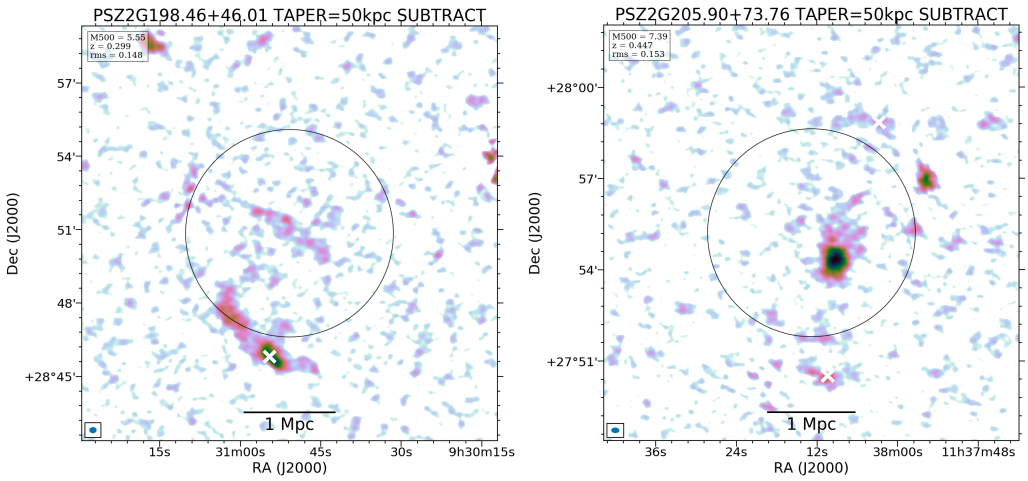

Figure 3.14: continued.

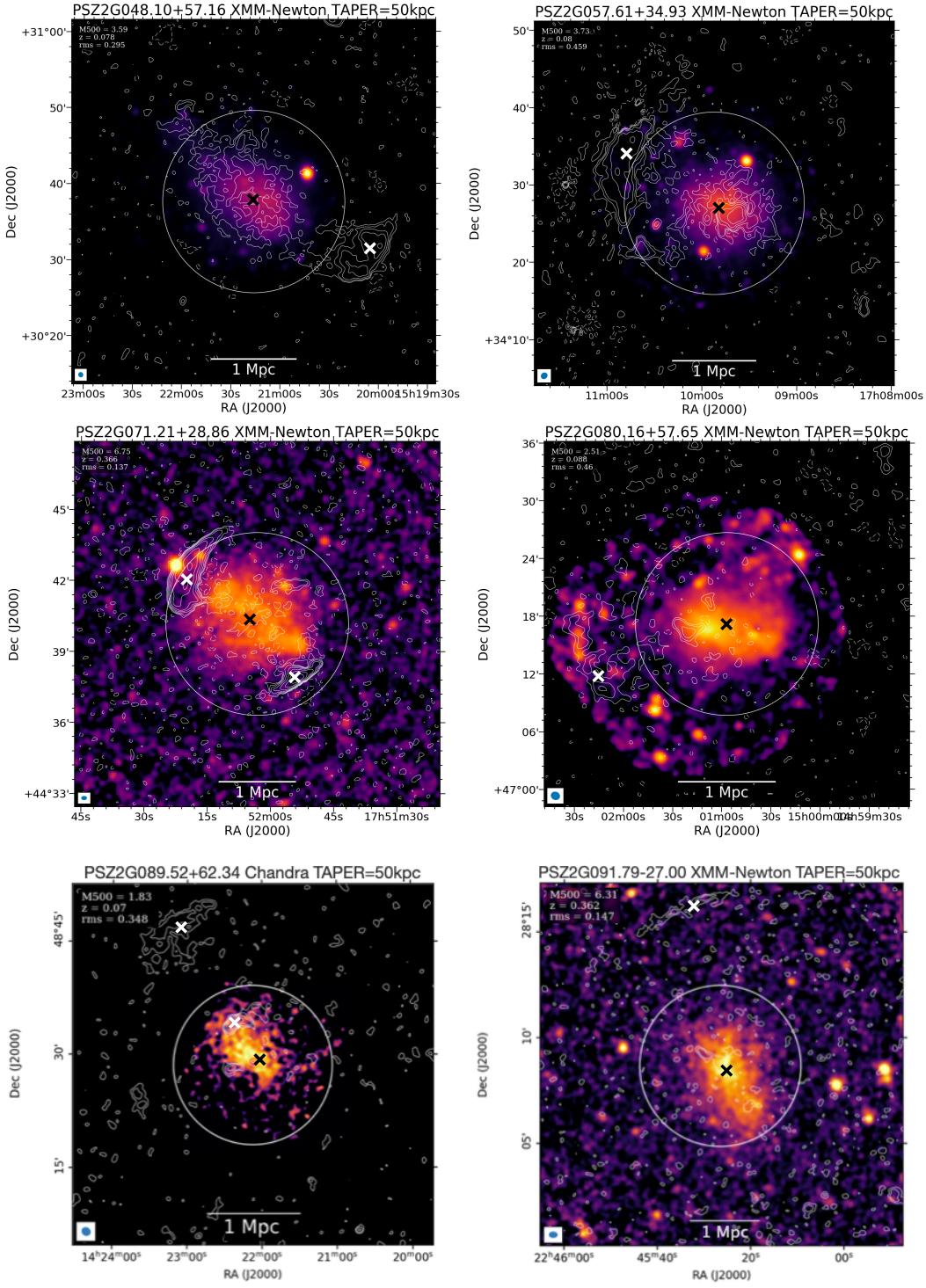

Figure 3.15: *Chandra*/*XMM-Newton* images of the relic-hosting clusters in our sample. The white contours show the corresponding radio images (Fig. 3.14) spaced by a factor of 2, starting at $2\sigma_{rms}$. Black crosses mark the position of the X-ray centroid. We note that, for PSZ2 G107.10+65.32, only the X-ray centroid of the S subcluster is plotted. All other information is as in Fig. 3.14.

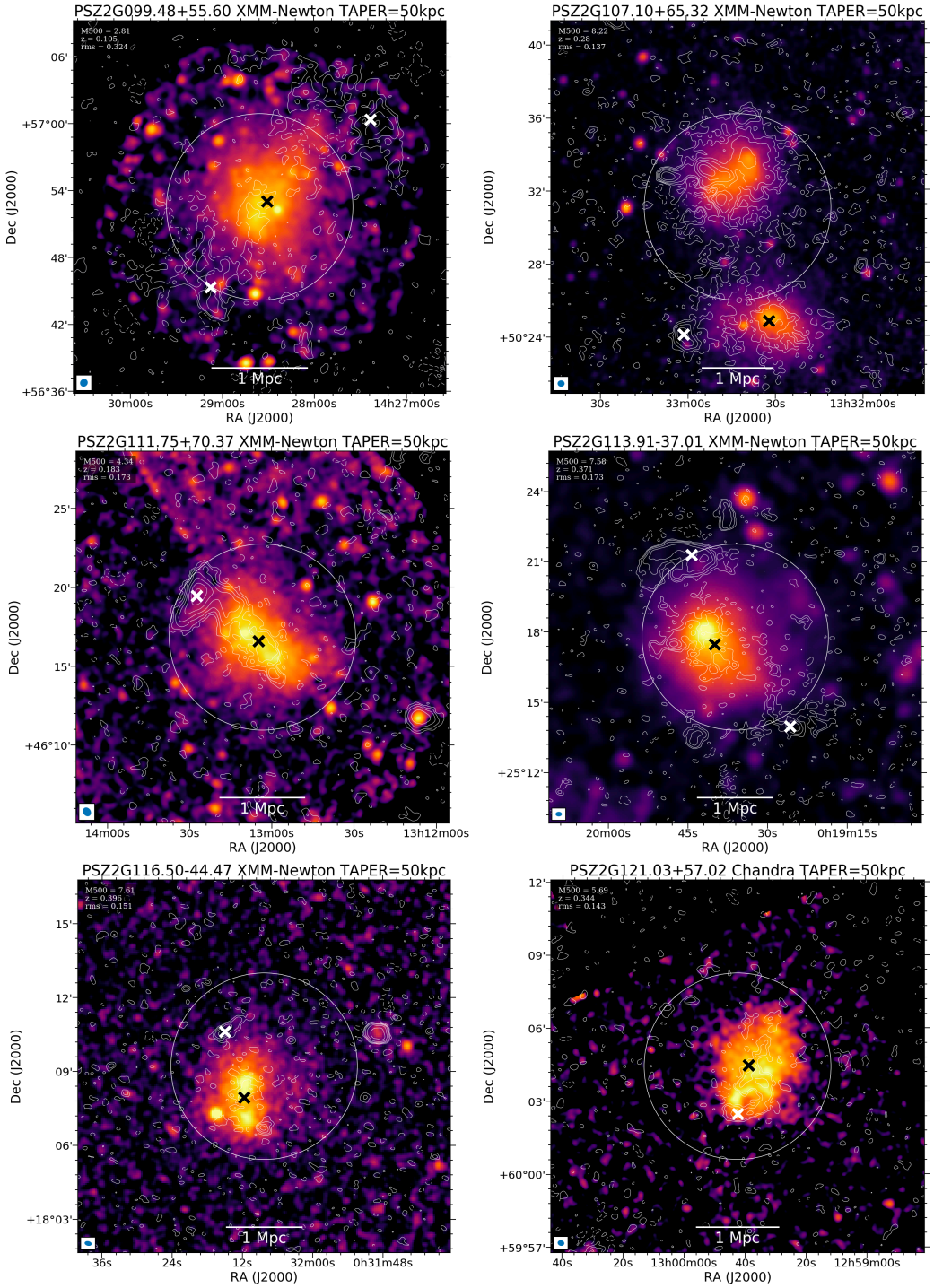

Figure 3.15: continued.

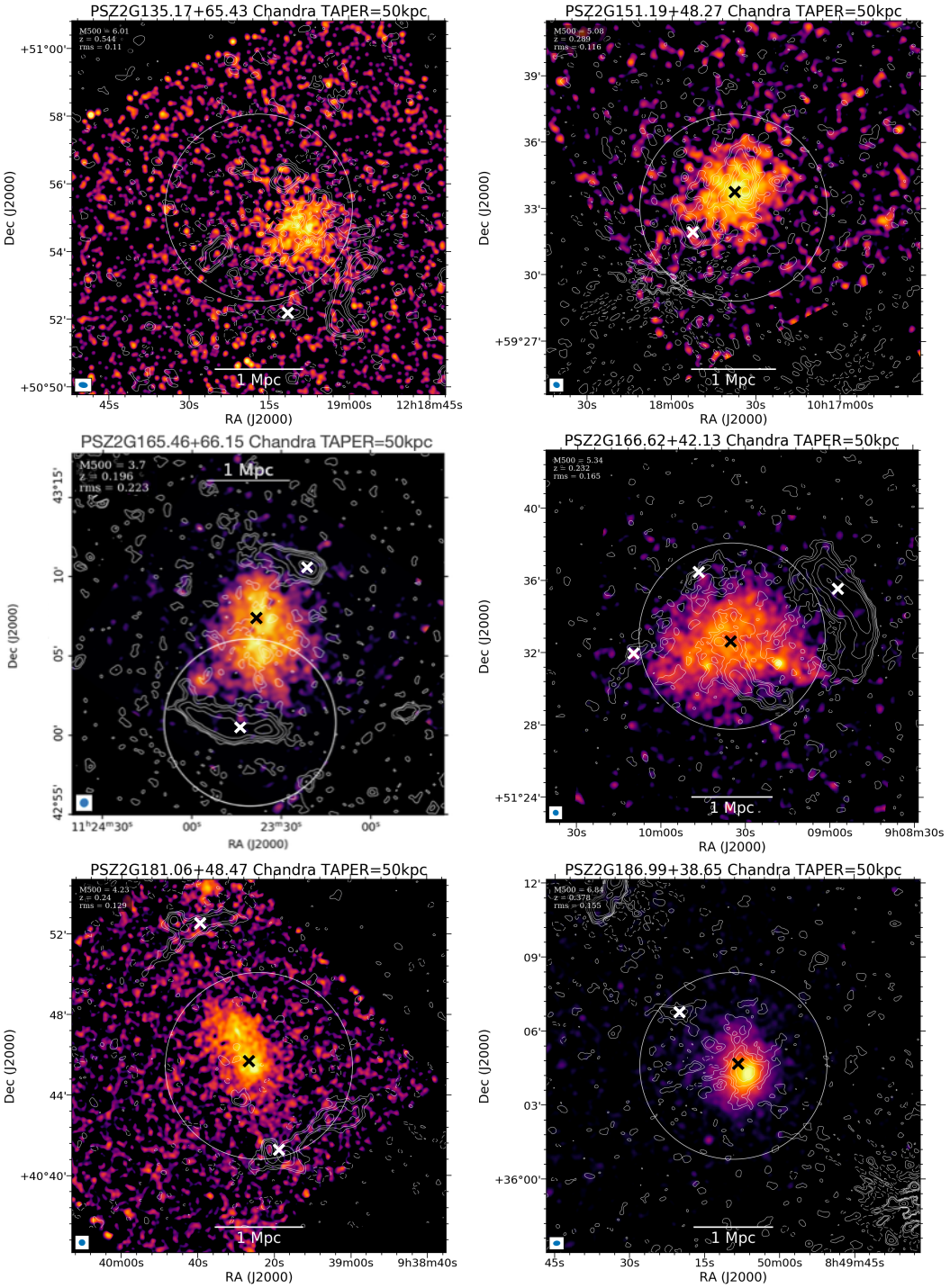

Figure 3.15: continued.

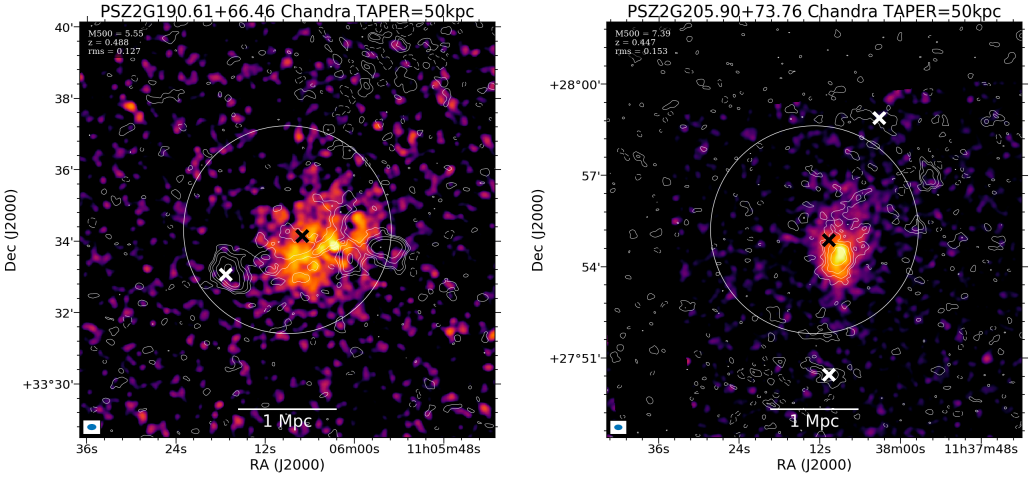

Figure 3.15: continued.

3.7 Appendix B: Comparison with FdG14 powers

In Fig. 3.6 we compare the power vs. mass scaling relations of the relics in this sample (150 MHz) and those used by FdG14 (1.4 GHz). To make a completely fair comparison, the cosmology used to calculate the relic powers should be the same. In Fig. 3.16 we reproduce Fig. 3.6 (top) with the relic powers from our sample recomputed with the same cosmology as FdG14 (ΛCDM cosmology with $\Omega_\Lambda = 0.73$, $\Omega_m = 0.27$, and $H_0 = 71$ km s^{-1} Mpc^{-1}), since the scaling relation in FdG14 was calculated with this cosmology. The slope and intercept (orthogonal fit) of the line of best fit for the recomputed powers are B = 5.84 ± 1.31 and A = -60.74 ± 19.27.

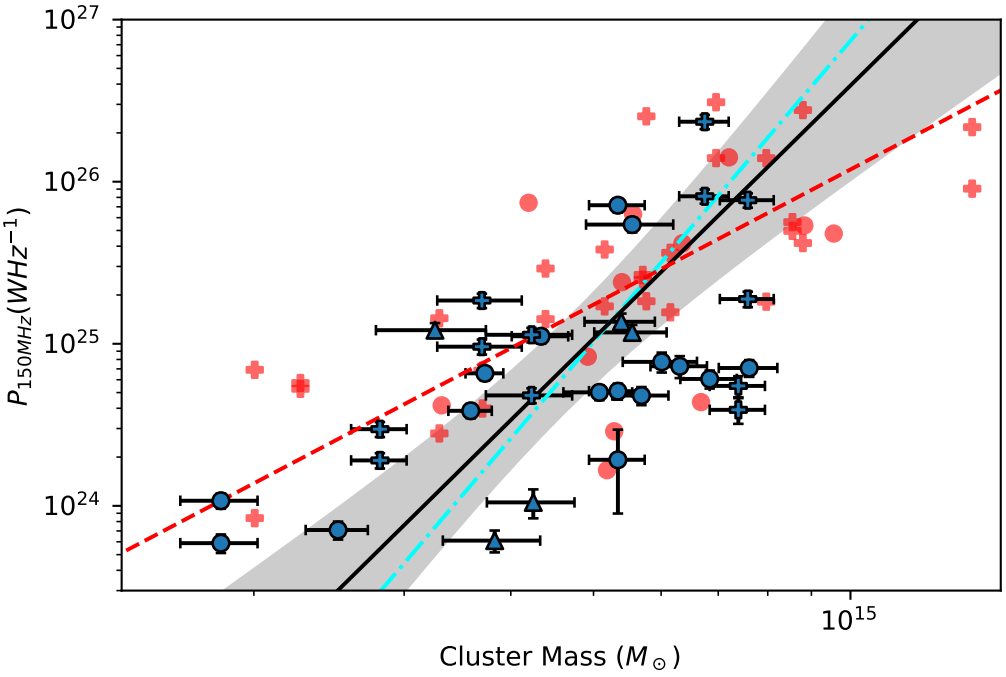

Figure 3.16: Same as Fig. 3.6 (top) but the relic powers from the DR2 sample have been recomputed using the cosmology used by FdG14.

3.8 Appendix C: Fitting methods

The slope and intercept obtained when fitting a regression line depends on the fitting method (see Tab. 3.2. In this paper we report the parameters for four different methods: orthogonal; Y|X; X|Y and the bisector of Y|X and X|Y. In Fig. 3.17 we show the regression line (confirmed relics only) for each fitting method.

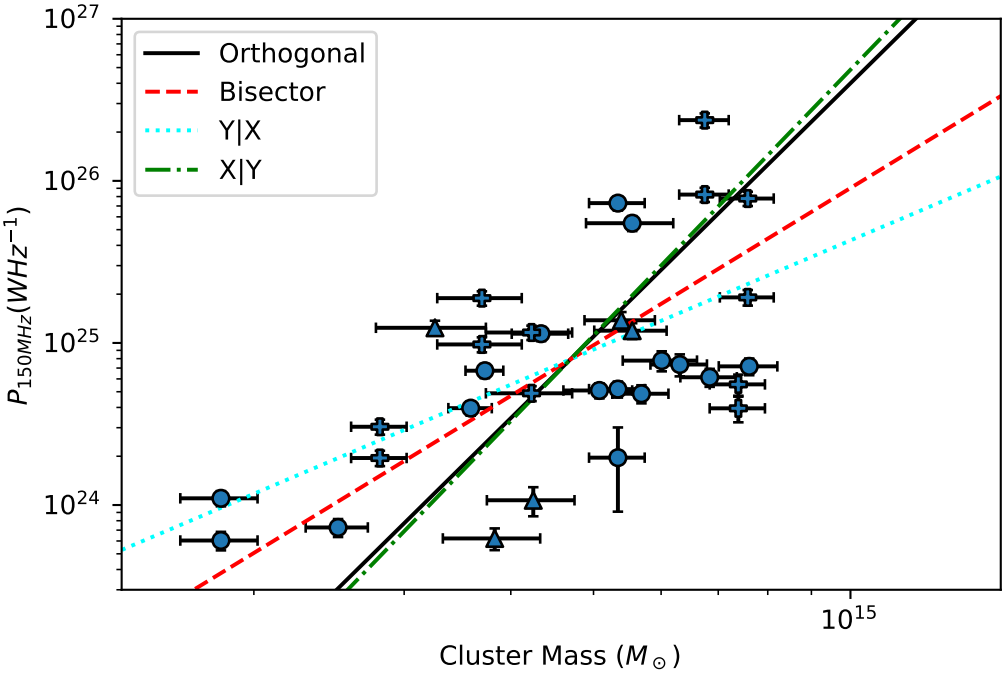

Figure 3.17: Relic power vs. cluster mass for confirmed relics only. The regression lines are shown for all four fitting methods.

Chapter 4

Conclusions

4.1 Motivation

A fraction of the enormous amounts of energy injected into the intracluster medium (ICM) of galaxy clusters goes into the acceleration of cosmic ray electrons (CRes) at shocks and through turbulence. The result is Mpc-scale diffuse radio emission, which is observed in the form of radio halos (RHs) and radio relics (RRs; see van Weeren et al., 2019, for a review). The low surface brightness and steep spectra of these sources makes them challenging to observe. To-date relatively few have been discovered, representing only the brightest, nearest objects which are observable at higher radio frequencies.

The advent of low-frequency, high-sensitivity radio telescopes, such as the LOw Frequency ARray (LOFAR; van Haarlem et al., 2013), and in particular the ongoing LOFAR Two-meter Sky Survey (LoTSS; Shimwell et al., 2017), has allowed the discovery of many more of these objects, and an insight into the lowest-energy CRe populations in galaxy clusters. This thesis represents my contribution to the understanding merger-induced, cluster-scale emission at low radio frequencies.

Specifically, with regards to my aims outlined in Sec. 1.4, my work focussed on improving our understanding of the following:

1. **Can lobes of previous AGN activity provide seed electrons to produce radio relics, and are the properties of the relics altered?** There is growing evidence that acceleration of electrons from the thermal pool to relativistic energies by DSA is insufficient to produce the RRs observed, and re-acceleration of mildly-relativistic CRes is required (e.g. Botteon et al., 2020a). A few RRs show direct evidence of having been produced by re-acceleration of the tails of radio galaxies (e.g. Bonafede et al., 2014; Shimwell et al., 2015; van Weeren et al., 2017), but these are the exceptions, rather than the rule. Are there other sources of CRe for re-acceleration and how can they affect the relic?

2. **What are the statistical properties of radio relics as a population? Do the scaling**

relations previously reported extend to low frequency? RRs are uncommon radio objects usually found in the outskirts of merging clusters. Do we find this for a well-selected sample of relics? Previous studies of the properties of RRs as a population have revealed a correlation between the size of a relic and its distance from the cluster centre, indicating that the shock surface grows as it travels (van Weeren et al., 2009; Bonafede et al., 2012; de Gasperin et al., 2014). de Gasperin et al. (2014) also found that the radio power of a relic correlates with the cluster mass, indicating that the mass is a driver of the energy injected by the shock. However, simulations suggest that observations are missing a population of low-power RRs in low-mass clusters, which could affect these findings (Nuza et al., 2017; Brüggen & Vazza, 2020). Do we find similar scaling relations at low frequency, and do we find faint RRs residing in low-mass clusters?

3. **Is DSA the only CRe acceleration mechanism present in radio relics, or does turbulence also play a role?** In the absence of another acceleration mechanism, the downstream width of a relic is governed by synchrotron and IC losses. The widths of a few RRs have been found to be too large to be explained in this way (e.g. Kang, 2016; Kang et al., 2017), and this is particularly pronounced at low frequencies (de Gasperin et al., 2020). Do we find that this is common among RRs at low frequency, or are these exceptions? Di Gennaro et al. (2021) found evidence for turbulence in the downstream region of a relic in CIZA J2242.8+5301, which could explain the extended widths. Is evidence of turbulence found in other RRs?

4. **What is the connection between radio relics and radio halos?** Radio halos and relics are both generated by galaxy cluster mergers. However, some merging clusters clusters host both, but others host only one or the other. It is not understood why. Bonafede et al. (2017) investigated the difference between relic-hosting clusters with and without radio halos, but found no conclusive reason for the difference. Can a statistical sample of RRs observed at low frequency explain the existence of these two populations of merging clusters?

4.2 Summary of work

Here I summarise my work and most important findings in the context of the above questions.

1. The double radio relics in PSZ2 G096.88+24.18 had previously been discovered by de Gasperin et al. (2014). In *Radio relics in PSZ2 G096.88+24.18: A connection with pre-existing plasma* we announced the discovery of a connection, between cluster-member radio galaxies and both relics. Of particular interest was the southern relic, where a factor of 4 increase in surface brightness on the eastern side of the relic is connected to a bright, cluster-member galaxy by a faint patch of emission which we dubbed the "Connection". We found that the integrated spectral index steepens from the outer edge of the relic towards the cluster centre ($\alpha \sim -1.0$ to $\alpha \sim -1.6$). This is in line with (re-)acceleration of CRes by a shock propagating outwards,

leaving a trail of CRes in its wake that radiate energy away. However, along the Connection towards the radio galaxy, the spectral index flattens again to $\alpha \sim -1.0$, similar to that observed in Abell 3411-3412 (van Weeren et al., 2017). Additionally, there is a region of the Connection only visible in the LOFAR images, so we were only able to set an upper limit of $\alpha < -1.9$ on the spectral index. We interpret this as the result of shock passage over an old AGN lobe of mildly-relativistic CRes, which has subsequently been compressed and re-accelerated to produce the relic that we observe.

2. The following all relate to *The Planck clusters in the LOFAR sky VI. LoTSS-DR2: Properties of radio relics*, where we took all clusters with *Planck*-derived masses covered by the LoTSS-DR2 area and studied those clusters which host diffuse radio emission; in particular radio relics.

   Previous studies have found that the occurrence of radio relics is $\sim 5\%$ (e.g. Kale et al., 2015). However, simulations suggest that the RRs thus far discovered are just the brightest and we are missing a population of low-power RRs residing in low-mass clusters (Nuza et al., 2017; Brüggen & Vazza, 2020). With the low frequency and high sensitivity of LOFAR, we showed that the occurrence of RRs in our sample is $10 \pm 6\%$. Additionally, 9 of the 11 clusters $< 5 \times 10^{14}\ M_{\odot}$ in our sample were discovered to host RRs for the first time with LOFAR, or in combination with another instrument (Botteon et al., 2022). Our results therefore indicate that LOFAR is indeed able to discover low-power RRs which were previously undetectable at higher frequencies.

   Even without direct detection of a merger shock, radio relics are typically associated with galaxy cluster mergers. This is inferred by measuring the dynamic disturbance of RR-hosting clusters from their X-ray properties. We used the concentration parameter and the centroid shift, derived from X-ray observations, to determine the dynamical state (Zhang et al., 2023). We find that RR-hosting clusters are amongst the most dynamically-disturbed clusters in our sample, strongly indicating a connection with mergers.

   Radio relics are typically located in the outskirts of clusters, where the kinetic energy dissipated into CRe (re-)acceleration at a shock is greatest (Vazza et al., 2012). As predicted, we find that $89 \pm 19\%$ of RRs are located at least 800 kpc from their cluster centre, and none are located at closer than 450 kpc.

   Previous studies of RR populations have indicated a correlation between the longest linear size (LLS) of a relic and its distance from the cluster centre (D_{RR-c}; van Weeren et al., 2009; Bonafede et al., 2012; de Gasperin et al., 2014). We confirm these findings for our sample and show that the LLS scales like LLS $\propto D_{RR-c}^{1.49 \pm 0.27}$, which we show is very similar to the findings of de Gasperin et al. (2014). Our results therefore support the finding that shock surfaces expand as they propagate outwards.

   de Gasperin et al. (2014) also found evidence for a correlation between RR power and cluster mass, indicating that the energy budget in a merger determines the power of a relic. We also find a correlation, however the mass dependency, $P_{150\mathrm{MHz}} \propto M^{5.19 \pm 1.20}$, is much steeper. Additionally, we find that the faintest RRs in our sample

lie close to the detection limit of our radio observations, indicating that we have not yet discovered the least powerful RRs. We therefore interpret this as the cluster mass providing an upper limit on the power of a relic, but that other variables must drive the observed radio power.

3. By measuring the distribution of relic widths for each RR in our sample, in *The Planck clusters in the LOFAR sky VI. LoTSS-DR2: Properties of radio relics* we show that, in comparison to the characteristic width expected for a single site of CRe acceleration with subsequent radiative losses (Kang, 2016), the downstream width is too large. Even for optimistic assumed values of shock Mach number and downstream temperature, the measured widths are too large, and the largest relics in our sample would require unrealistic ICM conditions to explain. We therefore concluded that RRs systematically require a further source of acceleration, such as turbulence, or that the shock structure in RRs is complex and the assumption of a single site of (re-)acceleration is too simplistic.

   Furthermore, in *Radio relics in PSZ2 G096.88+24.18: A connection with pre-existing plasma*, we found that there is very little polarised emission and a complex spectral index distribution in the southern relic. We interpreted this as the result of turbulence in the downstream region of the relic, as the result of either re-acceleration of an already turbulent cloud of CRe related to the AGN, or directly from shock passage downstream.

4. The double radio relics in PSZ2 G096.88+24.18 were first reported in de Gasperin et al. (2014), who also reported a low-significance radio halo detection in the cluster centre. With our higher sensitivity and resolution images, in *Radio relics in PSZ2 G096.88+24.18: A connection with pre-existing plasma* we showed that the radio halo previously reported is actually most likely fossil plasma, with $\alpha < -1.3$, originating from a cluster-member radio galaxy.

   Additionally, the sample of *The Planck clusters in the LOFAR sky VI. LoTSS-DR2: Properties of radio relics* contained detections of both radio relics and halos, allowing direct comparison between RR-hosting clusters with and without RHs. We find no conclusive evidence for a metric which could explain the difference between the two populations, finding that there is no clear distinction in the disturbance or time since merger, using D_{RR-c} as a proxy. The only difference we find is in the mass distribution, finding that $80 \pm 18\%$ of RR-hosting clusters above the median cluster mass of our sample, 5.2×10^{14} $M_{\odot}$, also host RHs, but only $33 \pm 12\%$ do below this mass. We conclude therefore that the difference may be driven by the mass dependence of the occurrence of RHs (Cassano & Brunetti, 2005), but larger samples are required to determine if this can entirely explain the difference.

4.3 Future work

The work presented in this thesis demonstrates the power of low-frequency radio observatories, and in particular those able to perform large-scale surveys, such as LOFAR, in

furthering our understanding of the physics of the intracluster medium and the processes responsible for diffuse radio emission in galaxy clusters.

One of the largest obstacles to our understanding of merger-induced diffuse radio emission in galaxy clusters, especially radio relics, is the low number discovered. The work presented in this thesis demonstrates the need for larger numbers of radio relics and halos to understand their statistical properties, in particular in low-mass galaxy clusters. The low surface brightness and steep spectra of these sources, however, makes their detection challenging, and it is becoming increasingly clear that the halos and relics discovered at higher frequencies represent only the most powerful. The ongoing LoTSS has, as of data release 2, covered only 27% of the northern hemisphere. Nuza et al. (2012) predicted the detection of $\sim$ 2500 previously undetected radio relics by LOFAR, and whilst the work presented here casts some doubt on the actual number of detections being that large, LoTSS, and LOFAR in general, has already discovered many new diffuse radio sources. This will only increase as LoTSS continues, and the upcoming SKA observatory in the southern hemisphere comes online.

The number of faint, extremely steep spectrum radio sources, originating from populations of fossil cosmic ray electrons associated with previous episodes of activity, discovered in galaxy clusters, is increasing with more observations at the lowest radio frequencies. In particular, my work on the steep spectrum source in PSZ2 G096.88+24.18, revealed only at low frequencies, highlights the value in observations in the $\sim$ 100 MHz regime in our understanding of the sources of seed electrons possibly required to produce relics and halos. In this regard, the companion low-band antenna survey to LoTSS, LoLSS, operating below 100 MHz, will allow for the discovery of more of these populations of fossil electrons. Additionally, the lower frequency regime will allow for the resolved and integrated spectral index studies of these sources vital to understand, for example, the shock strength and structure, and downstream regions in radio relics. In this regard, as well as in relation to halos, the upcoming *Athena* telescope is expected to be able to directly detect turbulence, through the centroid shift and broadening of X-ray emission lines. Furthermore, in the forthcoming LOFAR 2.0, amongst other improvements, it will be possible to simultaneously observe with the high- and low-band antennas, allowing for the detection and spectral study of many more steep-spectrum sources.

Appendix

A.1 Paper II data

The data used in Paper II, *The Planck clusters in the LOFAR sky VI. LoTSS-DR2: Properties of radio relics*, are published in Botteon et al. (2022) (Table A.4.). However, I took the measurements and devised the methods to take them, so I include the data here.

Name	Position	RA_{RR} [deg]	DEC_{RR} [deg]	S_{150} [mJy]	S_{150err} [mJy]	P_{150} [W Hz^{-1}]	P_{150err} [W Hz^{-1}]	LLS [kpc]	LLS_{err} [kpc]	Width [kpc]	$Width_{err}$ [kpc]	Average SB [μJy beam^{-1}]	D_{RR-c} [kpc]	$D_{RR-cerr}$ [kpc]	D_{RR-RR} [kpc]	$D_{RR-RRerr}$ [kpc]
PSZ2 G048.10+57.16		230.0114	30.5267	264.28	26.83	3.96e+24	4.02e+23	998	35	395	182	2940	1515	206		
PSZ2 G057.61+34.93		257.7043	34.5640	426.57	42.90	6.74e+24	6.77e+23	1361	44	450	167	5579	1269	176		
PSZ2 G069.39+68.05		215.4091	38.3299	28.47	4.58	7.61e+25	1.22e+25	1489	56	109	153	1237				
PSZ2 G071.21+28.86	N	268.0816	44.7043	518.11	51.83	2.37e+26	2.37e+25	1254	39	291	149	6205	998	42	1941	39
PSZ2 G071.21+28.86	S	267.9735	44.6313	179.66	17.99	8.23e+25	8.24e+24	813	39	136	86	5134	965	42	1941	39
PSZ2 G080.16+57.65		225.5644	47.1942	37.63	4.78	7.27e+23	9.24e+22	1073	50	173	86	1667	1418	196		
PSZ2 G086.58+73.11		205.9581	39.9924	4.28	0.66	6.22e+23	9.53e+22	394	44	121	42	584				
PSZ2 G089.52+62.34	N2	215.8002	48.7878	92.49	9.94	1.10e+24	1.19e+23	1213	35	296	200	2742	1721	233		
PSZ2 G089.52+62.34	N1	215.5888	48.5719	50.64	6.63	6.04e+23	7.90e+22	273	35	107	39	5147	484	74		
PSZ2 G091.79-27.00		341.3831	28.2727	16.48	2.55	7.36e+24	1.14e+24	1535	41	164	96	1176	2510	339		
PSZ2 G096.43-20.89		341.9545	35.5495	33.56	4.16	1.38e+25	1.71e+24	1482	53	279	173	839				
PSZ2 G099.48+55.60	N	216.8435	57.0057	108.16	11.44	3.04e+24	3.22e+23	1711	45	354	173	1398	1366	49	2405	45
PSZ2 G099.48+55.60	S	217.2878	56.7582	69.38	7.49	1.95e+24	2.11e+23	1090	45	229	160	1609	1068	48	2405	45
PSZ2 G107.10+65.32		203.2562	50.4015	21.49	2.25	5.29e+24	5.53e+23	538	50	266	113	1258	1211	170		
PSZ2 G109.22-44.01		2.6228	17.7278	148.71	15.75	1.24e+25	1.31e+24	1168	40	211	100	3216				
PSZ2 G111.75+70.37		198.3618	46.3271	120.37	12.07	1.14e+25	1.14e+24	874	56	317	93	4520	898	133		
PSZ2 G113.91-37.01	N	4.9365	25.3543	164.61	16.57	7.78e+25	7.84e+24	1172	43	412	155	2033	1210	47	2605	43
PSZ2 G113.91-37.01	S	4.8569	25.2329	40.41	4.43	1.91e+25	2.10e+24	1481	43	296	128	1361	1464	49	2605	43
PSZ2 G116.50-44.47		8.0645	18.1766	13.00	1.54	7.17e+24	8.48e+23	555	47	118	79	946	890	128		
PSZ2 G121.03+57.02		194.9253	60.0416	12.26	1.57	4.86e+24	6.21e+23	542	44	141	45	759	570	88		
PSZ2 G135.17+65.43		184.7975	50.8694	6.61	0.93	7.78e+24	1.10e+24	654	54	125	63	552	1110	158		
PSZ2 G144.99-24.64		37.2926	33.9827	10.45	2.12	1.07e+24	2.18e+23	773	48	153	82	749				
PSZ2 G151.19+48.27		154.4696	59.5328	19.24	2.05	5.09e+24	5.44e+23	812	43	122	90	816	682	101		
PSZ2 G165.46+66.15	N	170.8381	43.1768	89.07	9.43	9.79e+24	1.04e+24	1069	49	339	120	2270	843	51	2115	49
PSZ2 G165.46+66.15	S	170.9279	43.0079	171.63	17.51	1.89e+25	1.92e+24	1638	49	385	188	2571	1387	53	2115	49
PSZ2 G166.62+42.13	W	137.2336	51.5893	454.39	45.53	7.29e+25	7.30e+24	1901	39	718	238	2529	1462	200		
PSZ2 G166.62+42.13	N	137.4405	51.6072	32.37	3.67	5.19e+24	5.88e+23	932	39	364	163	675	917	129		
PSZ2 G166.62+42.13	E	137.5390	51.5332	12.21	6.52	1.96e+24	1.05e+24	1100	39	148	71	1080	1204	166		
PSZ2 G181.06+48.47	N	144.9131	40.8741	28.22	2.98	4.89e+24	5.17e+23	1394	39	135	67	925	1660	47	2694	39
PSZ2 G181.06+48.47	S	144.8281	40.6879	66.76	6.83	1.16e+25	1.18e+24	1660	39	207	122	1083	1035	42	2694	39
PSZ2 G186.99+38.65		132.5838	36.1125	12.42	1.58	6.14e+24	7.80e+23	723	46	136	73	705	1030	145		
PSZ2 G190.61+66.46		166.5720	33.5517	60.49	6.43	5.48e+25	5.82e+24	573	48	184	180	2331	865	126		
PSZ2 G198.46+46.01		142.7257	28.7635	41.68	4.64	1.19e+25	1.33e+24	1494	43	247	172	694				
PSZ2 G205.90+73.76	N	174.5111	27.9806	5.37	0.97	3.95e+24	7.12e+23	664	48	125	42	791	1490	53	2958	48
PSZ2 G205.90+73.76	S	174.5439	27.8404	7.55	1.12	5.55e+24	8.26e+23	655	48	155	58	1028	1540	54	2958	48

Table A.1: Col. 1: PSZ2 name; Col. 2: position of the relic with respect to the cluster; Cols. 3 and 4: coordinates of the radio relic; Cols. 5 and 6: flux density; Cols. 7 and 8: radio power and its error; Cols. 9 and 10: longest linear size and its error; Cols. 11 and 12: width and its error; Col. 13: average surface brightness; Cols. 14 and 15: distance between radio relic and X-ray centroid and its error; Cols. 16 and 17: distance between double radio relics and its error.

Acknowledgements

First and foremost I would like to thank my supervisor, Francesco, and my unofficial supervisor, Virginia, without whom I definitely would not be writing this. I could not have asked for nicer, more helpful supervisors.
Thank you, to my parents, who inexplicably read everything I wrote, understanding none of it, and who, along with my grandpa, were at times the only ones who believed I would finish. This is for you. To my relentlessly-weird siblings, who have about as much idea of what I do as any stranger on the street does, and probably wouldn't care if I won a Nobel prize. It's impossible to be stressed around your nonsense. To Jeevan, at times the only thing keeping me remotely sane and with whom, and Fahd, I've lost countless nights talking about anything and everything. To Ksyusha, David, Jess, Freddie and all my friends in Germany, the UK and Australia, who are probably sick of hearing me talk about my thesis and are the people I can truly rely on. And finally, thank you to Paola and Marco, who always made coming in to the office fun.
It's gone. It's done.

Bibliography

Ackermann, M., Ajello, M., Allafort, A., et al. 2010, The Astrophysical Journal Letters, 717, 14

Akamatsu, H. & Kawahara, H. 2013, Publications of the Astronomical Society of Japan, 65, 16

Akamatsu, H., Mizuno, M., Ota, N., et al. 2017, Astronomy & Astrophysics, 600, A100

Akritas, M. G. & Bershady, M. A. 1996, The Astrophysical Journal, 470, 706

Allen, S. W. & Fabian, A. C. 1997, Monthly Notices of the Royal Astronomical Society, 286, 583

Araya-Melo, P. A., Aragón-Calvo, M. A., Brüggen, M., & Hoeft, M. 2012, Monthly Notices of the Royal Astronomical Society, 423, 2325

Arnaud, M. & Evrard, A. E. 1999, Monthly Notices of the Royal Astronomical Society, 305, 631

Arnaud, M., Pointecouteau, E., & Pratt, G. W. 2007, Astronomy & Astrophysics, 474, L37

Arnaud, M., Pratt, G. W., Piffaretti, R., et al. 2010, Astronomy & Astrophysics, 517, A92

Ascasibar, Y. & Markevitch, M. 2006, The Astrophysical Journal, 650, 102

Bagchi, J., Enßlin, T. A., Miniati, F., Singh, M., & Raychaudhury, S. 2002, New Astronomy, 7, 249

Bagchi, J., Sirothia, S. K., Werner, N., et al. 2011, The Astrophysical Journal Letters, 736, 8

Barbosa, D., Bartlett, J. G., Blanchard, A., & Oukbir, J. 1996, Astronomy & Astrophysics, 314, 13

Bartelmann, M. & Schneider, P. 2001, Physics Reports, 340, 291

Basu, K. 2012, Monthly Notices of the Royal Astronomical Society, 421, 112

Bauer, F. E., Fabian, A. C., Sanders, J. S., Allen, S. W., & Johnstone, R. M. 2005, Monthly Notices of the Royal Astronomical Society, 359, 1481

Beck, R., Brandenburg, A., Moss, D., Shukurov, A., & Sokoloff, D. 1996, Annual Review of Astronomy and Astrophysics, 34, 155

Beck, R. & Krause, M. 2005, Astronomische Nachrichten, 326, 414

Bell, A. R. 1978, Monthly Notices of the Royal Astronomical Society, 182, 147

Benson, B. A., Church, S. E., Ade, P. A. R., et al. 2004, The Astrophysical Journal, 617, 829

Binney, J. & Tabor, G. 1995, Monthly Notices of the Royal Astronomical Society, 6, 663

Birkinshaw, M. 1999, Physics Reports, 310, 97

Bîrzan, L., Rafferty, D. A., McNamara, B. R., Wise, M. W., & Nulsen, P. E. J. 2004, The Astrophysical Journal, 607, 800

Blandford, R. & Eichler, D. 1987, Physics Reports, 154, 1

Blasi, P. & Colafrancesco, S. 1999, Astroparticle Physics, 12, 169

Böhringer, H., Pratt, G. W., Arnaud, M., et al. 2010, Astronomy & Astrophysics, 514, A32

Böhringer, H., Schuecker, P., Guzzo, L., et al. 2001, Astronomy & Astrophysics, 369, 826

Böhringer, H., Voges, W., Huchra, J. P., et al. 2000, The Astrophysical Journal Supplement Series, 129, 435

Bonafede, A., Brüggen, M., van Weeren, R., et al. 2012, Monthly Notices of the Royal Astronomical Society, 426, 40

Bonafede, A., Cassano, R., Brüggen, M., et al. 2017, Monthly Notices of the Royal Astronomical Society, 470, 3465

Bonafede, A., Feretti, L., Giovannini, G., et al. 2009a, Astronomy & Astrophysics, 503, 707

Bonafede, A., Feretti, L., Murgia, M., et al. 2010, Astronomy & Astrophysics, 513, A30

Bonafede, A., Giovannini, G., Feretti, L., Govoni, F., & Murgia, M. 2009b, Astronomy & Astrophysics, 494, 429

Bonafede, A., Intema, H. T., Brüggen, M., et al. 2014, The Astrophysical Journal, 785, 1

Bonamente, M., Joy, M., LaRoque, S. J., et al. 2008, The Astrophysical Journal, 675, 106

Botteon, A., Brunetti, G., Ryu, D., & Roh, S. 2020a, Astronomy & Astrophysics, 634, A64

Botteon, A., Cassano, R., van Weeren, R. J., et al. 2021, The Astrophysical Journal Letters, 914, L29

Botteon, A., Gastaldello, F., Brunetti, G., & Dallacasa, D. 2016a, Monthly Notices of the Royal Astronomical Society, 460, L84

Botteon, A., Gastaldello, F., Brunetti, G., & Kale, R. 2016b, Monthly Notices of the Royal Astronomical Society, 463, 1534

Botteon, A., Shimwell, T. W., Cassano, R., et al. 2022, Astronomy & Astrophysics, 660, A78

Botteon, A., van Weeren, R. J., Brunetti, G., et al. 2020b, Monthly Notices of the Royal Astronomical Society, 499, 11

Bourdin, H., Mazzotta, P., Markevitch, M., Giacintucci, S., & Brunetti, G. 2013, The Astrophysical Journal, 486, 347

Boxelaar, J. M., van Weeren, R. J., & Botteon, A. 2021, Astronomy and Computing, 35, 100464

Brentjens, M. A. & de Bruyn, A. G. 2005, Astronomy & Astrophysics, 441, 1217

Briggs, D. S. 1995, PhD thesis, The New Mexico Institue of Mining and Technology

Brown, S. & Rudnick, L. 2011, Monthly Notices of the Royal Astronomical Society, 412, 2

Brüggen, M. & Kaiser, C. R. 2002, Nature, 418, 301

Brüggen, M. & Vazza, F. 2020, Monthly Notices of the Royal Astronomical Society, 493, 2306

Brunetti, G., Cassano, R., Dolag, K., & Setti, G. 2009, Astronomy & Astrophysics, 507, 661

Brunetti, G., Giacintucci, S., Cassano, R., et al. 2008, Nature, 455, 944

Brunetti, G. & Jones, T. W. 2014, International Journal of Modern Physics D, 23, 1430007

Brunetti, G. & Lazarian, A. 2016, Monthly Notices of the Royal Astronomical Society, 458, 2584

Brunetti, G., Setti, G., & Comastri, A. 1997, Astronomy & Astrophysics, 325, 898

Brunetti, G., Setti, G., Feretti, L., & Giovannini, G. 2001, Monthly Notices of the Royal Astronomical Society, 320, 365

Brunetti, G., Venturi, T., Dallacasa, D., et al. 2007, The Astrophysical Journal, 670, L5

Bruno, L., Brunetti, G., Botteon, A., et al. 2023, Astronomy & Astrophysics, 672, A41

Buote, D. A. & Tsai, J. C. 1995, The Astrophysical Journal, 20

Burn, B. J. 1966, Monthly Notices of the Royal Astronomical Society, 133, 67

Carlstrom, J. E., Holder, G. P., & Reese, E. D. 2002, Annual Reviews of Astronomy and Astrophysics, 40, 643

Cassano, R. & Brunetti, G. 2005, Monthly Notices of the Royal Astronomical Society, 357, 1313

Cassano, R., Brunetti, G., Giocoli, C., & Ettori, S. 2016, Astronomy & Astrophysics, 593, A81

Cassano, R., Brunetti, G., Norris, R. P., et al. 2012, Astronomy & Astrophysics, 548, A100

Cassano, R., Brunetti, G., & Setti, G. 2006, Monthly Notices of the Royal Astronomical Society, 369, 1577

Cassano, R., Cuciti, V., Brunetti, G., et al. 2023, Astronomy & Astrophysics, 672, A43

Cassano, R., Ettori, S., Brunetti, G., et al. 2013, The Astrophysical Journal, 777, 141

Cassano, R., Ettori, S., Giacintucci, S., et al. 2010, The Astrophysical Journal Letters, 721, 82

Churazov, E., Brüggen, M., Kaiser, C. R., Böhringer, H., & Forman, W. 2001, The Astrophysical Journal, 554, 261

Clowe, D., Bradač, M., Gonzalez, A. H., et al. 2006, The Astrophysical Journal, 648, L109

Clowe, D., Gonzalez, A., & Markevitch, M. 2004, The Astrophysical Journal, 604, 596

Croston, J. H., Pratt, G. W., Böhringer, H., et al. 2008, Astronomy & Astrophysics, 487, 431

Cuciti, V., Cassano, R., Brunetti, G., et al. 2021, Astronomy & Astrophysics, 647, 51

Cuciti, V., Cassano, R., Brunetti, G., et al. 2015, Astronomy & Astrophysics, 580, A97

Cuciti, V., Cassano, R., Sereno, M., et al. 2023, arXiv e-prints

da Silva, A. C., Kay, S. T., Liddle, A. R., & Thomas, P. A. 2004, Monthly Notices of the Royal Astronomical Society, 348, 1401

de Gasperin, F., Brunetti, G., Brüggen, M., et al. 2020, Astronomy & Astrophysics, 642, A85

de Gasperin, F., Dijkema, T. J., Drabent, A., et al. 2019, Astronomy & Astrophysics, 622, A5

de Gasperin, F., Edler, H. W., Williams, W. L., et al. 2023, Astronomy & Astrophysics, 673, A165

de Gasperin, F., Intema, H. T., Shimwell, T. W., et al. 2017, Science Advances, 3, e1701634

de Gasperin, F., Intema, H. T., van Weeren, R. J., et al. 2015, Monthly Notices of the Royal Astronomical Society, 453, 3483

de Gasperin, F., Mevius, M., Rafferty, D. A., Intema, H. T., & Fallows, R. A. 2018, Astronomy & Astrophysics, 615, A179

de Gasperin, F., Rudnick, L., Finoguenov, A., et al. 2022, Astronomy & Astrophysics, 659, A146

de Gasperin, F., van Weeren, R. J., Brüggen, M., et al. 2014, Monthly Notices of the Royal Astronomical Society, 444, 3130

de Gasperin, F., Williams, W. L., Best, P., et al. 2021, Astronomy & Astrophysics, 648, A104

Di Gennaro, G., van Weeren, R. J., Hoeft, M., et al. 2018, The Astrophysical Journal, 865, 24

Di Gennaro, G., van Weeren, R. J., Rudnick, L., et al. 2021, The Astrophysical Journal, 911, 3

Domínguez-Fernández, P., Brüggen, M., Vazza, F., et al. 2021, Monthly Notices of the Royal Astronomical Society, 500, 795

Donnert, J., Dolag, K., Brunetti, G., & Cassano, R. 2013, Monthly Notices of the Royal Astronomical Society, 429, 3564

Donnert, J., Vazza, F., Brüggen, M., et al. 2018, Space Science Reviews, 214, 1

Dwarakanath, K. S., Parekh, V., Kale, R., & George, L. T. 2018, Monthly Notices of the Royal Astronomical Society, 477, 957

Eckert, D., Jauzac, M., Vazza, F., et al. 2016, Monthly Notices of the Royal Astronomical Society, 461, 1302

Enßlin, T. A., Biermann, P. L., Klein, U., & Kohle, S. 1998, Astronomy & Astrophysics, 332, 395

Fabian, A. C., Nulsen, P. E., & Canizares, C. R. 1984, Nature, 310, 733

Feretti, L., Giovannini, G., Govoni, F., & Murgia, M. 2012, Astronomy & Astrophysics Review, 20, 1

Fermi, E. 1949, Physical Review, 75, 1169

Finner, K., HyeongHan, K., Jee, M. J., et al. 2021, The Astrophysical Journal, 918, 72

Finner, K., Jee, M. J., Golovich, N., et al. 2017, The Astrophysical Journal, 851, 46

Finoguenov, A., Sarazin, C. L., Nakazawa, K., Wik, D. R., & Clarke, T. E. 2010, The Astrophysical Journal, 715, 1143

Fruscione, A., McDowell, J. C., Allen, G. E., et al. 2006, in Observatory Operations: Strategies, Processes, and Systems, Vol. 6270 (SPIE), 62701V

Fujita, Y., Akamatsu, H., & Kimura, S. S. 2016, Publications of the Astronomical Society of Japan, 68, 34

Fujita, Y., Takizawa, M., Yamazaki, R., Akamatsu, H., & Ohno, H. 2015, The Astrophysical Journal, 815, 116

George, L. T., Dwarakanath, K. S., Johnston-Hollitt, M., et al. 2015, Monthly Notices of the Royal Astronomical Society, 451, 4207

Ghirardini, V., Bahar, Y., Bulbul, E., et al. 2022, Astronomy & Astrophysics, 661, A12

Giacintucci, S., Venturi, T., Macario, G., et al. 2008, Astronomy & Astrophysics, 486, 347

Giovannini, G., Bonafede, A., Feretti, L., et al. 2009, Astronomy & Astrophysics, 507, 1257

Giovannini, G., Feretti, L., & Stanghellini, C. 1991, Astronomy & Astrophysics, 252, 528

Golovich, N., Dawson, W. A., Wittman, D. M., et al. 2019a, The Astrophysical Journal Supplement Series, 240, 39

Golovich, N., Dawson, W. A., Wittman, D. M., et al. 2019b, The Astrophysical Journal, 882, 69

Govoni, F. & Feretti, L. 2004, International Journal of Modern Physics D, 13, 1549

Govoni, F., Murgia, M., Xu, H., et al. 2013, Astronomy & Astrophysics, 554, 102

Ha, J.-H., Ryu, D., & Kang, H. 2018a, The Astrophysical Journal, 857, 26

Ha, J.-H., Ryu, D., Kang, H., & van Marle, A. J. 2018b, The Astrophysical Journal, 864, 105

Haardt, F. & Maraschi, L. 1991, The Astrophysical Journal, 380, L51

Hardcastle, M. J. & Croston, J. H. 2020, New Astronomy Reviews, 88, 101539

Harwood, J. J., Hardcastle, M. J., Croston, J. H., & Goodger, J. L. 2013, Monthly Notices of the Royal Astronomical Society, 435, 3353

Hattori, S., Ota, N., Zhang, Y. Y., Akamatsu, H., & Finoguenov, A. 2017, Publications of the Astronomical Society of Japan, 69, 39

Hoang, D. N., Brüggen, M., Botteon, A., et al. 2022, Astronomy & Astrophysics, 665, A60

Hoang, D. N., Shimwell, T. W., Stroe, A., et al. 2017, Monthly Notices of the Royal Astronomical Society, 471, 1107

Hoeft, M. & Brüggen, M. 2007, Monthly Notices of the Royal Astronomical Society, 375, 77

Hoeft, M., Nuza, S. E., Gottlöber, S., et al. 2011, Journal of Astrophysics and Astronomy, 32, 509

Intema, H. T., van der Tol, S., Cotton, W. D., et al. 2009, Astronomy & Astrophysics, 501, 1185

Jaffe, W. J. 1977, The Astrophysical Journal, 212, 1

Jee, M. J., Dawson, W. A., Stroe, A., et al. 2016, The Astrophysical Journal, 817, 179

Jones, A., de Gasperin, F., Cuciti, V., et al. 2023, arXiv e-prints

Jones, A., de Gasperin, F., Cuciti, V., et al. 2021, Monthly Notices of the Royal Astronomical Society, 505, 4762

Jones, C. & Forman, W. 1984, The Astrophysical Journal, 276, 38

Jones, C. & Forman, W. 1999, The Astrophysical Journal, 511, 65

Kale, R., Dwarakanath, K. S., Bagchi, J., & Paul, S. 2012, Monthly Notices of the Royal Astronomical Society, 426, 1204

Kale, R., Venturi, T., Giacintucci, S., et al. 2015, Astronomy & Astrophysics, 579, A92

Kale, R., Venturi, T., Giacintucci, S., et al. 2013, Astronomy & Astrophysics, 557, A99

Kang, H. 2015, Journal of the Korean Astronomical Society, 48, 9

Kang, H. 2016, Journal of the Korean Astronomical Society, 49, 145

Kang, H., Petrosian, V., Ryu, D., & Jones, T. W. 2014, The Astrophysical Journal, 788, 142

Kang, H. & Ryu, D. 2011, The Astrophysical Journal, 734, 18

Kang, H. & Ryu, D. 2016, The Astrophysical Journal, 823

Kang, H., Ryu, D., & Jones, T. W. 2012, The Astrophysical Journal, 756, 97

Kang, H., Ryu, D., & Jones, T. W. 2017, The Astrophysical Journal, 840, 42

Kardashev, N. S. 1962, Soviet Astronomy, 6, 317

Krivonos, R. A., Vikhlinin, A. A., Markevitch, M. L., & Pavlinsky, M. N. 2003, Astronomy Letters, 29, 425

Landau, L. D. & Lifshitz, E. M. 1959, Fluid mechanics (Pergamon Press)

Liang, H., Hunstead, R. W., Birkinshaw, M., & Andreani, P. 2000, The Astrophysical Journal, 544, 686

Locatelli, N. T., Rajpurohit, K., Vazza, F., et al. 2020, Monthly Notices of the Royal Astronomical Society: Letters, 496, L48

Loi, F., Murgia, M., Govoni, F., et al. 2017, Monthly Notices of the Royal Astronomical Society, 472, 3605

Longair, M. 2010, High Energy Astrophysics (Cambridge University Press)

Lovisari, L., Forman, W. R., Jones, C., et al. 2017, The Astrophysical Journal, 846, 51

Lovisari, L., Schellenberger, G., Sereno, M., et al. 2020, The Astrophysical Journal, 892, 102

Macario, G., Markevitch, M., Giacintucci, S., et al. 2011, The Astrophysical Journal, 728, 82

Mandal, S., Intema, H. T., van Weeren, R. J., et al. 2020, Astronomy & Astrophysics, 634, A4

Mangum, J. G. & Wallace, P. 2015, Publications of the Astronomical Society of the Pacific, 127, 74

Markevitch, M., Gonzalez, A. H., David, L., et al. 2002, The Astrophysical Journal, 567, 27

Markevitch, M., Govoni, F., Brunetti, G., & Jerius, D. 2005, The Astrophysical Journal, 627, 733

Markevitch, M., Ponman, T. J., Nulsen, P. E. J., et al. 2000, The Astrophysical Journal, 541, 542

Markevitch, M., Sarazin, C. L., & Vikhlinin1, A. 1999, The Astrophysical Journal, 521, 526

Markevitch, M. & Vikhlinin, A. 2007, Physics Reports, 443, 1

Marrone, D. P., Smith, G. P., Richard, J., et al. 2009, The Astrophysical Journal, 701, L114

McMullin, J. P., Waters, B., Schiebel, D., Young, W., & Golap, K. 2007, in Astronomical Data Analysis Software and Systems XVI, Vol. 376, 127

Mohan, N. & Rafferty, D. 2015, PyBDSF: Python Blob Detection and Source Finder

Mohr, J. J., Fabricant, D. G., & Geller, M. J. 1993, The Astrophysical Journal, 413, 492

Murgia, M., Govoni, F., Markevitch, M., et al. 2009, Astronomy & Astrophysics, 499, 679

Nurgaliev, D., McDonald, M., Benson, B. A., et al. 2013, The Astrophysical Journal, 779, 112

Nuza, S. E., Gelszinnis, J., Hoeft, M., & Yepes, G. 2017, Monthly Notices of the Royal Astronomical Society, 470, 240

Nuza, S. E., Hoeft, M., van Weeren, R. J., Gottlöber, S., & Yepes, G. 2012, Monthly Notices of the Royal Astronomical Society, 420, 2006

Offringa, A. R., McKinley, B., Hurley-Walker, N., et al. 2014, Monthly Notices of the Royal Astronomical Society, 444, 606

Offringa, A. R., Van De Gronde, J. J., & Roerdink, J. B. 2012, Astronomy & Astrophysics, 539, A95

Ogrean, G. A. & Brüggen, M. 2013, Monthly Notices of the Royal Astronomical Society, 433, 1701

Ogrean, G. A., Brüggen, M., Röttgering, H., et al. 2013, Monthly Notices of the Royal Astronomical Society, 429, 2617

Oppermann, N., Junklewitz, H., Greiner, M., et al. 2015, Astronomy & Astrophysics, 575, A118

Pacholczyk, A. G. 1970, Radio astrophysics. Nonthermal processes in galactic and extragalactic sources (W.H. Freeman, San Francisco)

Pearce, C. J. J., Van Weeren, R. J., Andrade-Santos, F., et al. 2017, The Astrophysical Journal, 845, 81

Perley, R. A. & Butler, B. J. 2017, The Astrophysical Journal Supplement Series, 230, 7

Petrosian, V. 2001, The Astrophysical Journal, 557, 560

Piffaretti, R., Arnaud, M., Pratt, G. W., Pointecouteau, E., & Melin, J.-B. 2011, Astronomy & Astrophysics, 534, A109

Pinkney, J., Roettiger, K., Burns, J. O., & Bird, C. M. 1996, The Astrophysical Journal Supplement Series, 19, 1

Pinzke, A., Oh, S. P., & Pfrommer, C. 2013, Monthly Notices of the Royal Astronomical Society, 435, 1061

Planck Collaboration, Ade, P. A., Aghanim, N., et al. 2014, Astronomy & Astrophysics, 571, A29

Planck Collaboration, Ade, P. A., Aghanim, N., et al. 2011, Astronomy & Astrophysics, 536, A8

Planck Collaboration, Ade, P. A., Aghanim, N., et al. 2016, Astronomy & Astrophysics, 594, A27

Poole, G. B., Fardal, M. A., Babul, A., et al. 2006, Monthly Notices of the Royal Astronomical Society, 373, 881

Pratt, G. W., Croston, J. H., Arnaud, M., & Böhringer, H. 2009, Astronomy & Astrophysics, 498, 361

Press, W. H. & Schechter, P. 1974, The Astrophysical Journal, 187, 425

Rajpurohit, K., Hoeft, M., van Weeren, R. J., et al. 2018, The Astrophysical Journal, 852, 65

Rajpurohit, K., van Weeren, R. J., Hoeft, M., et al. 2022, The Astrophysical Journal, 927, 80

Rajpurohit, K., Vazza, F., Hoeft, M., et al. 2020, Astronomy & Astrophysics, 642, L13

Rasia, E., Meneghetti, M., & Ettori, S. 2013, Astronomical Review, 8, 40

Reiprich, T. H. & Böhringer, H. 2002, The Astrophysical Journal, 567, 716

Rice, S. O. 1945, Bell System Technical Journal, 23, 282

Roettiger, K., Burns, J. O., & Stone, J. M. 1999, The Astrophysical Journal, 518, 603

Santos, J. S., Rosati, P., Tozzi, P., et al. 2008, Astronomy & Astrophysics, 483, 35

Sarazin, C. L. 1999, The Astrophysical Journal, 520, 529

Scaife, A. M. & Heald, G. H. 2012, Monthly Notices of the Royal Astronomical Society: Letters, 423, L30

Shimwell, T. W., Brown, S., Feain, I. J., et al. 2014, Monthly Notices of the Royal Astronomical Society, 440, 2901

Shimwell, T. W., Hardcastle, M. J., Tasse, C., et al. 2022, Astronomy & Astrophysics, 659, A1

Shimwell, T. W., Luckin, J., Brüggen, M., et al. 2016, Monthly Notices of the Royal Astronomical Society, 459, 277

Shimwell, T. W., Markevitch, M., Brown, S., et al. 2015, Monthly Notices of the Royal Astronomical Society, 449, 1486

Shimwell, T. W., Röttgering, H. J., Best, P. N., et al. 2017, Astronomy & Astrophysics, 598, A104

Shimwell, T. W., Tasse, C., Hardcastle, M. J., et al. 2019, Astronomy & Astrophysics, 622, A1

Simmons, J. & Stewart, B. 1985, Astronomy & Astrophysics, 142, 100

Skillman, S. W., Hallman, E. J., O'Shea, B. W., et al. 2011, The Astrophysical Journal, 735, 96

Skillman, S. W., Xu, H., Hallman, E. J., et al. 2013, The Astrophysical Journal, 765, 21

Stokes, G. G. 1851, Transactions of the Cambridge Philosophical Society, 9, 8

Stuardi, C., Bonafede, A., Wittor, D., et al. 2019, Monthly Notices of the Royal Astronomical Society, 489, 3905

Sunyaev, R. A. & Zel'dovich, Y. B. 1970, Astrophysics and Space Science, 7, 3

Sunyaev, R. A. & Zel'dovich, Y. B. 1972, Comments on Astrophysics and Space Physics, 4, 173

Sunyaev, R. A. & Zel'dovich, Y. B. 1980, Annual Review of Astronomy and Astrophysics, 18, 537

Tasse, C., Shimwell, T., Hardcastle, M. J., et al. 2021, Astronomy & Astrophysics, 648, A1

Thierbach, M., Klein, U., & Wielebinski, R. 2002, Astronomy & Astrophysics, 397, 53

Thompson, A. R., Moran, J. M., & Swenson, G. W. 2017, Interferometry and Synthesis in Radio Astronomy, Astronomy and Astrophysics Library (Springer International Publishing)

Thompson, R. & Nagamine, K. 2012, Monthly Notices of the Royal Astronomical Society, 419, 3560

Umetsu, K. 2020, The Astronomy and Astrophysics Review, 28, 1

Urdampilleta, I., Akamatsu, H., Mernier, F., et al. 2018, Astronomy & Astrophysics, 618, A74

van Haarlem, M. P., Wise, M. W., Gunst, A. W., et al. 2013, Astronomy & Astrophysics, 556, A2

van Weeren, R. J., Andrade-Santos, F., Dawson, W. A., et al. 2017, Nature Astronomy, 1, 0005

van Weeren, R. J., Brüggen, M., Röttgering, H. J., & Hoeft, M. 2011, Monthly Notices of the Royal Astronomical Society, 418, 230

van Weeren, R. J., Brunetti, G., Brüggen, M., et al. 2016a, The Astrophysical Journal, 818, 204

van Weeren, R. J., de Gasperin, F., Akamatsu, H., et al. 2019, Space Science Reviews, 215, 16

van Weeren, R. J., Röttgering, H. J., Brüggen, M., & Hoeft, M. 2010, Science, 330, 347

van Weeren, R. J., Röttgering, H. J. A., Brüggen, M., & Cohen, A. 2009, Astronomy & Astrophysics, 508, 75

van Weeren, R. J., Shimwell, T. W., Botteon, A., et al. 2021, Astronomy & Astrophysics, 651, A115

van Weeren, R. J., Williams, W. L., Hardcastle, M. J., et al. 2016b, The Astrophysical Journal Supplement Series, 223, 2

Vazza, F. & Brüggen, M. 2014, Monthly Notices of the Royal Astronomical Society, 437, 2291

Vazza, F., Brüggen, M., van Weeren, R., et al. 2012, Monthly Notices of the Royal Astronomical Society, 421, 1868

Vazza, F., Jones, T. W., Brüggen, M., et al. 2017, Monthly Notices of the Royal Astronomical Society, 464, 210

Venturi, T., Giacintucci, S., Brunetti, G., et al. 2007, Astronomy & Astrophysics, 463, 937

Venturi, T., Giacintucci, S., Dallacasa, D., et al. 2008, Astronomy & Astrophysics, 484, 327

Vikhlinin, A., Markevitch, M., & Murray, S. S. 2001, The Astrophysical Journal, 551, 160

von der Linden, A., Mantz, A., Allen, S. W., et al. 2014, Monthly Notices of the Royal Astronomical Society, 443, 1973

Wardle, J. F. C. & Kronberg, P. P. 1974, The Astrophysical Journal, 194, 249

Wittor, D., Ettori, S., Vazza, F., et al. 2021, Monthly Notices of the Royal Astronomical Society, 506, 396

Wittor, D., Hoeft, M., Vazza, F., Brüggen, M., & Domínguez-Fernández, P. 2019, Monthly Notices of the Royal Astronomical Society, 490, 3987

Wittor, D., Vazza, F., & Brüggen, M. 2017, Monthly Notices of the Royal Astronomical Society, 464, 4448

Wright, C. O. & Brainerd, T. G. 2000, The Astrophysical Journal, 534, 34

Zhang, C., Churazov, E., Forman, W. R., & Lyskova, N. 2019, Monthly Notices of the Royal Astronomical Society, 488, 5259

Zhang, X., Simionescu, A., Gastaldello, F., et al. 2023, Astronomy & Astrophysics, 672, A42

Zimbardo, G. & Perri, S. 2018, Monthly Notices of the Royal Astronomical Society, 478, 4922

ZuHone, J. & Su, Y. 2022, Handbook of X-ray and Gamma-ray Astrophysics, 1

ZuHone, J. A., Markevitch, M., Weinberger, R., Nulsen, P., & Ehlert, K. 2021, The Astrophysical Journal, 914, 73

Zwicky, F., Herzog, E., Wild, P., Karpowicz, M., & Kowal, C. T. 1961, Catalogue of galaxies and of clusters of galaxies, Vol. I (Caltech, Pasadena, CA)